University of Copenhagen

Master Thesis

DARK
Niels Bohr Institute

Origin of Gas Metallicity Gradients in Observed and Simulated Galaxies

Author:
Emma Louise Bødker Espersen

Supervisors:
Michaela M. Hirschmann
Maritza A. Lara-Lopez
Steen H. Hansen

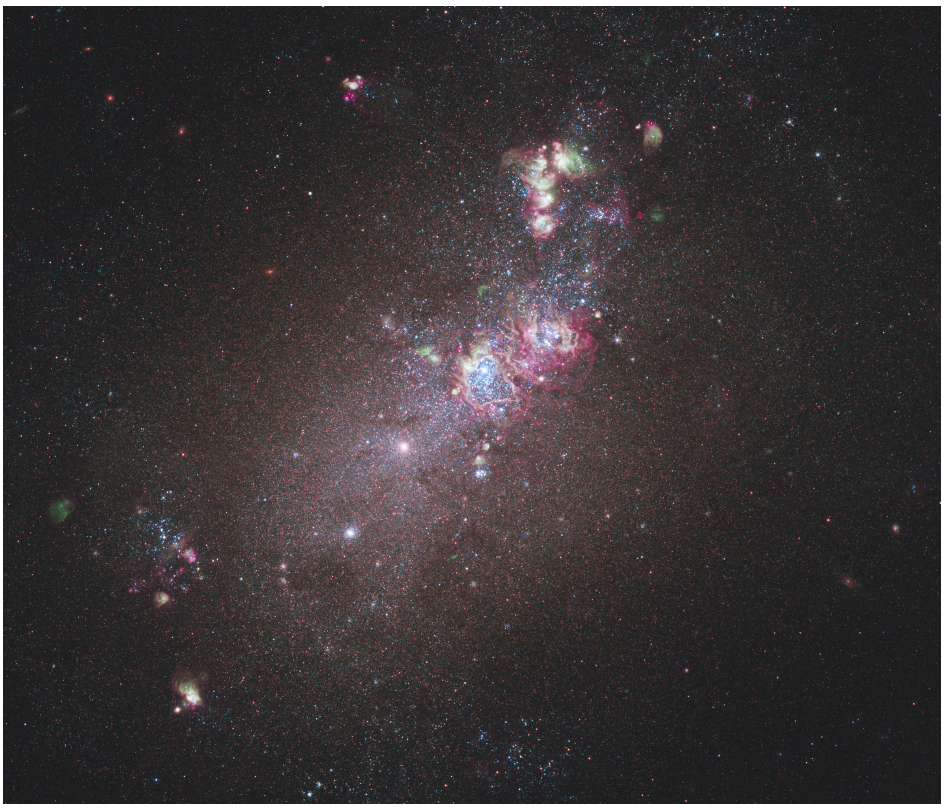

Composite image of NGC 4214 from separate exposures acquired by the Wide Field Camera 3 instrument on the Hubble Space Telescope in December 2009.

September 10th, 2021

Declaration of Authorship

I, Emma Louise Bødker Espersen, declare that this thesis titled "Origin of Gas Metallicity Gradients in Observed and Simulated Galaxies" and the work presented in it are my own. I confirm that:

- This work was done wholly while in candidature for a master degree at this University.
- Where I have consulted the published work of others, this is always clearly attributed.
- Where I have quoted from the work of others, the source is always given. With the exception of such quotations, this thesis is entirely my own work.
- I have acknowledged all main sources of help.
- Where the thesis is based on work done by myself jointly with others, I have made clear exactly what was done by others and what I have contributed myself.

Total page count (incl. bibliography and appendices): 117

Page count (excl. bibliography and appendices): 89

Appendix page count: 21

Signature: 

Date: Friday, September 10th, 2021

UNIVERSITY OF COPENHAGEN

Abstract

DARK
Niels Bohr Institute

Master of Astrophysics

Origin of Gas Metallicity Gradients in Observed and Simulated Galaxies

by Emma Louise Bødker Espersen

Spatially resolved observations have repeatedly revealed negative gas metallicity gradients in nearby galaxies, which contain important information on various physical processes affecting the evolution of galaxies. Cosmological hydrodynamic simulations can, in principle, predict such negative gas metallicity gradients for present-day galaxies due to inside-out growth, shaped by various internal and external processes (e.g. feedback versus merger history). A fully accurate comparison, however, has been impeded so far, as observed gas metallicities are derived from nebular emission lines in galaxy spectra, making several simplifying assumptions, whereas modern cosmological simulations intrinsically predict this quantity, but cannot self-consistently produce nebular emission lines. In this master thesis, we will use a novel methodology (Hirschmann et al., 2017; Hirschmann et al., 2019) to generate, for the first time, synthetic spatially resolved emission line maps for simulated galaxies (e.g., IllustrisTNG), which will allow us to derive gas metallicities for simulated galaxies in the same way as for observed ones. Such a uniquely accurate confrontation to observations (Lara-López et al., 2021) enable us to robustly assess, which are the main physical mechanisms shaping the gas metallicity gradients of local galaxies.

Contents

List of Abbreviations

AGB	**A**symptotic **G**iant **B**ranch
AGN	**A**ctive **G**alactic **N**uclei
AMD	**A**ge-**M**etallicity **D**egeneracy
BH	**B**lack **H**ole
BPT (diagram)	**B**aldwin, **P**hillips & **T**erlevich (diagram)
FMR	**F**undamental **M**etallicity **R**elation
IFS	**I**ntegral **F**ield **S**pectrograph
IFU	**I**ntegral **F**ield **U**nit
LINER	**L**ow **I**onization **N**arrow **E**mission line **R**egions
MMR	**M**ass **M**etallicity **R**elation
SF	**S**tar **F**orming
SMBH	**S**uper **M**assive **B**lack **H**ole
PAGB (star)	**P**ost-**A**symptotic **G**iant **B**ranch (star)
SN(e)	**S**uper**N**ova(e)
(s)SFR	(**s**pecific) **S**tar **F**ormation **R**ate
SSP	**S**imple **S**tellar **P**opulation
THINGS	**T**he **HI** **N**earby **G**alaxy **S**urvey
(Illustris) **TNG**	(Illustris) **T**he **N**ew **G**eneration

Chapter 1

Framework

1.1 Introduction

Studying the chemical history of galaxies is a fundamental part of understanding galaxy evolution. In astronomy, all elements heavier than He are referred to as metals, and are produced in various states of stellar evolution. Metals account for only $\sim 1\%$ of the mass in galaxies, but are the dominant factor when it comes to chemistry, ionization, heating- and cooling processes which are important to star formation.
Elements from carbon to iron are produced through nucleosynthesis in stellar interiors. In particular, the production of carbon is of great importance, as it facilitates the alpha process. Here, consecutive capture of alpha particles $^4_2$He by heavier nuclei produce the alpha elements (O, Ne, Mg, Si, S, Ar, Ca and Ti, amongst others), with the main production sites being red giants and SNe II (Narlikar, 1995). Fe-peak elements (Ti, V, Cr, Mn, Fe, Co, Ni and Zn) are, like alpha elements, produced in massive stars and SNe II. Yet, the majority are synthesized in SNe Ia, as the thermonuclear explosions allow silicon burning (Peters and Hirschi, 2013). Neutron capture elements (e.g. Y and Ba) are produced mainly in AGB stars, neutron star mergers, and, to a lesser extent, SNe II (Christensen-Dalsgaard, 2008; Peters and Hirschi, 2013). Proton capture elements include Na and Al, requiring extremely high temperatures, and can therefore be produced in SNe II and fast rotating massive stars (Christensen-Dalsgaard, 2008; Peters and Hirschi, 2013).

Massive stars are crucial in the nucleosynthesis of elements beyond oxygen, and thus galactic chemical evolution. They furthermore impact the surrounding interstellar medium (hereafter ISM) through strong stellar winds, shocks and ionizing UV emission (leading to H II regions). They are also the progenitors of SNe Ib, -Ic and -II, neutron stars and black holes. Smaller amounts of the metals produced in stellar nucleosynthesis are expelled into the ISM through stellar winds at the earlier evolutionary stages. The vast majority of metals are however incorporated into the ISM at later stages of the stellar evolution when expelled by strong stellar winds from AGB stars, mechanical winds from fast rotating massive stars or SNe explosions. Studying the chemical enrichment of the ISM through observations and simulations thereby enables a deeper and more comprehensive understanding of galactic evolution.

The gas-phase metallicity of a galaxy, denoted Z, is defined as the mass fraction of elements heavier than helium (here, in Solar units)

$$Z = \log\left(\frac{M_Z/M_{\text{gas}}}{Z_\odot}\right) \tag{1.1}$$

where M_Z is the mass of all elements heavier than He, M_{gas} is the total gas mass and $Z_\odot = 0.0127$ is the Solar metallicity.
To obtain the total abundance of a given element, in theory one must measure the flux from all transitions of that element. This is often not possible in practice through observations, due to both technical limitations and variation in line strengths. Astronomers have therefore

developed both theoretical and empirical methods (and hybrids thereof) to estimate the gas metallicities. Specifically, nebular spectroscopy of H II regions is widely used in astronomy to study planetary nebulae, late phase supernovae and in particular star-forming regions. H II regions are nebulae primarily composed of hydrogen, of which most is ionized (hence "H II") by UV radiation emitted from central sources. H II regions have large variations in both size and density, and the ionizing sources of these regions include young, massive stars, hot white dwarfs, shocks and stars in planetary nebulae.
A few examples of predicted temperature $T_\star$, number emitted of hydrogen ionizing photons per second within the radius of the Strömgren sphere R_S (that is, the point where the total rates of ionization and recombination are equal) for a few O-B stars can be seen in table 1.1. All values are adopted from table 2.3 of Osterbrock and Ferland (2006).

Spectral Type	$T_\star$ [K]	$\log(Q_\mathrm{ion}\ [\mathrm{s}^{-1}])$	R_S [pc]
O3 Ia	50,700	50.1	147
O5 V	46,100	49.53	94
B0 V	33,300	48.16	33
B0.5 III	30,200	48.27	36

Table 1.1: Predicted surface temperatures $T_\star$, number emitted of hydrogen ionizing photons per second $\log(Q_\mathrm{ion})$, and radius of Strömgren sphere R_S in parsecs for various stellar spectral types. All values are adopted from table 2.3 of Osterbrock and Ferland (2006).

Emission from atomic transitions in the spectra of H II regions can trace both temperatures and densities, chemical abundances, velocity structures, and ionization mechanisms. As atom-ion and atom-atom collisions are rare in H II regions, collisions with free electrons are dominant. Despite the low abundance of metals, forbidden transitions make a significant contribution because of their low excitation potentials ($\sim$ few eV). Because the photon emitted in the forbidden line transition has only a very low probability of being absorbed, the emitted photon easily escapes from the nebula gas and can thus be observed here from Earth (e.g. Spitzer, 1998; Osterbrock and Ferland, 2006; Léna et al., 2012).
The gas-phase metallicity of a H II region can thus be estimated using (strong) emission from forbidden transitions, in combination with recombination lines like Hα and Hβ, calibrated in terms of the metallicity (e.g. Skillman et al., 1989; Kewley and Dopita, 2002; Kobulnicky and Kewley, 2004; Pilyugin and Thuan, 2005; Moustakas, 2006; Pilyugin and Grebel, 2016). Some of the more abundant metallicity-sensitive lines found in the optical of H II regions are [O II] $\lambda\lambda\lambda\, 3727, 7318, 7324$, [O III] $\lambda\lambda\, 4959, 5007$, [N II] $\lambda\lambda\, 6548, 84$ and [S II] $\lambda\lambda\, 6717, 31$.
Wide availability of spectrophotometry of H II regions, combined with the apparent abundance and strength of emission lines makes oxygen a good tool for estimating the metallicity, which is then denoted $12 + \log(\mathrm{O/H})$. In the analysis presented here, [O III] $\lambda\, 5007$, [N II] $\lambda\, 6584$ and [S II] $\lambda\lambda\, 6717, 31$ are used to estimate the gas-phase metallicity, as described in further detail in Chapter 2.

1.2 The Mass-Metallicity Relation

The correlation between the stellar mass and gas-phase metallicity of galaxies is well-established, and formally known as the mass-metallicity relation (also denoted MZR or MMR). The first demonstration of this relation was in a study of irregular and blue compact galaxies by Lequeux et al. (1979). This correlation has later been firmly confirmed by Tremonti et al. (2004) using data for $\sim$ 53,000 galaxies from the Sloan Digital Sky Survey (SDSS); they found $\mathrm{O/H} \propto M_\star^{1/3}$

at $10^{8.5} M_\odot \leqslant M_\star \leqslant 10^{10.5} M_\odot$, with a flattening at $M_\star \gtrsim 10^{10.5} M_\odot$. The flattening, or 'turnover', in the MMR is illustrated in figure 1.1, which shows the mass-metallicity relation for 92,033 SDSS galaxies.

Using observations of local dwarf irregular galaxies, Lee et al. (2006) further extended the MMR to ~ 2.5 dex lower in stellar mass, but their metallicities were $0.2 - 0.3$ dex lower than that of Tremonti et al. (2004), which may be explained from the different methods used in the metallicity estimation. The MMR has primarily been explained by galactic outflows of metal-rich gas being more effective in low-mass galaxies, whereas galaxies with larger potential wells are able to retain most ejecta inside the halo, which can later be recycled (e.g. Tremonti et al., 2004; Ma et al., 2015). Additionally, galaxies with higher stellar mass have experienced more cycles of star-formation than galaxies of lower stellar mass, and have thus had more time to release metals into the ISM. Possible explanations under current debate also include downsizing (that is, the star formation efficiency is higher in more massive galaxies, and hence evolve faster than less massive ones, see e.g. Maiolino et al., 2008; Calura et al., 2009) and variation in the IMF (through a change in stellar yields, see e.g. Lian et al., 2018; Curti et al., 2019).

More recent work (Ellison et al., 2007) has shown that galaxies with high SFR systematically exhibit lower metallicities; in particular, at fixed stellar mass $\leqslant 10^{11} M_\odot$, higher SFR imply lower metallicity. This offset can be reduced by accounting for the SFR as shown by Mannucci et al. (2010) and Lara-López et al. (2010). The relationship between stellar mass, metallicity and SFR is known as the fundamental metallicity relation (FZR or FMR). This has lead to the understanding that the MMR is in fact a projection in the 3-dimensional space formed by the interplay between SFR, stellar mass and gas-phase metallicity.

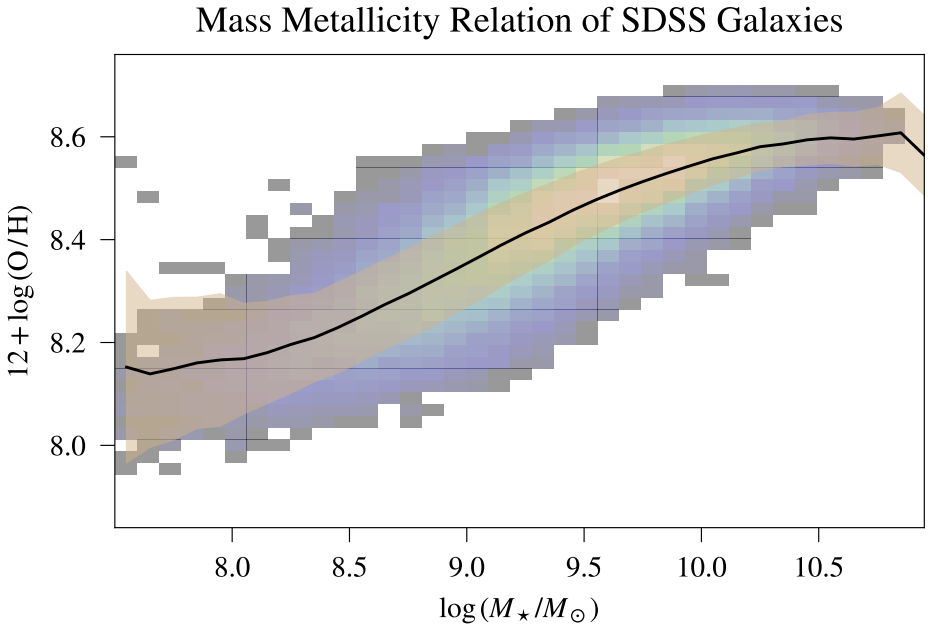

Figure 1.1: Mass metallicity relation of 92,033 SDSS galaxies at $z \sim 0$. The 2D histogram shows the whole sample, and the solid black line and shaded area indicate mean and standard deviations of 0.1 dex bins in $\log(M_\star/M_\odot)$, respectively.

1.3 The Radial Gas-Phase Metallicity Profile

The metal content and -distribution of galaxies is governed by an interplay of a number of galactic properties and -processes, such as (e.g. Mo et al., 2010)

- Gas infall, which dilute the metal content of the ISM, but may also trigger star formation
- Feedback driven by active galactic nuclei (AGN), star-formation and stellar evolution processes, which induce outflows that may dispel or redistribute enriched gas on galactic scales
- Injection of metals into the ISM by stellar evolution processes
- Turbulent processes, leading to metal-mixing
- Galaxy-galaxy interactions and mergers, which can trigger nuclear starbursts or AGN, and cause tidal perturbations in the disc

The picture is further complicated by the fact that many of these parameters, either directly or indirectly, influence each other.
Negative gas-phase metallicity gradients in disc galaxies have been known for decades (Searle, 1971; Peimbert, 1979; Shaver et al., 1983; Vila-Costas and Edmunds, 1992), and they have been examined in several observational studies (e.g. Afflerbach et al., 1997; Deharveng et al., 2000; Bresolin et al., 2005; Bresolin et al., 2009a; Bresolin et al., 2009b). The large amounts of high quality data from integral field spectroscopy now available (e.g. CALIFA and MaNGA) has enabled the exploration of the dependencies of the metallicity gradient (hereafter $\nabla_{\mathrm{O/H}}$) on a variety of galactic properties (e.g. Sánchez et al., 2014a; Sánchez-Menguiano et al., 2016; Pérez-Montero et al., 2016).
Observations of nearby galaxies allow astronomers to probe the ISM, and by comparing such observations with predictions from both theoretical models and simulations, it is possible to infer constraints on uncertain models adopted in galaxy evolution simulations. For example, observations of strong negative metallicity gradients in spiral galaxies indicate that the central regions are populated by more evolved, and thus more metal-rich, stellar populations, while metal-poor and less-evolved stars are located in the exterior of spirals (e.g. Zaritsky et al., 1994). This is consistent with the inside-out formation scenario of spirals, where spiral discs form from gas accretion, as seen in infall models of galaxy formation (e.g. Matteucci and François, 1989; Boissier and Prantzos, 1999).
Another example is galaxies experiencing mergers or interactions with other galaxies. These interactions disturb the gas in galaxies, and can create turbulent motions that energize the gas, causing it to lose angular momentum and flow radially inwards. Simulations of gas-rich mergers of disc galaxies of comparable mass have shown that these events are able to induce high levels of nuclear star-formation, and possibly the creation of AGN (Mo et al., 2010). Interacting or merging starburst- and active galaxies have likewise been observed to be associated with high central gas densities (e.g. Larson and Tinsley, 1978).
While the galaxy-galaxy interaction/merger may initially flatten the metallicity gradient, as metal-poor gas in the outer region is mixed with enriched gas from the companion galaxy, the induced central star-formation can re-establish a negative gradient, as metals are injected into the ISM by supernovae and stellar winds. However, subsequent outflows of enriched gas driven by feedback from AGN, star-formation and stellar evolution can flatten the metallicity gradient or truncate it at the outer regions. A flattened metallicity gradient, or truncation in the outer parts, have in addition to these galaxy-galaxy interactions been linked to the presence of bars (e.g. Bresolin et al., 2009a; Sánchez et al., 2010; Marino et al., 2012; Rosales-Ortega et al., 2011). For galaxies which are not part of interacting or merging systems, a flattening of the

metallicity gradient have been proposed to arise from metal-mixing caused by radial gas flows (Lacey and Fall, 1985; Goetz and Koeppen, 1992; Portinari and Chiosi, 2000; Ferguson and Clarke, 2001; Schönrich and Binney, 2009; Bilitewski and Schönrich, 2012; Spitoni et al., 2013, among others).

In the remainder of chapter 1, I will as an introduction to this thesis summarise some main results from literature on simulations of the gas-phase metallicity profile.

1.4 Observations of the Radial Gas-Phase Metallicity Profile

This following section will summarize some of the main observational results found in literature on how $\nabla_{\mathrm{O/H}}$ relates to characteristics of galaxies. While ellipticals also have been shown to exhibit negative gas-phase metallicity gradients, the lower amount of gas in these galaxies makes it hard to observationally measure reliable gradients. Additionally, we here study gas rich galaxies, why this section and the following will have late-type galaxies as the primary focus.

1.4.1 Stellar Mass and Morphology

There has been several studies investigating how the stellar mass is linked to the shape of the metallicity gradient. Massive galaxies form earlier and in denser regions than less massive ones. Moreover, less gas is accreted in massive galaxies at later times, and different types of physical processes occur in galaxies of different masses. For example, it is well known from observations that most massive galaxies have a massive black hole in the center. Some of these accrete gas from the surrounding ISM (i.e. AGN), and high mass galaxies are thus affected to a higher degree by AGN feedback, which can blow out metal-rich gas from the center and into the halo. Thus studying the effect of stellar mass on $\nabla_{\mathrm{O/H}}$ is not trivial, and it is in fact the underlying physical processes and structures that arise from the stellar mass, rather than the mass itself, that affects $\nabla_{\mathrm{O/H}}$.

A trend of $\nabla_{\mathrm{O/H}}$ with stellar mass, with shallow gradients for the more massive systems ($M_\star \gtrsim 10^{10.25-10.5} M_\odot$), has been reported by several observational studies (e.g. Belfiore et al., 2017; Poetrodjojo et al., 2018; Mingozzi et al., 2020). From a study of 550 nearby galaxies from SDSS IV MaNGA survey in the mass range $9.0 \leqslant \log(M_\star/M_\odot) \leqslant 11.5$, Belfiore et al. (2017) found, when normalizing to the disc size, roughly flat gradients for galaxies with $\log(M_\star/M_\odot) = 9$, while galaxies with $\log(M_\star/M_\odot) = 10.5$ exhibited slopes as steep as $-0.14\, R_e^{-1}$, where even more massive systems exhibited slightly flattened gradients. They also detected a flattening in the central regions $R < 1\, R_e$ (see also Sánchez-Menguiano et al., 2018), as well as a mild flattening in the outer region $R > 2\, R_e$. Similar results are found in Mingozzi et al. (2020) for 1795 local galaxies with $\log(M_\star/M_\odot) > 9$, with a flattening in the central regions ($R < 0.5\, R_e$) for galaxies with $\log(M_\star/M_\odot) > 10.25$, as well as a mild flattening of $\nabla_{\mathrm{O/H}}$ in the outer regions ($R > 1.5\, R_e$) for galaxies with $\log(M_\star/M_\odot) < 10$.

Sánchez-Menguiano et al. (2016) measured gas abundance profiles in 122 face-on spiral galaxies observed by the CALIFA survey. Contradictory to the aforementioned studies (Belfiore et al., 2017; Poetrodjojo et al., 2018; Mingozzi et al., 2020), Sánchez-Menguiano et al. (2016) found no trend of $\nabla_{\mathrm{O/H}}$ with stellar mass when normalizing to the physical scale of the disc. They furthermore emphasize the importance of defining the gradient normalised to the disc effective radius. The disc effective radius presents a clear correlation galactic properties such as the absolute magnitude, mass, or morphological type, hence why a normalization is important. In addition, they suggest that the observed flattening in the outer parts of the galaxies is a universal property of spiral galaxies, as they found no significant differences for sub samples based on the morphological type, presence or absence of bars and luminosity. However, this

discrepancy may arise from statitsics, as both MaNGA and SAMI have much larger samples than what was examined by Sánchez-Menguiano et al. (2016).

The morphology of galaxies and the shape of the radial metallicity profile may be related by certain processes that affect both, as different physical processes which can alter the gradients take place in spirals and ellipticals. In the case of spirals, three main aspects can be considered; how tightly wound the arms are (early/late type spiral), the presence/absence of a bar or bulge, along with the relative size of these (bulge-to-total, bar-to-total), and the relative size of the disc (disc-to-total).
Sánchez-Menguiano et al. (2016) examined relations between the slope distribution and morphological type. They found that in general, the earlier spirals (Sa) present flatter gradients than the later type ones (Sd), though these results are not deemed statistically significant. They furthermore found essentially no correlation of $\nabla_{O/H}$ with the presence of a bar, but speculates that the bulge-to-total may play an important role in the derived gradients. A chemical evolution model by Cavichia et al. (2013) found that the aforementioned flattening of $\nabla_{O/H}$ in the inner region may be caused by the presence of a bar, creating radial gas flows in the disc, which increases the SFR at the corotation radius and enriches the surrounding medium. This flattening has not only been observed in nebular emission, but also in stellar populations throughout the Galaxy (Hayden et al., 2014).

1.4.2 Feedback

AGN- and stellar driven feedback create gaseous outflows of metal-rich gas, which is then redistributed at larger radii. This has been observed to be true at high redshift, especially in conjunction with high mass and star formation surface density (Newman et al., 2012; Genzel et al., 2014; Wuyts et al., 2016). Some of the enriched gas that has been blown out into the halo will escape, but a fraction is recycled and mixed with incoming low-metallicity gas from the surrounding intergalactic medium, producing a flattening in the outer regions (Sánchez-Menguiano et al., 2016). Results from Stott et al. (2014) indicated a trend between metallicity gradient and specific star formation rate (sSFR) for star-forming galaxies at $z \sim 1$, with high sSFR being associated with metal-poor gas in the central region. They note that this relation may be due to radial inflows of unenriched gas, driven either by mergers or accretion.

1.4.3 Mergers

Through observations of morphologically disturbed galaxies, merger galaxies and close neighbours, previous works have found that these objects exhibit flatter metallicity gradients. Mergers induce inflow of metal-poor gas in the central regions and cause mixing of low- and high-metallicity gas, flattening the slope of the gradient. Additionally, the disc may be destroyed and bursts of star formation can occur, evening out the gas metallicity (Wuyts et al., 2016; Sánchez-Menguiano et al., 2016). In the case of minor mergers or encounters/perturbations caused by orbiting satellite galaxies, Sánchez-Menguiano et al. (2016) notes that the external regions may experience an increase in the metal content, again flattening the outer metallicity profile.

The main take away from the observations described above may be summarised as:

- *Inside-out galaxy formation* The negative metallicity gradients observed in disc galaxies are believed to be associated with the inside-out galaxy formation scenario, where discs form from gas accretion. Here, central regions are populated by more evolved, metal-rich stellar populations. On the other hand, the exterior regions need longer time to build up higher metallicities due to the radial dependance on gas infall timescales (and thereby SFR).

- *Central star-formation and gas inflow* Central star-formation can create negative gradients as metals are injected into the ISM by supernovae and stellar winds. Shallow gradients or a truncation at low radii have however also been associated with high sSFR, as the radial inflows of pristine gas feeding the star formation dilute the central ISM.
- *AGN- and stellar feedback* Outflows of enriched gas driven by feedback from AGN, central star-formation and supernovae can flatten the metallicity gradient or truncate it at the outer regions.
- *Galaxy interactions and mergers* At early stages, the interaction/merger-induced turbulent motions may initially flatten $\nabla_{\mathrm{O/H}}$ due to both mixing in the exterior and radial inflows of metal-poor gas. At later stages, a negative gradient may be re-established from induced nuclear starbursts.

The following section will describe the current state of simulations in this context.

1.5 Radial Gas-Phase Metallicity Profiles in Simulations

Galactic chemical evolution models has for years been used to try to understand the physical processes governing the shape of the metallicity gradient. Among others, topics such as infall of metal-rich gas (Tosi, 1988), star formation processes (Portinari and Chiosi, 1999), relations with luminosity (Prantzos and Boissier, 2000), and the formation scenarios of galactic components (Hou et al., 2000; Portinari and Chiosi, 2000; Chiappini et al., 2001; Fu et al., 2009) have all been investigated in the past. In recent years however, hydrodynamical simulations which follow the chemical enrichment of the ISM have become of greater importance in this area (e.g. Kobayashi, 2004; Rupke et al., 2010b; Teklu et al., 2015; Tissera et al., 2015; Sillero et al., 2017; Taylor and Kobayashi, 2017). This section lists some of the theoretical findings and predictions of metallicity gradients, and their relation to some of the galactic properties and physical processes taking place.

1.5.1 Stellar Mass and Morphology

While low mass galaxies tend to have flatter gradients due to more efficient outflows, both Tissera et al. (2015) and Ma et al. (2017) found no clear correlations between stellar mass and the slope of the metallicity gradient. Sánchez et al. (2012) additionally reported a characteristic slope for 38 face-on spiral galaxies when normalizing to the disc size, with no correlations with morphological characteristics. This has been suggested to indicate a correlation with mass growth of disc galaxies (Sánchez-Menguiano et al., 2016).

The negative metallicity gradients observed in disc galaxies are believed to be associated with the inside-out galaxy formation scenario, as described earlier. Several observational studies have provided evidence to support this theory, both through the study of radial stellar age gradients (Delgado et al., 2014; Delgado et al., 2015; Ruiz-Lara et al., 2015) and star-formation histories (Pérez et al., 2013). In this scenario, gas infall timescales have a radial dependance, such that they increase with increasing galactocentric distance (Sánchez-Menguiano et al., 2016), which in turn yield a radial dependence of the SFR. The negative $\nabla_{\mathrm{O/H}}$ have likewise been found to be a consequence of the global inside-out disc assembly in simulations (e.g. Tissera et al., 2015). Gas metallicity gradients have additionally been shown to flatten over time, as the outer parts of galaxies need more time to build up higher abundances (e.g. Belfiore et al., 2016).

Galactic bars can induce gas flows from an angular momentum exchange with the disc (Athanassoula, 1992; Friedli, 1998). This may cause radial redistribution of enriched gas, yielding lower central metallicities (Dutil and Roy, 1999). Another effect from bars earlier

reported are shallower gradients compared to unbarred spiral galaxies (Vila-Costas and Edmunds, 1992; Zaritsky et al., 1994; Friedli et al., 1994; Friedli and Benz, 1995; Martin and Roy, 1995; Dutil and Roy, 1999; Portinari and Chiosi, 2000; Cavichia et al., 2013) or even positive gradients (e.g. Tissera et al., 2015). While more recent studies have found no correlations between the presence of bars and $\nabla_{O/H}$ (Sánchez et al., 2012; Sánchez et al., 2014a; Sánchez-Blázquez et al., 2014; Cheung et al., 2015; Sánchez-Menguiano et al., 2016), there is evidence in both observations (Sánchez-Menguiano et al., 2016) and simulations (Fu et al., 2013) that the gas-phase metallicity gradients correlate with the relative size of bars or bulges.

A physical explanation comes from the bulge formation process; when a bulge is formed through mergers, it sets the strength of $\nabla_{O/H}$ as most of the gas in the merger galaxies is consumed during an induced starburst. Once the new merger galaxy is able to accrete, $\nabla_{O/H}$ is re-established, but with signs of a negative gradient. The disc component also relates to the radial metallicity gradient, where shallower slopes are found with increasing disc sizes (Tissera et al., 2018) and very negative slopes are mainly present in rotationally supported galaxies (Ma et al., 2017).

1.5.2 Feedback

Variations in $\nabla_{O/H}$ on $\lesssim$ Gyr time scales have previously been associated with starburst episodes (Ma et al., 2017). Feedback from these violent events can drive strong outflows that flatten metallicity gradients by redistribution of metals on galactic scales. As suggested by Ma et al. (2017), the feedback processes may be more efficient in low-mass galaxies and galaxies with high sSFR, which tend to exhibit flat gradients. The metals ejected from a galaxy earlier may be re-accreted at later times, which leads to a flatter present-day $\nabla_{O/H}$ (Fu et al., 2013). AGN driven feedback has been shown to be associated with flattened metallicity gradients, both due to quenching of star formation (Taylor and Kobayashi, 2017) and removal of metal-rich gas (Tissera et al., 2015). Collacchioni et al. (2020) has shown that the slope of the radial metallicity profile depends more strongly on gas accretion rate than on stellar mass, SFR or gas fraction, and associate steeper (negative) slopes with low-metallicity gas accretion. The dependency may arise due to feedback from high levels of star formation triggered by significant gas accretion onto the central regions, or likewise increased feedback from AGN. Tissera et al. (2015) confirmed observational results by Stott et al. (2014), who found a possible correlation between $\nabla_{O/H}$ and sSFR, where high sSFR is associated with central metal-poor gas, primarily funnelled by merger-driven gaseous inflows. Indeed, Tissera et al. (2015) report that positive abundance gradients are found in galaxies with morphological perturbations, such as a very close companion, the presence of central bars, or clear ring structures in the discs.

1.5.3 Mergers

Tissera et al. (2018) found a positive correlation between $\nabla_{O/H}$ and stellar mass for galaxies with quiet merger histories, while only a weak relation was present for galaxies that had experienced mergers. Several studies (Kobayashi, 2004; Wuyts et al., 2016; Sánchez-Menguiano et al., 2016; Ma et al., 2017; Taylor and Kobayashi, 2017) associate flattened metallicity gradients with galaxies exhibiting strongly disturbed morphologies and/or have experienced mergers. Specifically, Kobayashi (2004) find that shallow gradients are a result of major mergers due to strong induced star formation.

Another effect found by both Tissera et al. (2015) and Sillero et al. (2017) is, that galaxies showing positive or very negative gradients are all associated with galaxy-galaxy interactions or highly disturbed morphologies - however, not *all* galaxies subject to perturbations have positive/very negative gradients. A possible explanation for the former is given in Sillero

et al. (2017); the galaxy-galaxy interactions produce strong gaseous inflows, which dilute the gas-phase metallicity in the central regions and increase the sSFR.

The main take away from the simulations described above may be summarised as:

- *Inside-out galaxy formation and morphology* Simulations support the inside-out formation scenario as indicated by observations. While no clear dependencies on morphology are found, the size of a bulge or bar relative to the disc seem to correlate with the gradient. This effect is seen in the sense that shallower gradients are found with increasing relative sizes bars, likely due to metal redistribution caused by radial gas flows. If a bulge is formed through a merger, a negative metallicity gradient can be produced as gas in the inner regions is consumed by an induced starburst.

- *Central star-formation and gas inflow* Negative metallicity gradients have been associated with low-metallicity gas accretion, which may arise from high levels of central star formation. The slope of $\nabla_{\mathrm{O/H}}$ have been found to correlate with sSFR, such that an increase in sSFR initially cause a flattening, while a (negative) steepening is found as stars inject metals into the central ISM.

- *AGN- and stellar feedback* Feedback from starburst episodes can drive strong outflows that flatten metallicity gradients by redistribution of metals on galactic scales. This process may be more efficient in low-mass galaxies and galaxies with high sSFR, which tend to exhibit flat gradients. AGN driven feedback has been shown to be associated with flattened metallicity gradients, both due to quenching of star formation and removal of metal-rich gas.

- *Galaxy interactions and mergers* Interactions and early stages of mergers have been shown to flatten the gas-phase metallicity gradient as low-metallicity gas is driven inwards. Flattened metallicity gradients are however generally associated with galaxies exhibiting strongly disturbed morphologies and/or have experienced mergers. At later stages, the increase in gas density allow high central star formation, resulting in negative $\nabla_{\mathrm{O/H}}$.

1.6 Motivation and Problem Statement

At the moment, the comparison between simulations and observations can only be approximate, since metallicities are a direct output in simulations, but are derived from emission lines in observations, making a number of assumptions. Specifically, large variations in the total metallicities and metallicity gradients derived in observations are found when using different calibrations.
Thus, in this thesis, we want to achieve a new level of accuracy when comparing simulated and observed galaxy metallicities, by modelling emission lines of simulated galaxies such that gas-phase metallicities can be derived in the same way as in observations. Using a novel methodology (Hirschmann et al., 2017) to generate synthetic spatially resolved emission line maps for simulated galaxies from the cosmological hydrodynamic simulations IllustrisTNG, we will in this thesis derive gas-phase metallicity gradients for simulated galaxies in the same way as for observed ones. The simulated gradients will be compared to six nearby, spatially resolved galaxies observed with integral field spectroscopy (Lara-López et al., 2021); that is, four spiral galaxies (NGC 925, NGC 5194, NGC 6946 and NGC 7331) and two dwarf irregular galaxies (NGC 1569 and NGC 4214). This uniquely accurate confrontation enables the assessment of the main physical mechanisms shaping the gas metallicity gradients of local galaxies. The main characteristics of the observed galaxies are given in table 1.2.

Galaxy	NGC 925	NGC 1569	NGC 4214	NGC 5194	NGC 6946	NGC 7331
Distance [Mpc]	9.2	2	2.9	8.0	5.9	14.7
SFR [$M_\odot$/yr]	0.561	0.06	0.107	3.125	3.239	2.987
$\log(M_\star/M_\odot)$	9.9	8.4	8.8	10.6	10.5	10.1
$\log(M_{\mathrm{H\,I}}/M_\odot)$	9.8	7.9	8.7	9.5	9.8	10.1
Morphology	Barred Spiral	Dwarf Irregular	Barred Dwarf Irregular	Spiral	Spiral	Unbarred Spiral

Table 1.2: Basic information on the observed galaxies.

The structure of the thesis is as follows: Chapter 2 is divided into two parts. The first part, section 2.1, includes first a description of the observations (sections 2.1.1 - 2.1.2), data reduction (section 2.1.3), emission line diagnostics (section 2.1.4), and the approach used for the estimation of metallicity and ionization parameters, including the used calibrations (section 2.1.5). Secondly, the method used in the derivation of the gradients are described in section 2.1.6. The observational results are additionally presented and discussed here. The second part, section 2.2, gives first an overview of the IllustrisTNG simulations, galaxy sample selection (section 2.2.1), and the derivation of parameters (sections 2.2.2 - 2.2.3). This is followed by a description of how the synthetic emission lines are generated, coupled to the simulations and converted into mock observations (section 2.2.4). Section 2.2.5 contains first a description of the derivation of the simulated gradients (section 2.2.5), followed by a presentation, comparison and discussion of the results obtained from emission line models and intrinsic simulation abundances (section 2.2.5). Possible dependencies of the metallicity gradient on galaxy properties is investigated using results from emission line models at redshift $z = 0$ in section 2.2.5. Lastly, the cosmic evolution of the metallicity gradient (from $z = 2$) is examined through case studies in section 2.2.5.
Chapter 3 is the main discussion, and the results from observations and simulations are compared and discussed in section 3.1. Caveats of the approaches and methodology used in this work are additionally discussed in sections 3.2 through 3.4, and the results are compared to litterature in section 3.5. Chapter 4 contains a summary and conclusion.

Chapter 2

Methodology and Results

The observational part of this master thesis is based on the Metal-THINGS survey (Lara-López et al., 2021), and the methodology, along with the adopted metallicity- and ionization calibrations, is described in section 2.1 below. The part dealing with the simulated galaxies from IllustrisTNG is based on synthetic optical nebular emission lines generated following Hirschmann et al. (2017) and Hirschmann et al. (2019), and is described later in section 2.2.

2.1 Integral Field Spectroscopy of Nearby Galaxies

2.1.1 Integral Field Spectroscopy

Integral field spectroscopy (IFS) is often used in astronomy to study objects that are extended on the sky (e.g. nebulae, galaxies, star clusters). Integral field units (IFU) come in three main types; a micro-lens array, a fibre bundle, optionally combined with a micro-lens array, and an image slicer. In IFS, the signal measured in each pixel is fed to a spectrograph. Each individual pixel hence yields a spectrum at a different position; that is, the flux is given as a function of position and wavelength. The IFS data is thus a cube consisting of contiguous spectral pixels (spaxels), and a schematic diagram of the IFS data cube structure is illustrated in figure 2.1. IFS enable observers to view the target both at a single wavelength "slice", as indicated in figure 2.1, or collapsed over several wavelength "slices". As each spaxel yield a spectrum at each wavelength slice, it is possible to examine the target in detail.

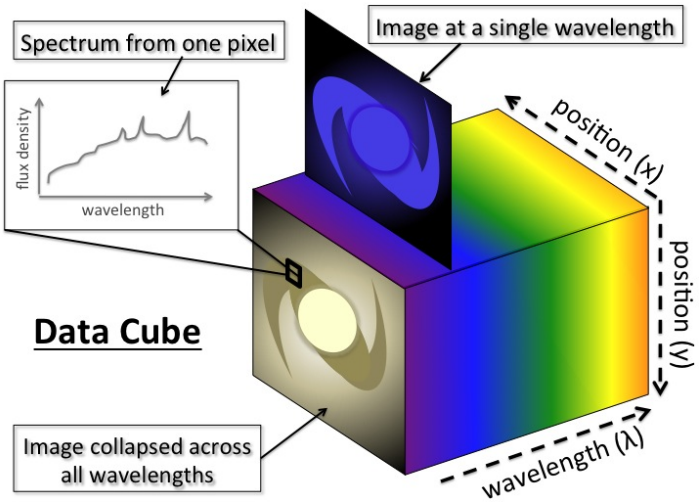

Figure 2.1: Schematic diagram of the IFS data cube structure (image credit: Harrison, 2014).

2.1.2 Observations

The selection of galaxies in the Metal-THINGS survey (Lara-López et al., 2021) is based on the THINGS survey (Walter et al., 2008), who observed 34 nearby galaxies of large angular sizes in radio using the Very Large Array (VLA). The Metal-THINGS survey (Lara-López et al., 2021) is obtaining complementary IFU spectroscopy. The IFU data is collected using the 2.7 m telescope at McDonald Observatory (*Harlan J. Smith Telescope* 2020), with the George Mitchel spectrograph (GMS, formerly known as VIRUS-P, Hill et al., 2008; *Mitchell Spectrograph* 2020). Additionally, observations with MUSE-Very Large Telescope (VLT) are performed for three galaxies located in the southern hemisphere. GMS has a field of view of $100'' \times 102''$, with a spatial sampling of $4.2''$, and a 1/3 filling factor. The IFU consists of 246 fibers arranged in a fixed pattern.

This thesis will be covering a total of six galaxies, namely NGC 925, NGC 1569, NGC 4214, NGC 5194, NGC 6946 and NGC 7331. All galaxies were observed through a red setup, as part of the Metal-THINGS survey (Lara-López et al., 2021), covering the wavelength range 3400 Å to 6800 Å. In this range, multiple strong emission lines are available, including Hα, Hβ, [O I] λ6300, [O III] $\lambda\lambda$4959, 5007, [N II] λ6584 and [S II] $\lambda\lambda$6717, 31.
The GMS field of view is arranged with 246 optical fibers with a 1/3 filling factor, meaning that there are gaps between each of the fibres, where no light is collected. This missing light is collected by **dithering**, which is the method of slightly changing the position of the fibres and taking multiple exposures. All observed galaxies are very extended on the sky as they are nearby, and to ensure a 90% surface coverage, every pointing is observed with three dither positions. The observing procedure consists of taking 900 s exposure per dither, followed by a sky exposure, and repetition of the process until 45 minutes in total is reached per dither, per pointing. The sky exposure is taken off source, allowing for sky subtraction in the reduction process.
Furthermore, a calibration/guide star was observed every night using six dither positions with 120 s exposures, in order to ensure a 99% flux coverage. Calibration lamps (here Neon and Argon for the red setup) were observed both at the beginning as well as the end of every night. This is used for wavelength calibration of the spectra. Table 2.1 lists the number of pointings, average seeing and observing period for the observed galaxies.

Galaxy	NGC 925	NGC 1569	NGC 4214	NGC 5194	NGC 6946	NGC 7331
Pointings	13	1	4	9	10	6
Projected size	174.7 pc	41.6 pc	62.4 pc	162.2 pc	120.6 pc	259.9 pc
Average seeing	$1.5''$	$1.9''$	$2.1''$	$1.8'' - 2.0''$	$1.8'' - 2.0''$	$2.0''$
Observations [MM/YY]	12/17, 1/18, 1/19	1/18	5/19, 12/19, 1/20	5/16, 6/18, 5/19, 6/21	8/16, 9/17, 6/18, 10/18, 11/19, 12/19, 10/20, 6/21	12/16, 9/17, 12/17, 1/18, 10/18

Table 2.1: Specifications of the observations. Each fiber is $4.2''$ in diameter, and the third row denote the corresponding projected physical size of each fiber.

2.1.3 Data Reduction

The basic reduction of the IFS data cubes consists of bias subtraction, flat frame correction and wavelength calibration. This was performed using P3D, which is a general data-reduction tool intended to be used with data of fiber-fed IFSs (*P3D* 2020). The tasks in P3D convert the raw data from CCD detectors into extracted spectra as indicated.

Bias Subtraction

CCDs and CMOS detectors has an inherent level of readout noise associated with them, which creates a noise pattern on the images. A **bias** frame is a 'zero-length' exposure with the shutter closed that captures this noise pattern, so that it can later be removed. This (fixed) noise pattern in not necessarily uniform, and so if the bias is not subtracted from the data, the flat frame correction may not work as intended. The reason for the zero-length exposure is to limit the noise pattern to only being that of the electronics. In practice, several (~ 10) zero-length exposures in a dark room are taken and the images are then stacked, where after the noise can be subtracted from the data frames spaxel by spaxel.

Flat Field Correction

Not all spaxels in a detector will detect the same amount of light when exposed to a uniform light source. Dust settling on the detector, lens vignetting et cetera will reduce the amount of light that reach the spaxels affected by this. In practice, this means that the detected images may contain 'dark spots' (from dust) or a vignette (from the lens). In order to correct for this, **flat frames** are taken. In astronomy, flat frames are taken by pointing the telescope to zenith at dusk when the sky (at zenith) - to a good approximation - is uniform. One then calibrates the spaxels based on the flat frames, essentially smoothing out the image.

Wavelength Calibration

When collecting data with an IFS, data cubes are obtained. The spectra in each spaxel are not given in units of wavelength though, but rather in a *relative* energy scale. This is when **wavelength calibration** comes in to play. As aforementioned, calibration lamps (Ne and Ar) were observed both at the beginning and the end of every night. The Ne and Ar emission lines have well-defined energies, which is then used for wavelength calibrating the spectral data.

Sky Subtraction and Dither Combination

As only the light from the respective galaxies are of interest, **sky subtraction** was performed. This is done by taking short (300 s) exposures of the sky off source, before and after each galaxy exposure. This allows for a 'pure' sky spectra, that can then be subtracted from the actual data, leaving a 'clean' galaxy image behind. Both the sky subtraction and the combination of dithers was performed using Python (*Python Software Foundation, Version 2.7* 2020).

Flux Calibration

Flux calibration was then performed on the calibrations stars, following the methods of Cairós et al. (2012) using six dither position as mentioned earlier. This ensures a 97% coverage. Based on this, a calibration function was then created using the packages `standard` and `sensfunc` in IRAF (Tody, 1986). The stellar continuum of all flux calibrated spectra was fitted using Starlight (Fernandes et al., 2005; Mateus et al., 2006; Asari et al., 2007).
The calibration stars are used for **flux calibration**, which is used for creating the sensitivity function. A simple relation between the observed continuum flux, F^0_λ, the measured continuum counts, I^c_λ, and the sensitivity function, S_λ, is (Churchill, 2010):

$$I^c_\lambda = S_\lambda \, F^0_\lambda \tag{2.1}$$

where the sensitivity function depends on multiple factors, such as; the location of the observatory; the telescope throughput; the collecting area of the telescope; atmospheric attenuation (dependant on airmass); the spectrograph design (Churchill, 2010). The sensitivity

function, derived for the calibration star using `standard` and `sensfunc` in IRAF, is then used to create a **sensitivity curve**. I refer to *IRAF: standard* (2000) and *IRAF: sensfunc* (1993) for a more detailed description of these tasks. The IRAF task `calibrate` calibrates the input spectra to a flux scale using the sensitivity curve. I again refer to *IRAF: calibrate* (1993) for a more detailed description of this task.

Starlight

The stellar continuum of the flux calibrated spectra was fitted using STARLIGHT (Fernandes et al., 2005; Mateus et al., 2006; Asari et al., 2007). Subsequently, 45 synthetic simple stellar populations (SSPs) from the evolutionary synthesis models of Bruzual and Charlot (2003) with ages from 1 Myr up to 13 Gyr and metallicities $Z = 0.005$, 0.02 and 0.05 were used to create a synthetic stellar continuum.
A **SSP** is a collection of stars with the same age and initial chemical composition but different masses. If a SSP is plotted in a Hertzsprung-Russel (H-R) diagram, the SSP will follow an isochrone, and one will see different evolutionary tracks traced out by stars of different masses. In practice, an example of a SSP could be a globular cluster, where hundreds of thousands of stars were formed around the same time of the same molecular cloud, such that the stars have very similar initial compositions.
Following this, the stellar continuum was subtracted from the spectra, and then the nebular emission lines were measured by fitting Gaussian line-profiles. The stellar continuum fitting and subtraction thereof was performed by collaborators of the Metal-THINGS survey, and I refer to Zinchenko et al. (2016) and Zinchenko et al. (2018) for a more detailed description.

Extinction Correction

Extinction is the combination of scattering and absorption of light by dust and gas. Shorter wavelengths are comparable to the sizes of dust grains, and are thus more affected by this than light emitted at longer wavelengths. Extinction thereby dims emitting sources, which need to be accounted for. The extinction correction, as described in the following, is carried out following Appendix A of López-Sánchez (2006). To correct for dust extinction, we model the intensity of the received light, $I(\lambda)$, as being the intensity of the light emitted from a source, $I_0(\lambda)$, obscured by dust with an optical depth τ_λ along the line of sight (between the observer and the source):

$$I(\lambda) = I_0(\lambda)\, \mathrm{e}^{-\tau_\lambda} \tag{2.2}$$

such that the optical depth τ_λ is defined as the natural logarithm of the ratio of incident to transmitted intensity through a material. Due to the size of the dust grains, the amount of scattering and absorption by dust is greater at shorter wavelengths (hence the term "reddening", see figure A.1 in López-Sánchez (2006)), and in general the opacity, which measure the ability of photons to pass through a material, $\kappa_\lambda \to 0$ as $\lambda \to \infty$.
Equation (2.2) may be expressed in terms of the extinction A_λ, using $\mathrm{e}^x = 10^{x\ \log(e)}$ and the opacity κ_λ:

$$\tau_\lambda = \int \kappa_\lambda \, \mathrm{d}s = \frac{0.4}{\log(\mathrm{e})} A_\lambda \tag{2.3}$$

By measuring the brightness of two stars of the same spectral type, one reddened (denoted 1) and one not reddened (or to a very low degree, denoted 2), the optical depth $\tau_\lambda(1)$ along the

line of sight to the reddened star can be estimated in the distances D_1 and D_2 are known:

$$\frac{\mathcal{F}_\lambda(1)}{\mathcal{F}_\lambda(2)} = \frac{\mathcal{F}_{0,\lambda}(1)\,\mathrm{e}^{-\tau_\lambda(1)}}{\mathcal{F}_{0,\lambda}(2)\,\mathrm{e}^{-\tau_\lambda(2)}} = \frac{D_1^2}{D_2^2}\,\mathrm{e}^{-(\tau_\lambda(1)-\tau_\lambda(2))} \tag{2.4}$$

$$\Longrightarrow \quad \tau_\lambda(1) - \tau_\lambda(2) \approx \tau_\lambda(1) \tag{2.5}$$

where the brightness $\mathcal{F}_\lambda = \pi\, F_\lambda$ is substituted for the intensity $I(\lambda)$ in equation (2.2). Note that all but the distances cancel out in the flux ratio $\mathcal{F}_{0,\lambda}(1)/\mathcal{F}_{0,\lambda}(2)$, as the stars are assumed to be of the same spectral type.

Observations of stars have resulted in empirical evidence that extinction of stellar light from different spectral types all follow (to a high degree) the same trend in regards of the wavelength dependency (Osterbrock and Ferland, 2006), that is to say the extinction follows a reddening law $A_\lambda = c' f'(\lambda)$, and a similar trend can be expressed for the (diffuse) interstellar medium. This thesis considers optical spectroscopy of nebular emission (3400 Å - 6800 Å), and in this regime, normalization by Hβ is convenient. Hence, by normalizing equation (2.4) by Hβ and applying (2.3), a new expression for $I(\lambda)$ (equation 2.2) can be found:

$$\frac{I(\lambda)}{I(\mathrm{H}\beta)} = \frac{I_0(\lambda)}{I_0(\mathrm{H}\beta)} \times 10^{-\log(\mathrm{e})\,(\tau_\lambda - \tau_{\mathrm{H}\beta})} \tag{2.6}$$

$$= \frac{I_0(\lambda)}{I_0(\mathrm{H}\beta)} \times 10^{-0.4\,(A_\lambda - A_{\mathrm{H}\beta})} \tag{2.7}$$

and as $A_\lambda = c'\, f'(\lambda)$, we can define a reddening coefficient which is constant with respect to Hβ extinction, namely $C(\mathrm{H}\beta)$, using the Balmer decrements

$$C(\mathrm{H}\beta) = \frac{1}{f(\lambda)} \log\left(\frac{I_0(\mathrm{H}\alpha)}{I_0(\mathrm{H}\beta)} \Big/ \frac{I(\mathrm{H}\alpha)}{I(\mathrm{H}\beta)}\right) \tag{2.8}$$

$$= \frac{1}{f(\lambda)} \log\left(2.878\,\frac{I(\mathrm{H}\beta)}{I(\mathrm{H}\alpha)}\right) \tag{2.9}$$

where $I(\mathrm{H}*)$ denotes the received light and $I_0(\mathrm{H}*)$ the light emitted from the source. Using a series of normalizations, we obtain a relation between $f(\lambda)$ and A_λ

$$f(\lambda) = \frac{A_\lambda}{A_{\mathrm{H}\beta}} - 1 = \frac{A_\lambda}{2.5\,C(\mathrm{H}\beta)} - 1 \tag{2.10}$$

Using reddening law of Cardelli et al. (1989) with $R_V = 3.1$ (the value in the diffuse interstellar medium)

$$\frac{A_\lambda}{A_V} = a(x) + \frac{b(x)}{R_V} \tag{2.11}$$

gives $f(\lambda) = -0.297$ in equation (2.9) (value adopted from table A.2 in López-Sánchez, 2006), and assuming $A_\lambda/A_V = 0.47$ (Lee et al., 2005). As to suit the observational regime, the optical/NIR ($1.1\,\mu\mathrm{m}^{-1} \leqslant x \leqslant 3.3\,\mu\mathrm{m}^{-1}$) parametrization of the Cardelli et al. (1989) reddening law is used. In this regime, $a(x)$ and $b(x)$ are defined as

$$\begin{aligned} a(x) = {} & 1 + 0.17699y - 0.50447y^2 - 0.02427y^3 + 0.72085y^4 + 0.01979y^5 \\ & - 0.77530y^6 + 0.32999y^7 \end{aligned} \tag{2.12}$$

$$\begin{aligned} b(x) = {} & 1.41338y + 2.28305y^2 + 1.07233y^3 - 5.38434y^4 - 0.62251y^5 \\ & + 5.30260y^6 - 2.09002y^7 \end{aligned} \tag{2.13}$$

where $y = x - 1.82$ and $x = 1/\lambda$ with λ in units of μm. The extinction corrected flux $\mathcal{F}_C(\lambda)$ for any line with wavelength λ is found spaxel-by-spaxel from the received flux $\mathcal{F}(\lambda)$ as:

$$\mathcal{F}_C(\lambda) = \mathcal{F}(\lambda) \times 10^{0.4\,A_\lambda} \tag{2.14}$$

with

$$\begin{aligned} A_\lambda &= 2.5\,[f(\lambda) + 1]\,C(\mathrm{H}\beta) \\ f(\lambda) &= \frac{a(x_\lambda) + b(x_\lambda)/R_V}{a(x_{\mathrm{H}\beta}) + b(x_{\mathrm{H}})/R_V} - 1 \\ C(\mathrm{H}\beta) &= -\frac{1}{0.297}\,\log\left(2.878\,\frac{\mathcal{F}(\mathrm{H}\beta)}{\mathcal{F}(\mathrm{H}\alpha)}\right) \end{aligned}$$

where $\mathcal{F}(\mathrm{H}\alpha)$ and $\mathcal{F}(\mathrm{H}\beta)$ are the (received) fluxes from Hα and Hβ in any spaxel, $x_\lambda = 1/\lambda$ and $x_{\mathrm{H}\beta} = 1/\lambda_{\mathrm{H}\beta}$.

Metal-THINGS Maps

Extinction corrected Hα and Hβ maps of the observed galaxies are shown in figures 2.2 and B.1, respectively. Only spaxels with a SNR > 3 for Hα and Hβ lines are shown. Strong emission from recombination lines like Hα and Hβ trace star formation, as these lines indicate photoionization powered by UV radiation from young, massive stars. The Hα maps of NGC 925, NGC 5194 and NGC 6946 present strong emission in the central region and spiral arms, while for NGC 7331, Hα emission is the strongest in the spiral structures. For the irregular dwarf galaxies, NGC 1569 and NGC 4214, the irregular shape is illustrated in the Hα maps, as no clear structures are present. Both galaxies are starbursts, and NGC 1569 exhibit strong Hα emission throughout the entire galaxy, clearly illustrating this. Two oval ring-like patterns of glowing ionized gas are visible in both the Hα- and Hβ map (figures B.1 and 2.2), with the upper ring roughly (499.2 pc $\times$ 249.6 pc) in size, and the lower ring roughly (187.2 pc $\times$ 312 pc) in size.

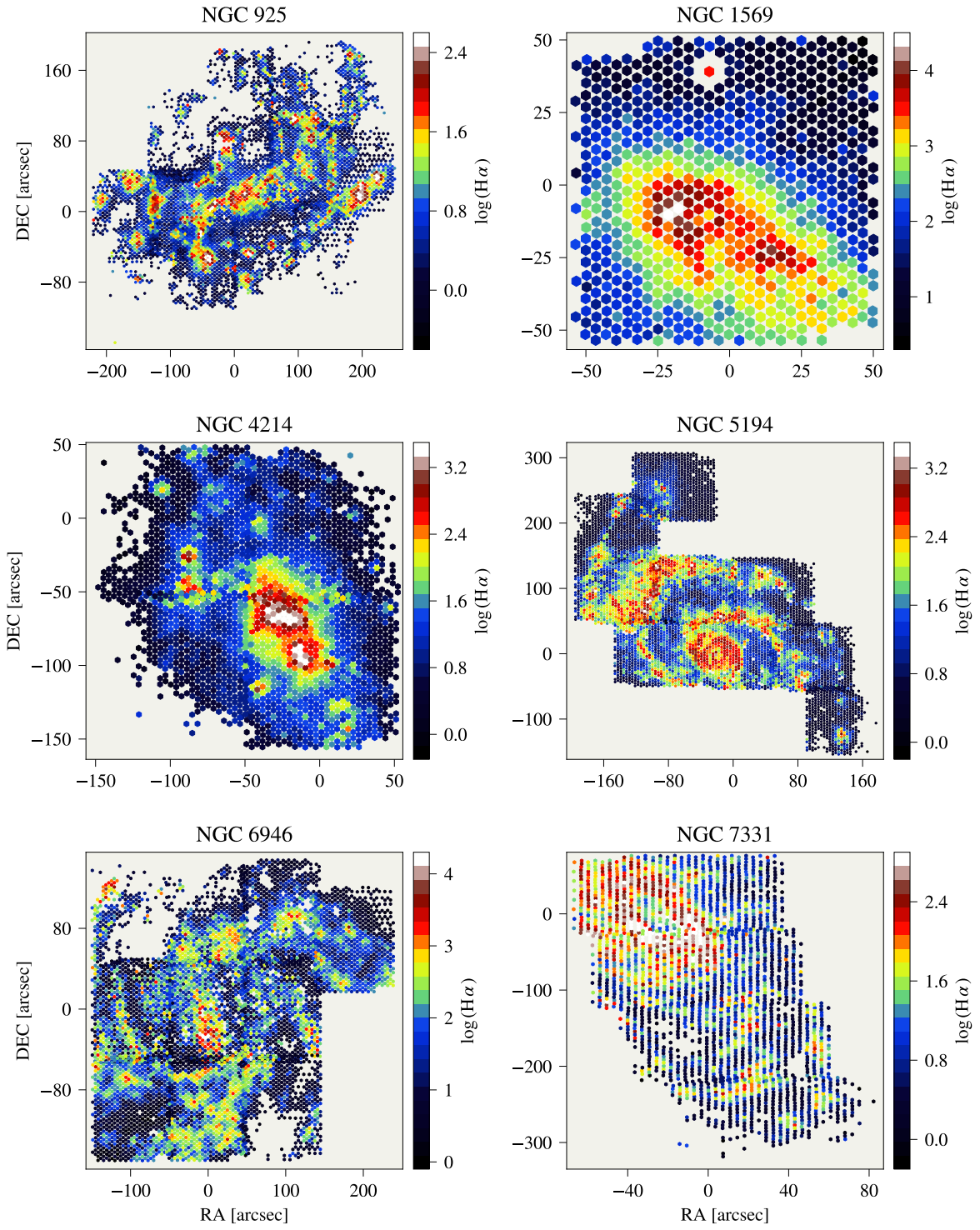

Figure 2.2: Extinction corrected Hα maps for the observed galaxies. Only spaxels with a SNR > 3 for Hα and Hβ lines are shown.

2.1.4 Diagnostic Diagrams

Optical emission trace emission from warm, ionized gas in the interstellar medium. By studying nebular optical spectra, it is thus possible to probe the underlying physical mechanisms that drive the gas ionization. It is empirically established that in extragalactic objects, the most prevalent excitation mechanisms include 1) photoionization by O and B stars, 2) photoionization by a power-law continuum source, or 3) shock wave heating. Additionally, planetary nebulae photoionized by very hot stars ($T > 50{,}000$ K) constitute another class (Baldwin et al., 1981).

Star-forming (hereafter SF) galaxies show lines emitted by H II regions, where the photoionization is powered by ultra violet radiation from young, massive stars. This limits the intensity of collisionally excited lines (e.g. [O III] $\lambda\,5007$, [N II] $\lambda\,6584$ and [S II] $\lambda\lambda\,6717, 31$) with respect to recombination lines like Hα and Hβ. On the other hand, lines from AGN are ionized by harder radiation fields, yielding intense collisionally excited lines (Stasinska et al., 2006). The large brightness of AGN arise from a centrally located accreting black hole, and the in-falling gaseous material release potential energy. The luminosity of an AGN is proportional to the accretion rate, $L_{\rm AGN} \propto \dot{M}_{\rm BH}$, and can in some cases outshine their host galaxy. Seyferts are one of the two largest groups of active galaxies, along with quasars, and their spectra reveal strong, high-ionisation emission lines (e.g. [O III] $\lambda\,5007$) (Schneider, 2014). Spectra of low ionization narrow emission line region (hereafter LINER) galaxies has a great resemblance to those of Seyferts, but show lower ionization levels. LINERs have nuclear optical spectra dominated by emission from low ionization species like [O I] $\lambda\,6300$, [O II] $\lambda\lambda\,3736, 9$ and [S II] $\lambda\lambda\,6717, 31$, whereas emission from [O III] $\lambda\,5007$ is weak (Heckman, 1980). LINERs are very common in galactic nuclei and typical LINER spectra is observed in about 1/3 of nuclear galaxy spectra (e.g. Heckman, 1980; Ho et al., 1997). These spectral characteristics is visually present in the diagnostic diagrams discussed in the following.

Baldwin, Phillips & Terlevich diagrams (Baldwin et al., 1981, hereafter BPT diagrams) are a diagnostic tool for classifying the excitation methods of emission lines, based on the most easily measured lines. Baldwin, Phillips & Terlevich developed an empirical method for distinguishing between active galactic nuclei (AGN) and starburst (H II) types from line flux ratios ([O III] / Hβ, [N II] / Hα, [S II] / Hα, and [O I] / Hα). In order to allow for great practicality, Baldwin et al. (1981) avoided pairs of weak lines, and chose lines close to each other in wavelength (as far as possible) to lessen the effect of errors in reddening correction. In the following, the classification schemes used in this thesis for the [O III] / Hβ versus [S II] / Hα and [O III] / Hβ versus [N II] / Hα line ratio diagrams (hereafter [S II]- and [N II] BPT diagrams, respectively) are outlined.

Kewley et al. (2001) derived the first purely theoretical upper boundary for the region occupied by starbursts based on the optical diagnostic diagrams. The classification scheme is derived from models of a large sample of infrared starburst galaxies, with spectral energy distributions of young star clusters generated by the PEGASE v2.0 code, in combination with photoionization models computed using their MAPPINGS III code. This theoretical upper boundary effectively separate extreme starburst from AGN in both the [S II]- and [N II] BPT diagrams. In this thesis, we use this classification to distinguish composite from AGN in the [N II] BPT diagram.
Kauffmann et al. (2003) derived a demarcation between SF- and AGN galaxies through examination of the properties of host galaxies of 22,623 narrow-line AGN from SDSS with $0.02 < z < 0.3$. This pure star formation line is used in this thesis to separate SF and AGN-like regions in both the [S II]- and [N II] BPT diagrams.
Kewley et al. (2006) analyzed the host properties of 85,224 emission-line galaxies selected from SDSS. In this work, they derived a method to separate galaxies into H II-region-like,

Seyferts, LINERs, and composite H II–AGN types using [O III] / Hβ to [S II] / Hα line ratios. This classification, which they denote the Seyfert–LINER line, is in this thesis used to separate Seyfert from LINER in the [S II] BPT diagram.
Using the classification schemes above (Kewley et al., 2001; Kauffmann et al., 2003; Kewley et al., 2006), spaxels of the observed galaxies are classified according the regions defined in the following.

SF galaxies are found in the regions

$$\log\left(\frac{[\mathrm{O\,III}]}{\mathrm{H}\beta}\right) < \frac{0.61}{\log\left(\frac{[\mathrm{N\,II}]}{\mathrm{H}\alpha}\right) - 0.05} + 1.3 \tag{2.15}$$

$$\log\left(\frac{[\mathrm{O\,III}]}{\mathrm{H}\beta}\right) < \frac{0.72}{\log\left(\frac{[\mathrm{S\,II}]}{\mathrm{H}\alpha}\right) - 0.32} + 1.30 \tag{2.16}$$

where the first equation is derived by Kauffmann et al. (2003), and the second by Kewley et al. (2001).

Composite galaxies are found in the regions

$$\log\left(\frac{[\mathrm{O\,III}]}{\mathrm{H}\beta}\right) > \frac{0.61}{\log\left(\frac{[\mathrm{N\,II}]}{\mathrm{H}\alpha}\right) - 0.05} + 1.3 \tag{2.17}$$

$$\log\left(\frac{[\mathrm{O\,III}]}{\mathrm{H}\beta}\right) < \frac{0.61}{\log\left(\frac{[\mathrm{N\,II}]}{\mathrm{H}\alpha}\right) - 0.47} + 1.19 \tag{2.18}$$

where the first equation is derived by Kauffmann et al. (2003), and the second by Kewley et al. (2001).

Seyfert galaxies are found in the regions

$$\log\left(\frac{[\mathrm{O\,III}]}{\mathrm{H}\beta}\right) > \frac{0.61}{\log\left(\frac{[\mathrm{N\,II}]}{\mathrm{H}\alpha}\right) - 0.47} + 1.19 \tag{2.19}$$

$$\log\left(\frac{[\mathrm{O\,III}]}{\mathrm{H}\beta}\right) > \frac{0.72}{\log\left(\frac{[\mathrm{S\,II}]}{\mathrm{H}\alpha}\right) - 0.32} + 1.30 \tag{2.20}$$

$$\log\left(\frac{[\mathrm{O\,III}]}{\mathrm{H}\beta}\right) > 1.89 \log\left(\frac{[\mathrm{S\,II}]}{\mathrm{H}\alpha}\right) + 0.76 \tag{2.21}$$

where the first and second equation is derived by Kewley et al. (2001), and the third by Kewley et al. (2006).

LINERs are found in the regions

$$\log\left(\frac{[\mathrm{O\,III}]}{\mathrm{H}\beta}\right) > \frac{0.61}{\log\left(\frac{[\mathrm{N\,II}]}{\mathrm{H}\alpha}\right) - 0.47} + 1.19 \tag{2.22}$$

$$\log\left(\frac{[\mathrm{O\,III}]}{\mathrm{H}\beta}\right) > \frac{0.72}{\log\left(\frac{[\mathrm{S\,II}]}{\mathrm{H}\alpha}\right) - 0.32} + 1.30 \tag{2.23}$$

$$\log\left(\frac{[\mathrm{O\,III}]}{\mathrm{H}\beta}\right) < 1.89 \log\left(\frac{[\mathrm{S\,II}]}{\mathrm{H}\alpha}\right) + 0.76 \tag{2.24}$$

where the first and second equation is derived by Kewley et al. (2001), and the third by Kewley et al. (2006).

The BPT diagrams for the observed galaxies are shown in figures B.2 and 2.5, diagnostic maps of the observed galaxies are shown in figures 2.4 and 2.3, and the division between the categories is summed up in table 2.2. The data is extinction corrected and selected upon a SNR> 3 for Hα, [O III], [N II] and [S II] and a SNR > 2 for Hβ.

Both diagnostics for NGC 925 in figures 2.3 and 2.4 indicate a galactic center dominated by SF regions. The disk, however, is occupied by AGN-like regions (LINER and Seyfert) as seen from the [S II] BPT map in figure 2.4. Kewley et al. (2013) associates this extended LINER emission (> 1 kpc) with shock excitation.
The [S II] BPT map of the starburst NGC 1569 shows outer regions heavily occupied by Seyfert emission, while the [N II] diagnostic classify the vast majority of spaxels as SF, with some spaxels in the outer region falling into the composite- and AGN category. The explanation provided by Kewley et al. (2013) is also valid in this case, as shock waves are a great contributor to starbursts.
NGC 4214, which is shown in a false color image on the front page, exhibit many of the same trends as NGC 1569. NGC 4214 is known for its large SF regions in the center, which is also reflected in the Hα map seen in figure 2.2.
NGC 5194, commonly known as the Whirlpool Galaxy, is an interacting galaxy with a Seyfert 2 AGN in the center. The AGN is nicely illustrated in both diagnostic maps in figures 2.3 and 2.4. NGC 5194 is connected to its companion dwarf galaxy, NGC 5195, by a dust-rich tidal bridge. Tidal winds from the gravitational interaction compress gas along the spiral arms of NGC 5194, feeding star formation as is seen in figure 2.2.
The [N II] BPT map of both NGC 6946 and NGC 7331 show a significant number of spaxels classified as composite. From shock models, Kewley et al. (2013) argues how galaxies with contributions from both fast shocks and star formation can mimic composite SF-AGN galaxies at this redshift.

	NGC 925	NGC 1569	NGC 4214	NGC 5194	NGC 6946	NGC 7331
[N II] BPT						
SF	98.79%	93.99%	99.44%	50.58%	91.24%	70.71%
Composite	1.15%	5.06%	0.4%	37.6%	8.15%	27.71%
AGN	0.06%	0.95%	0.16%	11.55%	0.61%	1.59%
[S II] BPT						
SF	86.57%	68.73%	77.11%	90.2%	99.02%	95.82%
LINER	7.06%	1.03%	13.17%	9.03%	0.37%	3.26%
Seyfert	6.36%	30.24%	9.72%	0.78%	0.61%	0.92%

Table 2.2: Results from BPT diagnostics as described in section 2.1.4. The [N II] vs. [O III] utilizes $\lambda\,6584$ and $\lambda\,5007$, and the [S II] vs. [O III] utilizes $\lambda\lambda\,6717, 31$ and $\lambda\,5007$.

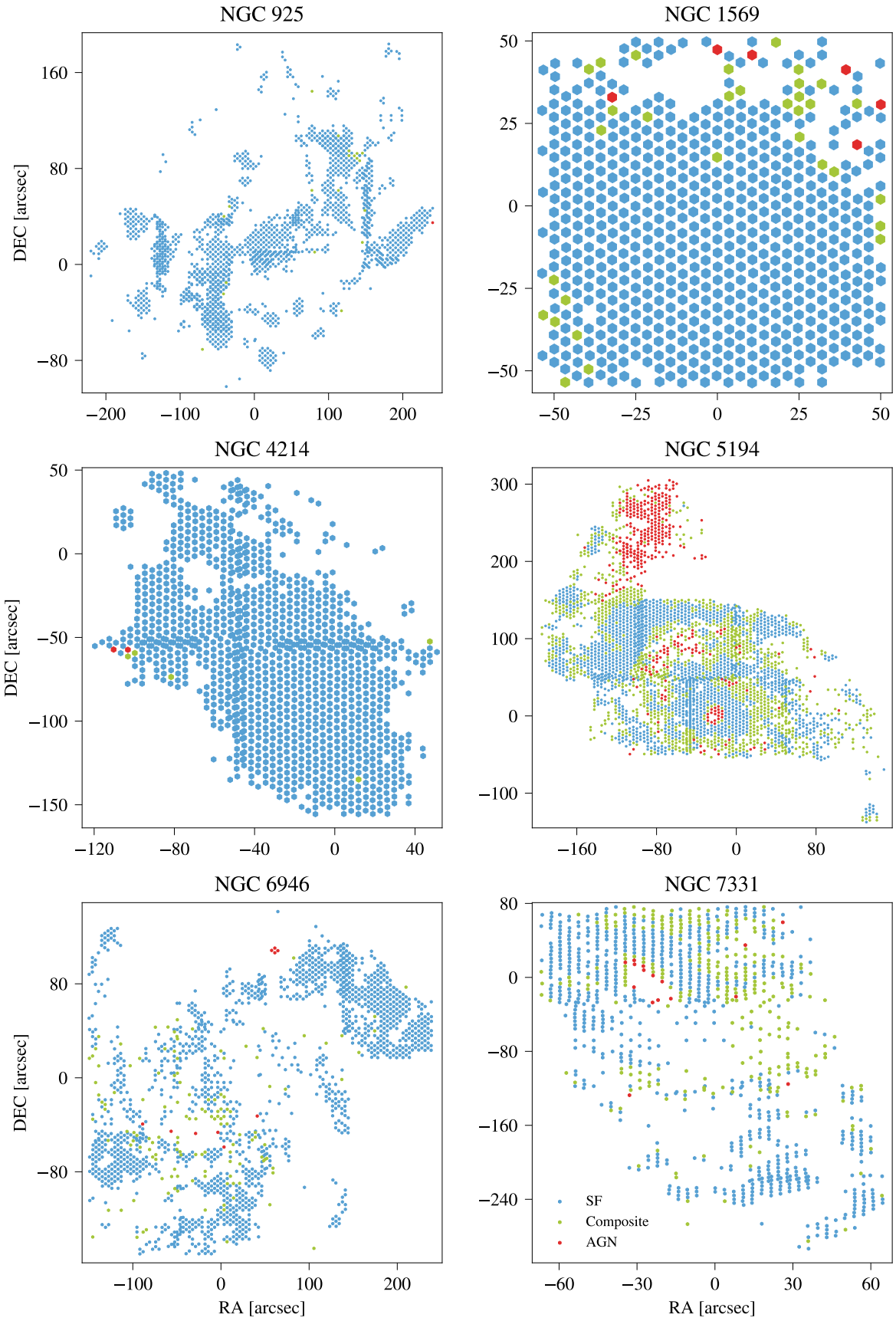

Figure 2.3: [N II] BPT diagnostic maps for the observed galaxies (see page 19).

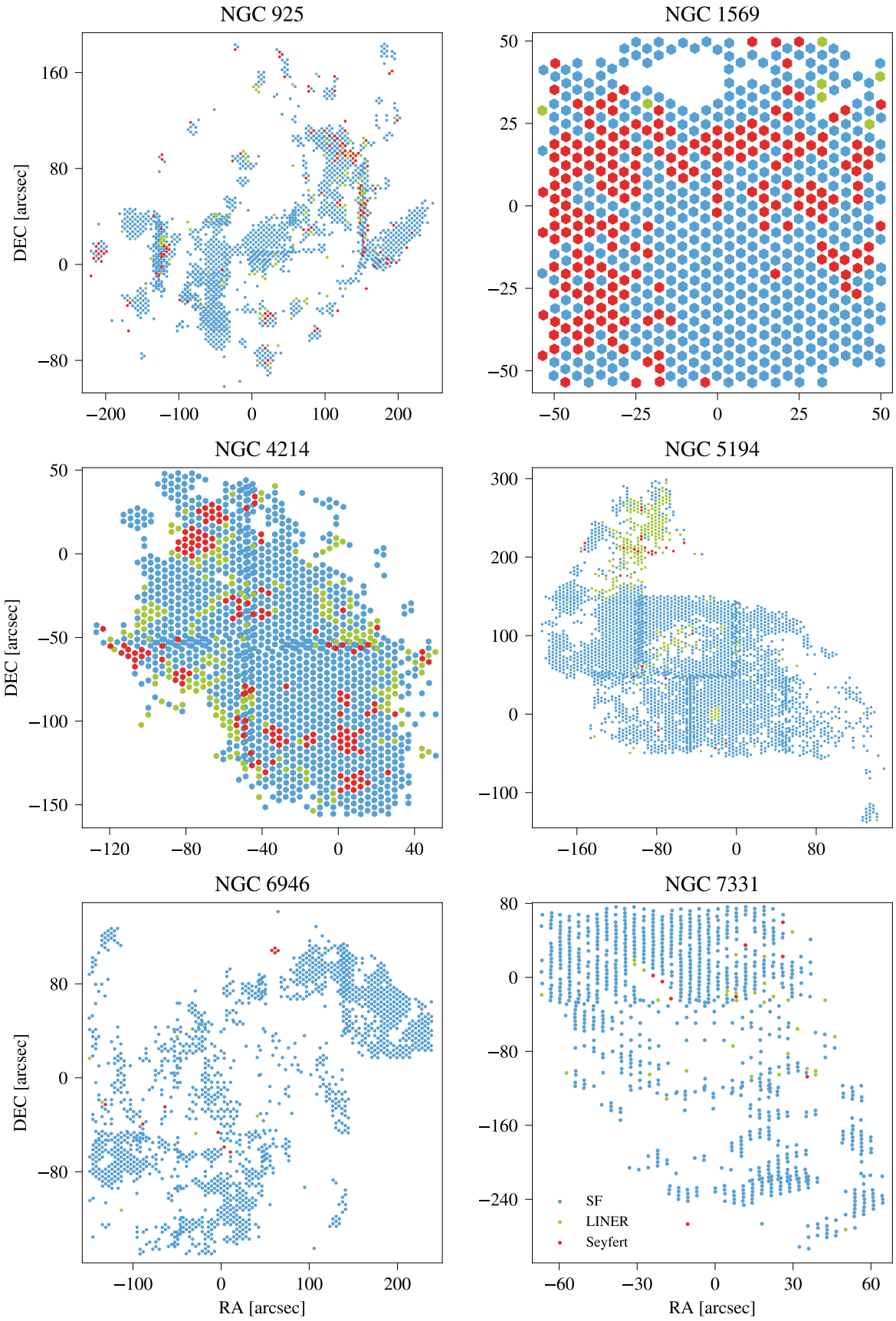

Figure 2.4: [S II] BPT diagnostic maps for the observed galaxies (see page 19).

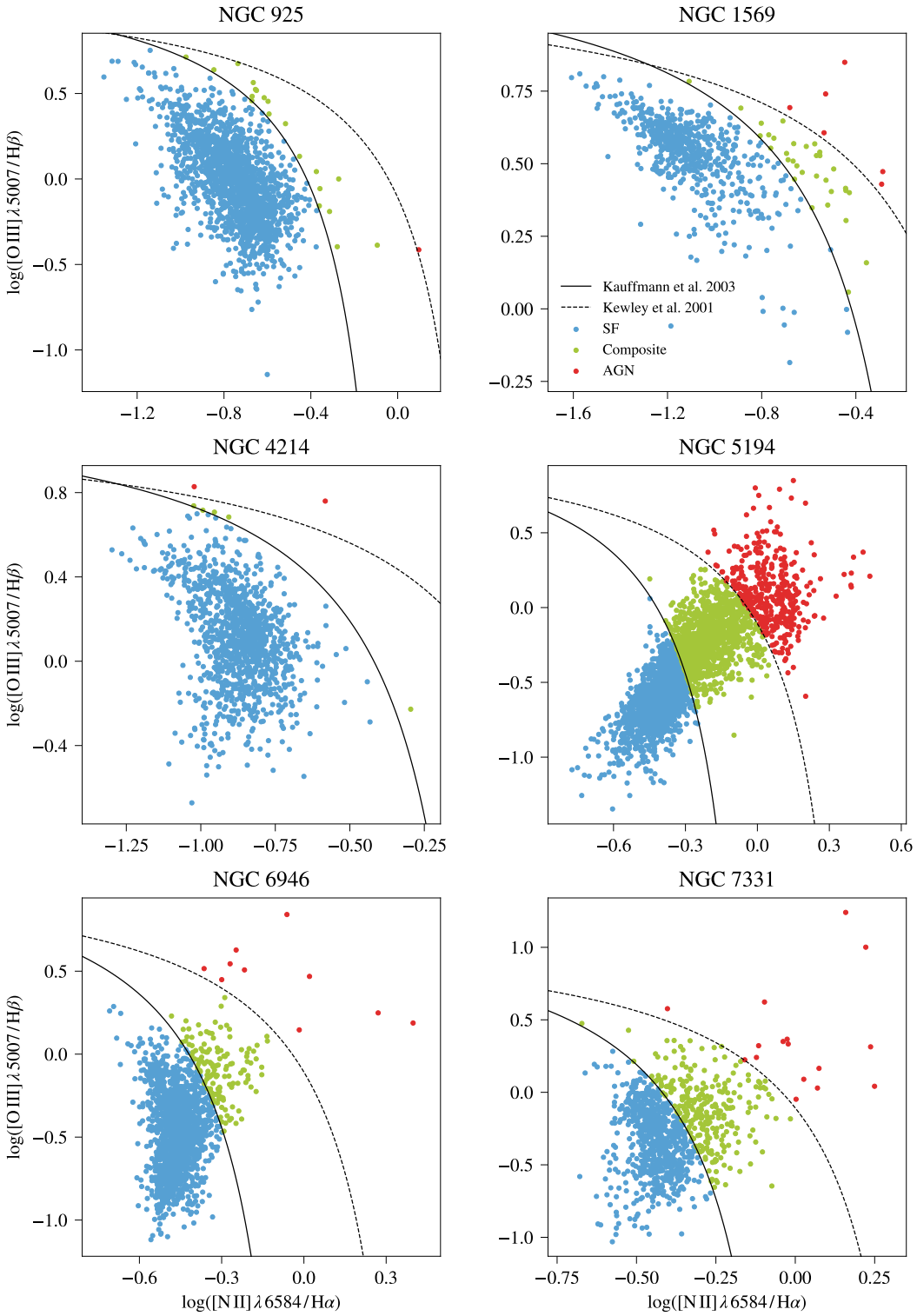

Figure 2.5: [N II] BPT diagrams for the observed galaxies. Regions are classified according to equations (2.15) - (2.24).

2.1.5 Estimation of Gas Metallicity and Ionization Parameter

In this thesis, gas metallicity and ionization parameter are estimated for the extinction corrected IFS data, for spaxels selected with a SNR > 3. SF galaxies are selected from the [N II] BPT diagram, and so the classification from section 2.1.4 will be used to select only SF spaxels.

In the following, I will use the notations for the line ratios and excitation parameter (P) as defined by Pilyugin and Grebel (2016).

$$\begin{aligned} S_2' &= I_{[\mathrm{S\,II}]\,\lambda\lambda\,6717,31} \,/\, I_{\mathrm{H}\alpha} \\ S_2 &= I_{[\mathrm{S\,II}]\,\lambda\lambda\,6717,31} \,/\, I_{\mathrm{H}\beta} \\ N_2 &= I_{[\mathrm{N\,II}]\,\lambda\lambda\,6548,84} \,/\, I_{\mathrm{H}\beta} \\ R_2 &= I_{[\mathrm{O\,II}]\,\lambda\lambda\,3927,29} \,/\, I_{\mathrm{H}\beta} \\ R_3 &= I_{[\mathrm{O\,III}]\,\lambda\lambda\,4959,5007} \,/\, I_{\mathrm{H}\beta} \\ R_{23} &= R_2 + R_3 \\ P &= R_3/R_{23} = R_3/(R_2 + R_3) \end{aligned} \tag{2.25}$$

Metallicity Estimation

The T_e method provides a direct and accurate estimate metallicities. The idea is to use line ratios with a strong temperature dependance, with lines of similar strengths and close together in wavelength. The optical lines [O III] λ4363 and [O III] $\lambda\lambda$4959, 5007 are excited by collisions with thermal electrons, and are emitted from the same ion but have different excitation energies. Their relative excitation rates are thus temperature dependant; [O III] λ4363 has higher excitation energy and, relative to [O III] $\lambda\lambda$4959, 5007, tends to be emitted in higher-temperature environments (e.g. Spitzer, 1998; Peimbert, 1967). The electron temperature T_e can thereby be measured using their relative line strengths(Léna et al., 2012):

$$\frac{I(\lambda4959 + \lambda5007)}{I(\lambda4363)} = \frac{7.90\,\exp\left(3.29 \times 10^4\, T_\mathrm{e}^{-1}\right)}{1 + 4.5 \times 10^{-4}\; n_\mathrm{e}\, T_\mathrm{e}^{-1/2}} \tag{2.26}$$

such that larger $I(\lambda4959 + \lambda5007)\,/\,I(\lambda4363)$ yield lower T_e. In oxygen-rich H II regions, however, detection of temperature sensitive lines like [O III] λ4363 is challenging, as they are simply too weak (Pilyugin, 2001). Instead, several empirical methods using strong emission lines have been developed. One of them is the R_{23} method

$$R_{23} = \frac{[\mathrm{O\,II}]\,\lambda\lambda3727, 29 + [\mathrm{O\,III}]\,\lambda\lambda4959, 5007}{\mathrm{H}\beta} \tag{2.27}$$

However, different calibrations using R_{23} present large scatters ($\sim$ 0.3 dex), and are subject to both random- and systematic errors, with the latter being dependant on the ionization parameter. The T_e method naturally takes into account these physical conditions, but the R_{23} method does not (Pilyugin, 2000).

Pilyugin and Grebel (2016) has designed a simple metallicity calibration using the strong lines N_2, S_2 and R_3 as given in (2.25). The basis of this method is that the N_2 line intensity is an indicator of T_e in H II regions, being a monotonic function of $\log(N_2)$. The $T_\mathrm{e} - \log(N_2)$ relation (Pilyugin and Grebel, 2016, figure 2, panel a3) has a noticeable dependence on the excitation parameter P (equation 2.25) at high electron temperatures, with no appreciable dependence present at low T_e. The oxygen and nitrogen abundances both present clear monotonic relations with $\log(N_2)$ (Pilyugin and Grebel, 2016, figure 2, panels a1 and a2, respectively), with both relations exhibiting a dependence on P at high and low metallicities X/H (i.e. high T_e), where

X/H may denote the abundances $12 + \log(\mathrm{O/H})$ and $12 + \log(\mathrm{N/H})$.
The excitation level of hot H II regions is usually higher, while it is lower in cool H II regions. The magnitude of P likewise reflects the temperature of the H II region (and thus, the emission contribution from low ionization zones to the total emission of a H II region), with variations in P of hot H II regions corresponding to greater changes in the contribution from low ionization zones to the total emission than in cool H II regions. The dependencies of $T_\mathrm{e} - N_2$ and $\mathrm{X/H} - N_2$ on P may therefore be assumed to reflect the contribution of low ionization zones. Hence, the oxygen abundance depends on both the electron temperature T_e and the level of excitation P (or, equivalently, R_2 and R_3), with a shift at $\log(N_2) \sim -0.6$. To account for these dependencies, Pilyugin and Grebel (2016) divides the metallicity calibration into two branches at $\log(N_2) = -0.6$, with an upper branch $(\mathrm{O/H})^*_\mathrm{U}$ ($\log(N_2) \geqslant -0.6$) and a lower branch $(\mathrm{O/H})^*_\mathrm{L}$ ($\log(N_2) < -0.6$). The resulting calibrations is based on the sulphur S_2 line intensity as noted in equation (2.25) (thereby the name "S calibration"), and takes into account the correlation with the ionization parameter. In this work, the metallicity calibration is carried out following the S calibration of Pilyugin and Grebel (2016, hereafter PG16), with the relations for the upper- $(\mathrm{O/H})^*_\mathrm{U}$ and lower $(\mathrm{O/H})^*_\mathrm{L}$ branch being

$$\begin{aligned}(\mathrm{O/H})^*_U =& 8.424 + 0.030 \log\left(\frac{R_3}{S_2}\right) + 0.751 \log(N_2) \\ &+ \left[-0.349 + 0.182 \log\left(\frac{R_3}{S_2}\right) + 0.508 \log(N_2)\right] \times \log(S_2)\end{aligned} \tag{2.28}$$

$$\begin{aligned}(\mathrm{O/H})^*_L =& 8.072 + 0.789 \log\left(\frac{R_3}{S_2}\right) + 0.726 \log(N_2) \\ &+ \left[1.069 - 0.170 \log\left(\frac{R_3}{S_2}\right) + 0.022 \log(N_2)\right] \times \log(S_2)\end{aligned} \tag{2.29}$$

where $(\mathrm{O/H})^*_i = 12 + \log(\mathrm{O/H})_i$. It should be noted that PG16 is compatible with the typical metallicity scales of H II regions, and in general show a smaller scatter compared to calibrations using auroral lines such as [O III] λ4363, [N II] λ5755, and [S III] λ6312.

The gas metallicity was estimated using the PG16 calibration, and the corresponding maps are shown in figure 2.6.

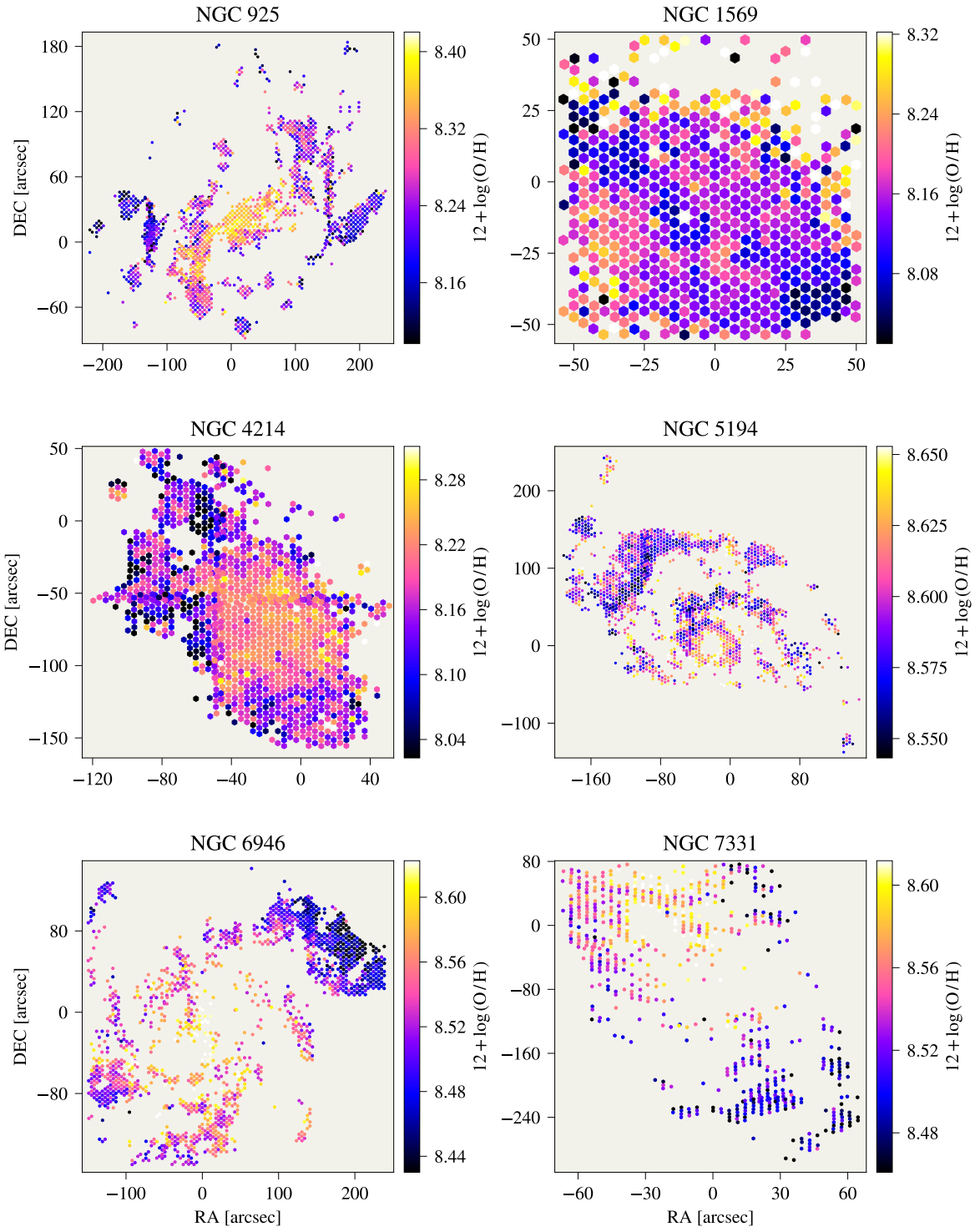

Figure 2.6: Metallicity maps of the observed galaxies. The spaxels are corrected for extinction, filtered by SNR > 3, categorized as SF from the [N II] diagnostic in section 2.1.4.

Ionization Parameter

The ionization parameter (U) is estimated following Dors et al. (2016), with U being a linear function of S_2' and the linear coefficients a and b being functions of metallicity Z (equations 2.32 and 2.33). They deployed a grid of 180 photoionization models build using the photoionization code CLOUDY (Ferland et al., 2013), to derive the calibrations among

- The effective temperature of the radiation field arising from the ionizing stars, $T_{\rm eff}$
- The ionization parameter, U
- Strong emission lines which are observable in H II regions

Effective temperatures in the range $2500\,\mathrm{K} \leqslant T_{\rm eff} \leqslant 30{,}000\,\mathrm{K}$ are considered in the photoionization models, and are estimated using the R index

$$R = \log\left(\frac{[\mathrm{O\,II}]\,\lambda\lambda 3727,29}{[\mathrm{O\,III}]\,\lambda 5007}\right) \tag{2.30}$$

of which its relation with $T_{\rm eff}$ exhibits a strong dependence on U. In their photoionization models, the ionization parameter U is defined by

$$\mathrm{U} = \frac{Q_{\rm ion}}{4\,\pi\,R_{\rm in}^2\,n\,c} \tag{2.31}$$

where $Q_{\rm ion}$ denotes the number of hydrogen ionizing photons ($h\nu \geqslant 13.6$ eV) emitted per second by the ionizing source and $R_{\rm in}$ is the distance from the inner surface of the ionized gas cloud to the source measured in cm. The particle density n is measured in cm^{-3} and c is the speed of light (Dors et al., 2016).

As the line ratio S_2' (equation (2.25)) has a relatively low dependence on ($T_{\rm eff}$, Dors et al. (2016) use S_2' in their estimates of U. The resulting linear relation of $\log(\mathrm{U}) - S_2'$ is

$$\log(\mathrm{U}) = a\,(Z/Z_\odot) \times S_2' + b \tag{2.32}$$

where $Z_\odot = 8.69$ and

$$\begin{aligned} a &= -0.26\,(\pm 0.04) \times (Z/Z_\odot) - 1.54\,(\pm 0.02) \\ b &= -3.69\,(\pm 1.79) \times (Z/Z_\odot)^2 + 5.11\,(\pm 1.96) \times (Z/Z_\odot) - 5.26\,(\pm 0.36) \end{aligned} \tag{2.33}$$

The models of Dors et al. (2016) considered values of $-3.5 \leqslant \log(\mathrm{U}) \leqslant -1.5$ and $0.03 \leqslant \log(Z/Z_\odot) \leqslant 1.0$, and the vast majority of our measurements fall in this range. The ionization parameter was estimated using Dors et al. (2016), and the obtained maps are shown in figure 2.7.

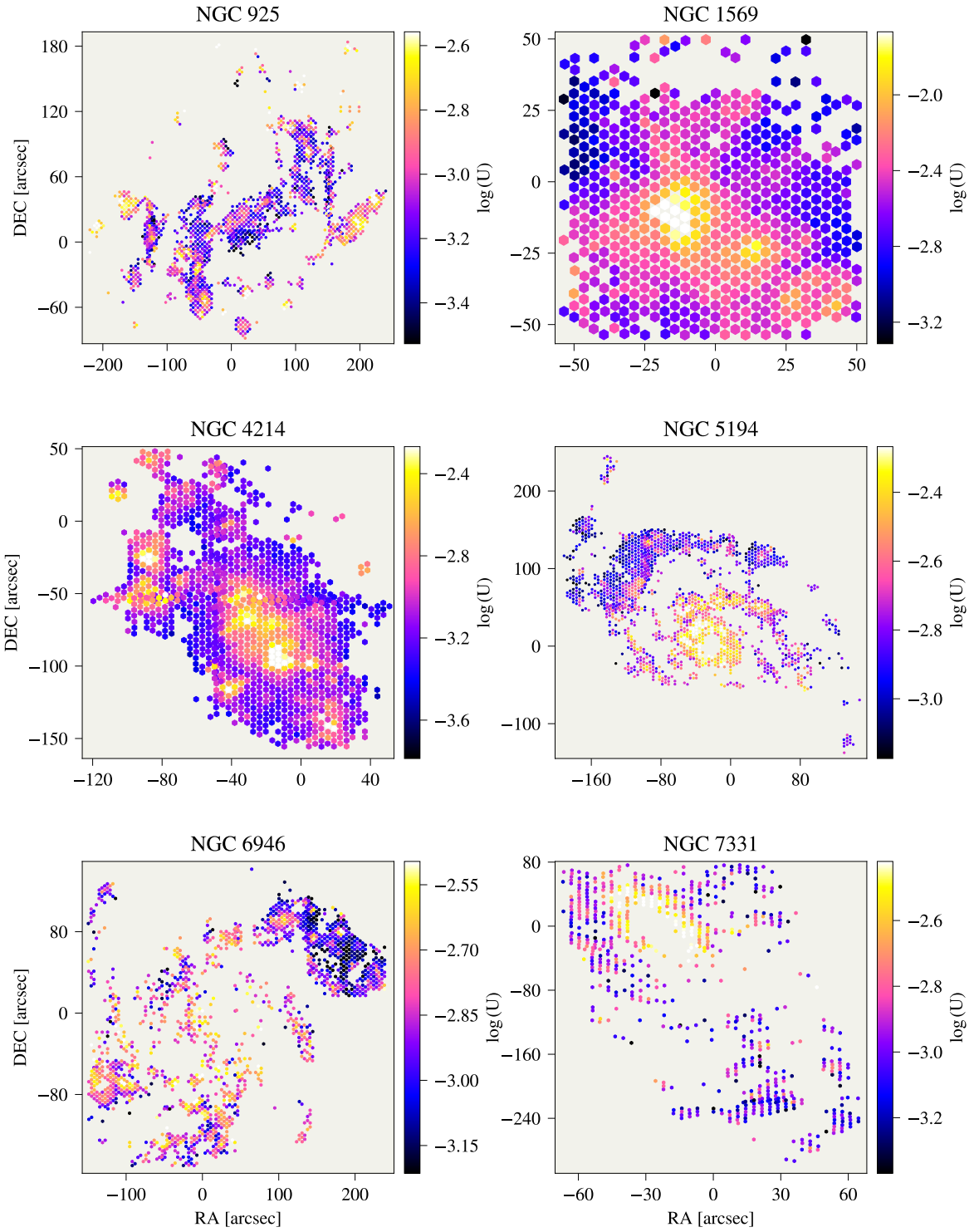

Figure 2.7: Ionization maps of the observed galaxies. The spaxels are corrected for extinction, filtered by SNR > 3, categorized as SF from the [N II] diagnostic in section 2.1.4.

2.1.6 Observed Metallicity- and Ionization Gradients

Deriving the Radial Metallicity and Ionization Profiles

To determine the gradients of the observed galaxies, the radial distance from the galactic center to the spaxels are found as

$$R = \sqrt{x^2 + y^2} \tag{2.34}$$

where x and y are the spaxel coordinates corrected for the positional angle ϕ and inclination i so that they correspond to the face-on coordinates. This is done as

$$x = x' \cos(\phi) - y' \sin(\phi) \tag{2.35}$$
$$y = x' \sin(\phi) + y' \cos(\phi) \tag{2.36}$$

with

$$x' = [(\mathrm{RA} - \mathrm{RA}_0) \cos(\phi) + (\mathrm{DEC} - \mathrm{DEC}_0) \sin(\phi)] \,/\, \cos(i) \tag{2.37}$$
$$y' = -(\mathrm{RA} - \mathrm{RA}_0) \sin(\phi) + (\mathrm{DEC} - \mathrm{DEC}_0) \cos(\phi) \tag{2.38}$$

where RA_0 and DEC_0 are the central coordinates of the galaxy. The positional angle ϕ, inclination i, the isophotal radius R_{25}[1] as well as the central coordinates for all observed galaxies are given in table 2.3.

All gradients were fitted using a χ^2 minimization routine based on course material from Michelsen and Petersen (2018), using the Python module IMINUIT v1.5.4 (Dembinski et al., 2021). The metallicity- and ionization gradients in units of [dex/R_e] are shown in figures 2.8 and 2.9, and the corresponding gradients in units of [dex/R_{25}] and [dex/kpc] can be found in appendix C in figures C.1 through C.4. The total metallicities and ionization parameters are given in table 2.4, while the fit ranges are given in tables 2.5 and 2.6. The fitting parameters of the obtained gradients are summarised in table 2.7, together with the root mean square error (RMSE), defined as:

$$\mathrm{RMSE} = \sqrt{\frac{\sum_{i=1}^{N} (\hat{y}_i - y_i)^2}{N}} \tag{2.39}$$

where $\hat{y}_i$ are the predicted values, y_i the observed values, and N the number of points in the fit region, as noted in tables 2.5 and 2.6.

	NGC 925	NGC 1569	NGC 4214	NGC 5194	NGC 6946	NGC 7331
R_{25} [kpc]	13.51	0.756	2.86	12.79	8.38	17.81
R_e [kpc]	7.11	1	1.17	5.89	5.51	8.04
ϕ [°]	293.3	0	126	172	243	166.3
i [°]	68.7	0	27	20	33	73.1
RA_0 [″]	9.1	0	−2.52	0	0	13.2
DEC_0 [″]	−38.9	0	2.98	0	0	−26.5

Table 2.3: Information on the observed galaxies. The meaning of the parameters are as follows: R_{25} is the isophotal radius in kpc, R_e is the effective radius in kpc, ϕ is the position angle in degrees, i is the inclination in degrees, RA_0 is the right ascension of the central spaxel in arcseconds, and DEC_0 is the declination of the central spaxel, also in arcseconds.

[1]The isophotal radius R_{25} refers to the radius at which the surface brightness in the B band has a value of $S_B = 25$ mag arcsec^2.

	NGC 925	NGC 1569	NGC 4214	NGC 5194	NGC 6946	NGC 7331
$12 + \log(\mathrm{O/H})$	8.28 ± 0.08	8.16 ± 0.1	8.2 ± 0.07	8.59 ± 0.03	8.55 ± 0.05	8.56 ± 0.05
$\log(\mathrm{U})$	-3.0 ± 0.3	-2.2 ± 0.3	-2.7 ± 0.3	-2.6 ± 0.2	-2.8 ± 0.2	-2.7 ± 0.2

Table 2.4: Total (i.e. integrated) metallicity and ionization parameter $\pm 1\sigma$ of the observed galaxies.

$12 + \log(\mathrm{O/H})$	NGC 925	NGC 1569	NGC 4214	NGC 5194	NGC 6946	NGC 7331
$R_{\nabla[\mathrm{dex}/R_{25}]}$	$2.08\,R_{25}$ 28.1 kpc	$0.93\,R_{25}$ 0.7 kpc	$0.91\,R_{25}$ 2.6 kpc	$0.87\,R_{25}$ 11.13 kpc	$0.93\,R_{25}$ 7.79 kpc	$1.64\,R_{25}$ 29.21 kpc
$R_{\nabla[\mathrm{dex}/R_{\mathrm{e}}]}$	$3.95\,R_{\mathrm{e}}$ 28.08 kpc	$0.7\,R_{\mathrm{e}}$ 0.7 kpc	$2.22\,R_{\mathrm{e}}$ 2.6 kpc	$1.89\,R_{\mathrm{e}}$ 11.13 kpc	$1.42\,R_{\mathrm{e}}$ 7.82 kpc	$3.62\,R_{\mathrm{e}}$ 29.1 kpc
$R_{\nabla[\mathrm{dex/kpc}]}$	28.08 kpc	0.7 kpc	2.6 kpc	11.13 kpc	7.82 kpc	29.14 kpc

Table 2.5: Fit ranges used for obtaining the metallicity gradients listed in table 2.7. The leftmost column describes what normalization is considered for the gradient, while the rest defines the used fit ranges in units of both R_{25}, R_{e} and kpc.

$\log(\mathrm{U})$	NGC 925	NGC 1569	NGC 4214	NGC 5194	NGC 6946	NGC 7331
$R_{\nabla[\mathrm{dex}/R_{25}]}$	$2.08\,R_{25}$ 28.1 kpc	$0.93\,R_{25}$ 0.71 kpc	$0.91\,R_{25}$ 2.6 kpc	$0.93\,R_{25}$ 11.89 kpc	$0.93\,R_{25}$ 7.79 kpc	$1.64\,R_{25}$ 29.21 kpc
$R_{\nabla[\mathrm{dex}/R_{\mathrm{e}}]}$	$3.95\,R_{\mathrm{e}}$ 28.08 kpc	$0.71\,R_{\mathrm{e}}$ 0.71 kpc	$2.22\,R_{\mathrm{e}}$ 2.6 kpc	$2.03\,R_{\mathrm{e}}$ 11.96 kpc	$1.42\,R_{\mathrm{e}}$ 7.82 kpc	$3.62\,R_{\mathrm{e}}$ 29.1 kpc
$R_{\nabla[\mathrm{dex/kpc}]}$	28.08 kpc	0.71 kpc	2.6 kpc	11.95 kpc	7.82 kpc	29.14 kpc

Table 2.6: Fit ranges used for obtaining the ionization parameter gradients listed in table 2.7. The leftmost column describes what normalization is considered for the gradient, while the rest defines the used fit ranges in units of both R_{25}, R_{e} and kpc.

[dex/R_{25}]	$\alpha_{O/H}$	$\beta_{O/H}$	$RMSE_{O/H}$	α_U	β_U	$RMSE_U$
NGC 925	-0.1 ± 0.01	8.32 ± 0.01	0.076	0.18 ± 0.02	-3.12 ± 0.01	0.24
NGC 1569	0.01 ± 0.03	8.16 ± 0.02	0.078	-0.47 ± 0.04	-2.23 ± 0.02	0.255
NGC 4214	-0.06 ± 0.03	8.22 ± 0.02	0.077	0.04 ± 0.04	-2.95 ± 0.02	0.271
NGC 5194	-0.04 ± 0.02	8.608 ± 0.007	0.027	-0.83 ± 0.03	-2.4 ± 0.01	0.177
NGC 6946	-0.17 ± 0.02	8.62 ± 0.01	0.034	-0.4 ± 0.03	-2.63 ± 0.02	0.163
NGC 7331	-0.07 ± 0.02	8.59 ± 0.01	0.043	-0.23 ± 0.03	-2.72 ± 0.02	0.223

[dex/R_e]	$\alpha_{O/H}$	$\beta_{O/H}$	$RMSE_{O/H}$	α_U	β_U	$RMSE_U$
NGC 925	-0.045 ± 0.008	8.32 ± 0.01	0.076	0.092 ± 0.01	-3.12 ± 0.01	0.24
NGC 1569	0.01 ± 0.05	8.16 ± 0.02	0.078	-0.62 ± 0.05	-2.23 ± 0.02	0.255
NGC 4214	-0.02 ± 0.01	8.22 ± 0.02	0.077	0.02 ± 0.02	-2.95 ± 0.02	0.271
NGC 5194	-0.017 ± 0.008	8.608 ± 0.007	0.027	-0.38 ± 0.01	-2.4 ± 0.01	0.177
NGC 6946	-0.11 ± 0.01	8.62 ± 0.01	0.034	-0.26 ± 0.02	-2.63 ± 0.02	0.163
NGC 7331	-0.032 ± 0.008	8.59 ± 0.01	0.043	-0.1 ± 0.01	-2.72 ± 0.02	0.223

[dex/kpc]	$\alpha_{O/H}$	$\beta_{O/H}$	$RMSE_{O/H}$	α_U	β_U	$RMSE_U$
NGC 925	-0.006 ± 0.001	8.32 ± 0.01	0.076	0.013 ± 0.001	-3.12 ± 0.01	0.24
NGC 1569	0.01 ± 0.05	8.16 ± 0.02	0.078	-0.62 ± 0.05	-2.23 ± 0.02	0.255
NGC 4214	-0.02 ± 0.01	8.22 ± 0.02	0.077	0.01 ± 0.01	-2.95 ± 0.02	0.271
NGC 5194	-0.003 ± 0.001	8.608 ± 0.007	0.027	-0.065 ± 0.003	-2.4 ± 0.01	0.177
NGC 6946	-0.02 ± 0.003	8.62 ± 0.01	0.034	-0.046 ± 0.004	-2.63 ± 0.02	0.163
NGC 7331	-0.004 ± 0.001	8.59 ± 0.01	0.043	-0.013 ± 0.002	-2.72 ± 0.02	0.223

Table 2.7: Results from χ^2 regression on the metallicity- and ionization gradients of the observed galaxies in units of (from top to bottom): [dex/R_{25}], [dex/R_e] and [dex/kpc]. The meaning of the parameters are as follows: slope of metallicity gradient $\alpha_{O/H}$, normalization of metallicity gradient $\beta_{O/H}$, RMSE of fitted metallicity gradient $RMSE_{O/H}$, slope of ionization gradient α_U, normalization of ionization gradient β_U and RMSE of fitted ionization gradient $RMSE_U$. The linear fit is based on the function $y = \alpha \cdot x + \beta$.

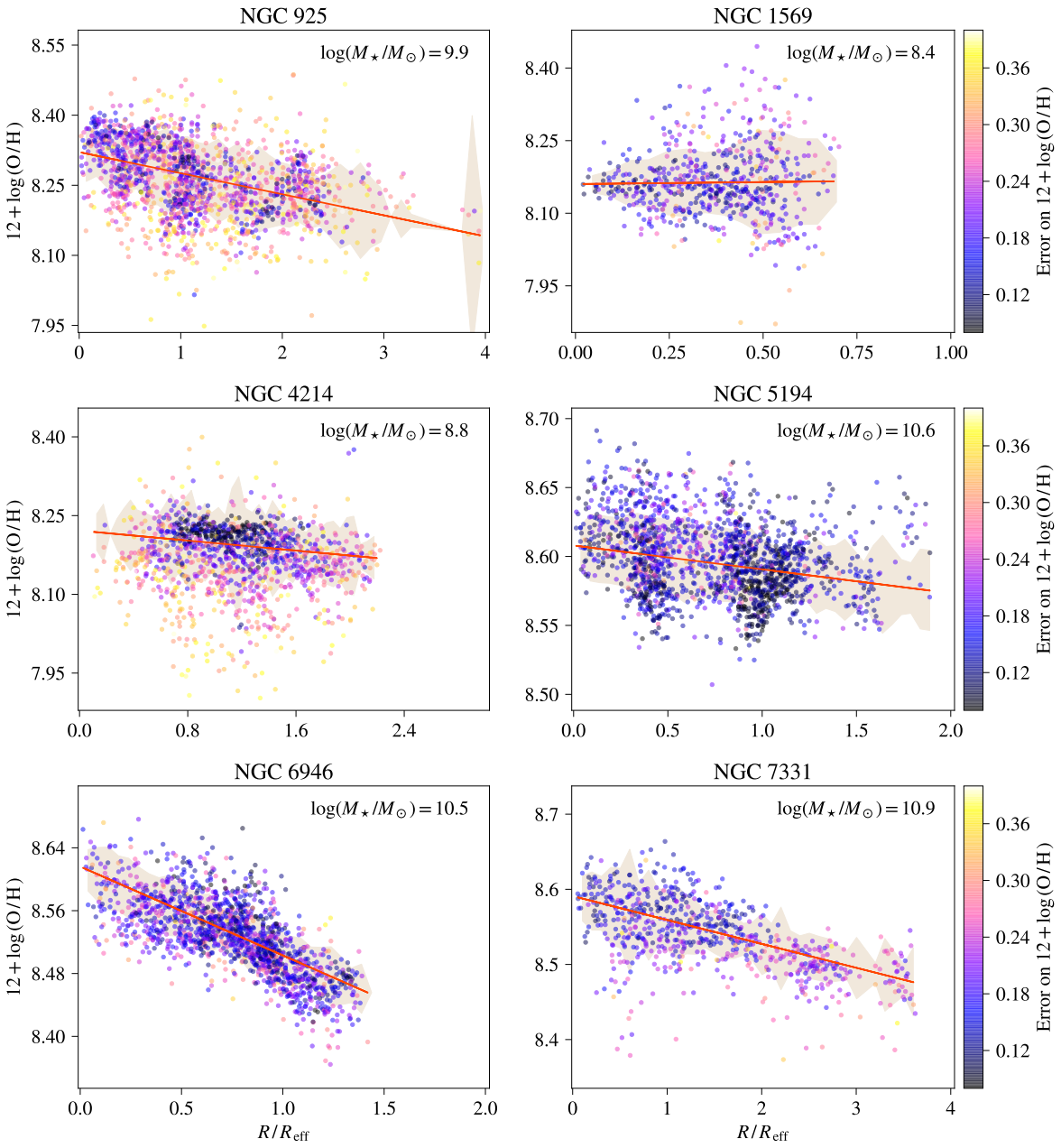

Figure 2.8: Metallicity gradients of the observed galaxies in units of [dex/R_e]. The red line is a linear χ^2 regression, the dots are color coded by error on the metallicity, and the shaded area is a 1σ scatter. All spaxels are corrected for extinction, filtered by SNR > 3, categorized as SF from the [N II] diagnostic in section 2.1.4 and 3σ clipped in log(Hα) to remove outliers.

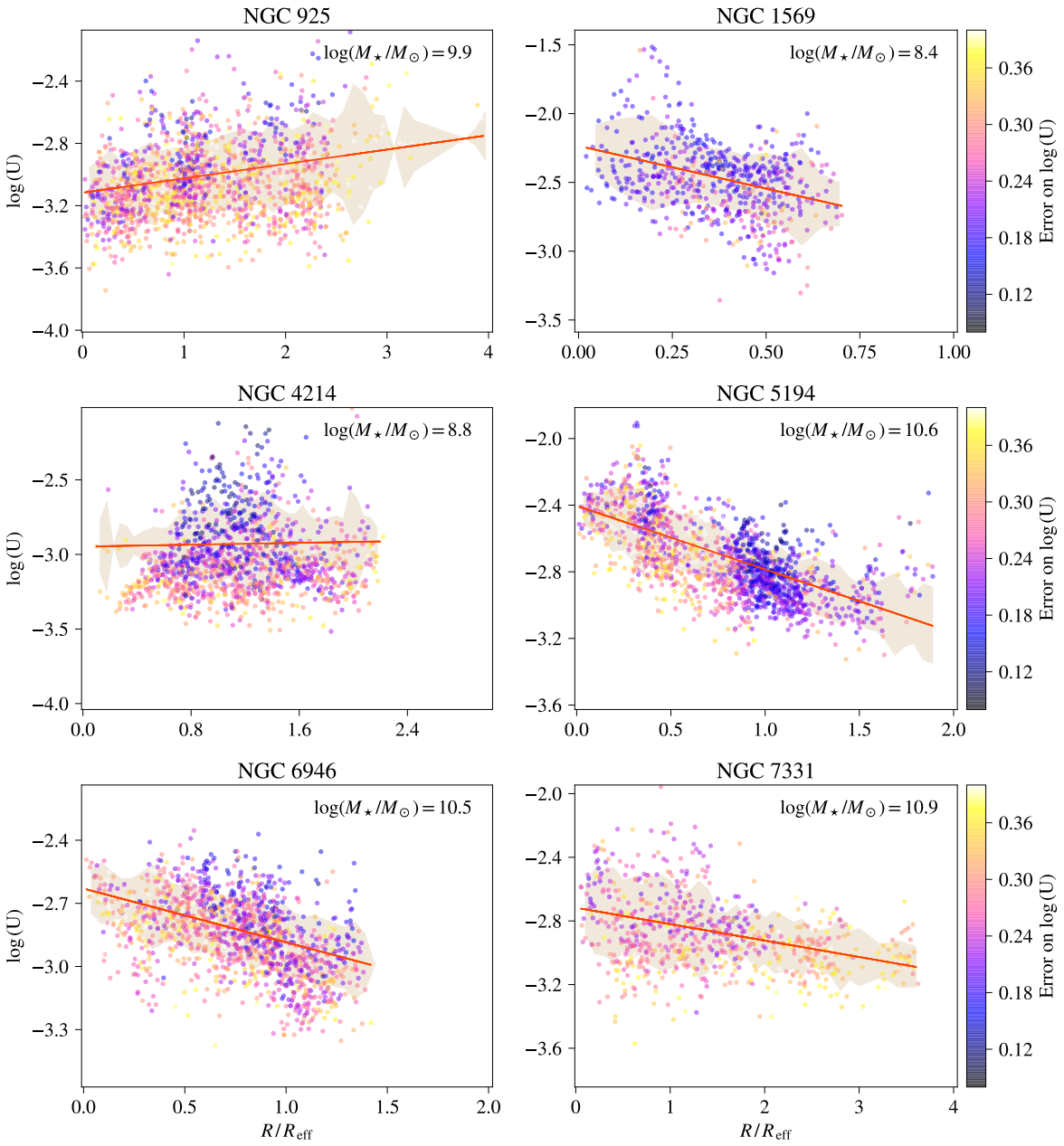

Figure 2.9: Ionization gradients of the observed galaxies in units of [dex/R_e]. The red line is a linear χ^2 regression, the dots are color coded by error on the ionization, and the shaded area is a 1σ scatter. All spaxels are corrected for extinction, filtered by SNR > 3, categorized as SF from the [N II] diagnostic in section 2.1.4 and 3σ clipped in log(Hα) to remove outliers.

Discussion

Metallicity Gradients

It can be seen in table 2.7 that for all observed galaxies, except NGC 1569, the metallicity- and ionization gradients are the flattest in units of [dex/kpc], and steepest in units of [dex/R_{25}]. Only NGC 1569 does not fall into this trend, as the radius used for fitting, measured in both R/R_e, R/R_{25} and kpc, are very close to being equal, that is $(R/R_e)_{max} \sim 0.9$ and $(R/R_{25})_{max} \sim (R/\text{kpc})_{max} \sim 0.7$. Both NGC 1569 and NGC 4214 are irregular dwarf galaxies, and NGC 1569 exhibits a positive, albeit very shallow, metallicity gradient ($\nabla_{O/H\,[dex/R_{25}]} = 0.01 \pm 0.03$), whereas a negative metallicity gradient ($\nabla_{O/H\,[dex/R_{25}]} = -0.06 \pm 0.03$) was measured for NGC 4214. Through a study of three dwarf irregulars and six dwarf spheroidals, Leaman et al. (2014) find that dwarf irregulars show a flattened metallicity ([Fe/H]) gradient, compared to the dwarf spheroidals. They speculate, on the basis of simulations by Schroyen et al. (2011), that higher angular momentum could result in flattened metallicity gradients. The reasoning for this is, that higher angular momentum would prevent gas funneling to the center of the galaxy. This would in turn introduce a more uniform distribution of star formation and chemical enrichment throughout the galaxy. An interesting physical trait of NGC 1569 is that it is smaller than the Small Magellanic Cloud, but brighter than the Large Magellanic Cloud (Karachentsev et al., 2004). This is due to it being a starburst galaxy, which could, together with the flat metallicity gradient (in fact, the flattest of the observed galaxies), imply a higher degree of angular momentum, as hypothesized by Schroyen et al. (2011). As can be seen in table 2.3, the position angle and inclination is set to zero, as these values would not yield any useful information because of the high irregularity of NGC 1569.

NGC 925 is a barred galaxy, and its dynamical center may be slightly offset (~ 1 kpc) from its optical center (Pisano and Wilcots, 1998). From my analysis, I find a negative metallicity gradient for NGC 925 of $\nabla_{O/H\,[dex/R_{25}]} = -0.1 \pm 0.01$ with an RMSE of 0.076, similar to that of Lara-López et al. (2021) $\nabla_{O/H\,[dex/R_{25}]} = -0.0948 \pm 0.0056$ (also using PG16). The obtained ionization gradient $\nabla_{U\,[dex/R_{25}]} = +0.18 \pm 0.02$ with an RMSE of 0.24 is however shallower than the one derived in Lara-López et al. (2021) $\nabla_{U\,[dex/R_{25}]} = +0.3813 \pm 0.0248$ with a RMSE of 0.2427 (also using the calibration by Dors et al., 2016), but both show large dispersion.
From the PHANGS-MUSE survey, Kreckel et al. (2019) find pronounced flattened metallicity gradients for three barred spiral galaxies (NGC 1672, NGC 3627 and NGC 4535), especially at $(0.1 - 0.3)\,R_{25}$. The morphology of the three galaxies in this inner region is dominated by strong stellar bars. They do not find a particularly flattened gradient for barred spirals with a lesser pronounced stellar bar however, and they do not draw any firm conclusions. Contrary to the barred galaxies analyzed by Kreckel et al. (2019), in the region $(0.1 - 0.3)\,R_{25}$, the gradient of NGC 925 derived here is steeper ($\nabla_{O/H\,[dex/R_{25}]} = -0.2 \pm 0.2$) than when measuring in the region $(0.0 - 2.08)\,R_{25}$.

Bresolin (2019) estimates, like we do here, metallicity gradients of NGC 6946, among others, using the PG16 calibration. Using a collection of long slit spectra taken throughout the galaxy, they find similar gradients with $\nabla_{O/H\,[dex/kpc]} = -0.033 \pm 0.010$ and $\nabla_{O/H\,[dex/R_e]} = -0.213 \pm 0.063$ to what we do here, that is $\nabla_{O/H\,[dex/kpc]} = -0.02 \pm 0.003$ and $\nabla_{O/H\,[dex/R_e]} = -0.11 \pm 0.01$.
Table 2.8 show total metallicities derived in this work together with values listed in table 1 of Walter et al. (2008). Additionally, table 2.9 show metallicity gradients of NGC 6946 measured by Cedrés et al. (2012) and Moustakas et al. (2010) in the region $0.0 \leqslant R/R_{25} \leqslant 1.0$ using two calibrations; a $R_{23} - O/H$ parametrization by Kobulnicky and Kewley (2004) (hereafter KK04) based on photoionization models of Kewley and Dopita (2002), and the P calibration by Pilyugin and Thuan (2005) (hereafter PT05) based on $R = [O\,III]\,\lambda 4363/H\beta$, and R_2, R_3 and P from equation (2.25). The slope of the metallicity gradients derived in Cedrés et al. (2012) and Moustakas et al. (2010), together with gradients of this work derived in the region

$0.0 \leqslant R/R_{25} \leqslant 1.0$, are given in table 2.9. The (global) average metallicity of this work listed in table 2.9 is defined as the unweighted average, with the uncertainty being the standard deviation. Table 2.9 additionally includes results from Moustakas et al. (2010) on NGC 925, NGC 5194 and NGC 7331.

While the values of the derived gradients are not directly comparable, due to the different metallicity calibrations used, both Cedrés et al. (2012) and Moustakas et al. (2010) find negative gradients of NGC 6946, and the value derived by Moustakas et al. (2010) using PT05 (-0.17 ± 0.15) is very similar to the one derived here using PG16 (-0.17 ± 0.02). Pilyugin and Thuan (2005) found metallicity gradients of NGC 5194 with $\nabla_{\mathrm{O/H}\,[\mathrm{dex}/R_{25}]} = (-0.27 \pm 0.15)$ and $\nabla_{\mathrm{O/H}\,[\mathrm{dex}/R_{25}]} = (-0.13 \pm 0.08)$ using the ff method and P method, respectively. These fits were performed in the region $(0.0 - 1.1)\,R_{25}$, while our observations allow at most $0.87\,R_{25}$. Using the PG16 calibration, our results yielded a gradient of $\nabla_{\mathrm{O/H}\,[\mathrm{dex}/R_{25}]} = (-0.04 \pm 0.0.02)$, which is the most shallow metallicity gradient out of the spirals in our sample (see table 2.7). NGC 5194 is an interacting galaxy, and several previous studies have found that interacting and merging galaxies have significantly flatter metallicity gradients (e.g. Kewley et al., 2010; Rich et al., 2012; Sánchez et al., 2014a). As mentioned by Sánchez et al. (2014a), this relation indicates that the dynamical processes involved in galaxy-galaxy interactions can effectively mix metals on large scales. In the case of NGC 7331, the fit from this work resulted in a gradient with slopes $\nabla_{\mathrm{O/H}\,[\mathrm{dex}/R_{25}]} = (-0.07 \pm 0.02)$ (at $(0.0 - 1.64)\,R_{25}$) and $(-0.05 \pm 0.0.03)$ (at $(0.0 - 1.0)\,R_{25}$). Our derived metallicities generally show low scatter, with NGC 5194, NGC 6946 and NGC 7331 having RMSE $\sim 0.02 - 0.04$, which is an indication of efficient mixing (Kreckel et al., 2019).

$12 + \log(\mathrm{O/H})$	NGC 925	NGC 1569	NGC 4214	NGC 5194	NGC 6946	NGC 7331
This work	8.28 ± 0.08	8.16 ± 0.1	8.2 ± 0.07	8.59 ± 0.03	8.55 ± 0.05	8.56 ± 0.05
Walter et al. (2008)	8.24	8.16	8.34	8.54	8.40	8.36

Table 2.8: Total metallicity of observed galaxies. The first row are total metallicities $\pm 1\sigma$ from this work, while the second row is values from Walter et al. (2008). The metallicities of NGC 925, NGC 5194, NGC 6946 and NGC 7331 from Walter et al. (2008) are derived by Moustakas (2006), and the ones of NGC 1569 and NGC 4214 by Skillman et al. (1989).

	This work [PG16]	C12 [PT05]	C12 [KK04]	M10 [PT05]	M10 [KK04]
NGC 925					
$(O/H)_\mu$	8.26 ± 0.08	–	–	8.22 ± 0.14	8.73 ± 0.15
$\nabla_{O/H}$	-0.14 ± 0.02	–	–	-0.21 ± 0.03	-0.42 ± 0.02
NGC 5194					
$(O/H)_\mu$	8.6 ± 0.03	–	–	8.54 ± 0.09	9.17 ± 0.11
$\nabla_{O/H}$	-0.04 ± 0.02	–	–	-0.31 ± 0.06	-0.50 ± 0.05
NGC 6946					
$(O/H)_\mu$	8.53 ± 0.05	–	–	8.37 ± 0.06	8.99 ± 0.118
$\nabla_{O/H}$	-0.17 ± 0.02	-0.40 ± 0.1	-0.29 ± 0.1	-0.17 ± 0.15	-0.28 ± 0.1
NGC 7331					
$(O/H)_\mu$	8.54 ± 0.05	–	–	8.36 ± 0.07	9.05 ± 0.05
$\nabla_{O/H}$	-0.05 ± 0.03	–	–	-0.24 ± 0.35	-0.56 ± 0.28

Table 2.9: Globally-averaged metallicity $(O/H)_\mu$ and slope of metallicity gradient $\nabla_{O/H}$, in units of [dex/R_{25}] for NGC NGC 925, 5194, NGC 6946 and NGC 7331. The columns are as follows: The first column (This work [PG16]) show values derived in this work; The second (C12 [PT05]) and third (C12 [KK04]) columns are values derived by Cedrés et al. (2012); The fourth (M10 [PT05]) and fifth (M10 [KK04]) columns are values derived by Moustakas et al. (2010). The square brackets refer to the calibration used, with PG16 being the S calibration of Pilyugin and Grebel (2016), PT05 the P calibration by Pilyugin and Thuan (2005), and KK04 a calibration using $R_{23} - O/H$ parametrization by Kobulnicky and Kewley (2004) based on photoionization models of Kewley and Dopita (2002). The gradients from this work listed here are fits to the region $(0.0 - 1.0)\, R_{25}$.

Ionization Gradients

Both NGC 925 and NGC 4214 show positive ionization parameter gradients, while the other galaxies exhibit negative gradients. This decreasing radial profile of ionization parameter for the spiral galaxies agree with results by Kaplan et al. (2016), who examined spirals using IFU. Large dispersions are found in all of the derived ionization gradients (RMSE ~ 0.2), compared to the metallicity gradients (RMSE ~ 0.05). This dispersion is also reported by Poetrodjojo et al. (2018), who found that, compared to the gas-phase metallicity, the ionization parameter exhibits a lack of significant or coherent structure. Contradictory to us, Poetrodjojo et al. (2018) find no significant gradients in ionization parameter.

Zinchenko et al. (2018) calculated metallicities and ionization parameters for a sample of H II regions located in the disks of 59 spiral galaxies at $0.005 < z < 0.03$. Using spectroscopic data from CALIFA DR3, they derived ionization parameters using the same theoretical calibration by Dors et al. (2016) as we do here, and metallicities using the R calibration from Pilyugin and Grebel (2016), where we used the S calibration presented in the same paper. When measuring gradients in the range $0.2 < R/R_{25} < 1.0$, Zinchenko et al. (2018) find that the radial log(U) gradient depend on the metallicity gradient, in the sense that ∇_{U} increases as $\nabla_{\mathrm{O/H}}$ increases. They additionally found that galaxies with flat metallicity gradients also tend to have flat ionization gradients.
While it should be noted that we are using a different calibration for estimating metallicities, we do not find this trend here, even when measuring in the same region ($0.2 < R/R_{25} < 1.0$) and use the same normalization (R/R_{25}). Only four spiral galaxies are included in our sample, which does not allow for interpretation of any trends. In fact, when comparing the results listed in table 1 of Zinchenko et al. (2018) to the metallicity- and ionization parameter gradients derived here (in the region $0.2 < R/R_{25} < 1.0$), an overall agreement is found. When considering ∇_{U} versus $\nabla_{\mathrm{O/H}}$, only NGC 5194 does not fall within the 1σ scatter of 0.1 dex bins in ∇_{U} derived from Zinchenko et al. (2018). However, their range in ∇_{U}, that is -0.488 dex/R_{25} to 0.751 dex/R_{25}, does not go as low as the gradient derived for NGC 5194 ($\nabla_{\mathrm{U\,[dex}/R_{25}]} = -0.58 \pm 0.05$).

In the following, any spaxel i in a radial bin R has *enhanced* oxygen abundance if

$$y_{i \in R} > \mu(\hat{y}_R) + \sigma(\hat{y}_R - y_R) \tag{2.40}$$

where $y_{i \in R}$ is the metallicity of the spaxel i, $\mu(\hat{y}_R)$ is the mean value of the fitted gradient in the radial bin R, and $\sigma(\hat{y}_R - y_R)$ is the standard deviation of the difference between the fitted gradient and the observed metallicities in the radial bin R. The values $\mu(\hat{y}_R) \pm \sigma(\hat{y}_R - y_R)$ correspond to the shaded area in figure 2.8 and 2.9, such that the radial bins have sizes of $0.1R_{\mathrm{e}}$ for NGC 925 and NGC 7331, and $0.05R_{\mathrm{e}}$ for NGC 1569, NGC 4214, NGC 5194 and NGC 6946. Corresponding higher/lower values of log(U) and Hα flux are defined relative to the mean and standard deviation of these parameters in the radial bin R.
Spaxels with enhanced oxygen abundance in NGC 925 and NGC 1569 tend to exhibit higher ionization parameter and/or higher Hα flux, while lower log(U) is also found for some spaxels in NGC 925, although to a lesser extent. Only a smaller fraction of the oxygen enhanced spaxels in NGC 5194, NGC 6946 and NGC 7331 have higher values of log(U). For these three galaxies, a similar enhancement in oxygen abundance is mostly associated with either lower ionization parameter or higher Hα luminosity. An enhancement in oxygen abundance is, to a smaller degree, also associated with a combination of lower values in both log(U) and Hα for NGC 6946, and lower Hα for NGC 5194. Considering the full sample, the vast majority of the oxygen-enhanced spaxels (i.e. outliers) are associated with higher values of log(U) and/or Hα flux. These results mostly agree with those of Kreckel et al. (2019), who examined H II regions across the discs of eight nearby galaxies using VLT/MUSE optical IFS as part

of the PHANGS-MUSE survey. Kreckel et al. (2019) estimated metallicities with the PG16 calibration like we do here, but use the line ratio

$$\frac{[\mathrm{S\,III}]\,\lambda9069 + \lambda9532}{[\mathrm{S\,II}]\,\lambda6716 + \lambda6731}$$

as an indicator of ionization parameter, as a positive linear correlation is expected between log([S III]/[S II]) and log(U), and [S III]/[S II] only has a weak dependence on metallicity. They found regions with enhanced oxygen abundances to be associated with high ionization parameter and higher Hα luminosity. As mentioned in Kreckel et al. (2019), the ionization parameter yield information about the local physical conditions, and higher values of log(U) typically indicates either a stronger ionizing source or a lower ionized gas density. As both Hα emission and the level of ionization are signs of photoionization powered by UV radiation from young, massive stars, the observed trend with oxygen-enhancement being associated with higher log(U) and Hα luminosity may thus be an indication of local enrichment from recent star formation.

2.2 The IllustrisTNG Simulations

The IllustrisTNG simulations are a set of state-of-the-art cosmological, magnetohydrodynamical (hereafter MHD) simulations build to simulate the formation and evolution of galaxies in a cosmological setting. The simulations are build with the moving mesh code Arepo (Springel, 2010a) which solves the coupled ideal MHD and self-gravity equations. This thesis works with two of the primary volumes, IllustrisTNG50-1 and IllustrisTNG100-1, of which the main characteristics are summarised in table 2.10. IllustrisTNG uses the Planck15 cosmology, with matter density $\Omega_\mathrm{m} = \Omega_\mathrm{DM} + \Omega_\mathrm{bary} = 0.3089$, cosmological constant $\Omega_\Lambda = 0.6911$ and Hubble constant $H_0 = 100h$ km/s/Mpc with $h = 0.6774\,\mathrm{km/Mpc/s}$. Both IllustrisTNG50-1 and TNG100-1 contain a total of 100 snapshots labelled 0 though 99, with snapshot 0 corresponding to $z = 127.0$ and snapshot 99 corresponding to $z = 0$ and $t = 13.803$ Gyr.

IllustrisTNG follow the evolution of large scale structures, the clustering of galaxies and the shapes of halos for both dark- and baryonic matter from $z = 127.0$ to $z = 0$. The hydrodynamical interactions of the gaseous component are described by the conservation of mass, momentum and energy; namely the Euler equations of fluid dynamics. Following the notation of Springel (2010b), this set of equations may be written in compact form by introducing a vector $\boldsymbol{U}$ describing the state of the fluid

$$\boldsymbol{U} = \begin{pmatrix} \rho \\ \rho\,\boldsymbol{v} \\ \rho\,\boldsymbol{e} \end{pmatrix} = \begin{pmatrix} \rho \\ \rho\,\boldsymbol{v} \\ \rho\,\boldsymbol{u} + \frac{1}{2}\rho\,\boldsymbol{v}^2 \end{pmatrix} \tag{2.41}$$

where ρ is the mass density, $\boldsymbol{v}$ is the velocity field, and $\boldsymbol{e} = \boldsymbol{u} + \boldsymbol{v}^2/2$ is the total energy per unit mass. The thermal energy per unit mass $\boldsymbol{u}$ is fully determined by temperature for an ideal gas. These fluid parameters are all functions of spatial position and time, and from $\boldsymbol{U}$, the flux function may thus be defined as

$$\boldsymbol{F}(\boldsymbol{U}) = \begin{pmatrix} \rho\,\boldsymbol{v} \\ \rho\,\boldsymbol{v}\,\boldsymbol{v}^\mathrm{T} + P \\ (\rho\,\boldsymbol{e} + P)\,\boldsymbol{v} \end{pmatrix} \tag{2.42}$$

where P is the equation of state defining the pressure of the fluid

$$P = (\gamma - 1)\,\rho\,\boldsymbol{u} \tag{2.43}$$

where γ is the adiabatic index. Using these definitions, the Euler equations can be written as

$$\frac{\partial \boldsymbol{U}}{\partial t} + \nabla \cdot \boldsymbol{F} = 0 \tag{2.44}$$

As described in Springel (2010a) and Pillepich et al. (2017), Arepo solves ideal (magneto-)hydrodynamic conservation laws with a finite-volume approach, using a moving unstructured mesh defined by the Voronoi tessellation of a set of discrete points. Finite-volume methods are widely used in computational fluid dynamics. In this approach, the volume of the system is subdivided into finite cells enclosing discrete points on the mesh. The state of the fluid is then described by the averages of the conserved fluid parameters of the cells.
The Voronoi tessellation subdivides the mesh into N cells, that is, one cell for each discrete point p_i on the mesh. Any point q lies in the cell of a point p_i, provided it obeys

$$\forall j \in \{1, \ldots, N\} \backslash \{i\} : d(p_i, q) < d(p_j, q) \tag{2.45}$$

with $d(p_i, q)$ being the distance from a point q to p_i. The resulting Voronoi cell of any site p_i on the mesh thus consists of all points $q_1, \ldots, q_M$ that are closer to p_i than to $p_{j\neq i}$. The mesh comprised of Voronoi cells therefore continuously deforms as each point moves, adapting the resolution to the local clustering, similar to smoothed particle hydrodynamics (SPH) codes. This automatic and continuous adjustment of spatial resolution is advantageous for simulations like IllustrisTNG that follow structure growth in a cosmological context (Springel, 2010a). In the setting of IllustrisTNG, the Voronoi cells track the conserved fluid parameters: mass, momentum, energy, and cell averaged magnetic field (Pillepich et al., 2017).

IllustrisTNG includes prescriptions for large variety of physical processes driving galaxy formation and -evolution, which is described below following section 1 and 2 of Pillepich et al. (2017). The simulated galaxies (hereafter subhalos) are defined at each snapshot (i.e. time step) by the SUBFIND algorithm (see Springel et al., 2001), where particles (of any kind) are associated with a unique subhalo (defined by its *SubhaloID*) if the particle is gravitationally bound to the object.

As star formation processes are unresolved in the cosmological simulations, IllustrisTNG adopt a prescription following empirically motivated models, where stars form stochastically from gas with $n_{\rm H} \gtrsim 0.1{\rm cm}^{-3}$ following the observed Kennicutt-Schmidt relation

$$\Sigma_{\rm SFR} = A(\Sigma_{\rm gas})^p, \quad p \sim 2 \tag{2.46}$$

where $\Sigma_{\rm SFR}$ and $\Sigma_{\rm gas}$ is the SFR- and gas surface densities, respectively, and a Chabrier initial mass function (hereafter IMF). The IMF for $M \leqslant 1M_\odot$ is given in Chabrier (2003):

$$\xi(\log(M)) = A \times \exp\left[-\frac{(\log(M) - \log(M_C))^2}{2\sigma^2}\right] \tag{2.47}$$

A is a normalization coefficient and is given in units of $\log(M_\odot)^{-1}\,{\rm pc}^{-3}$. For single objects, $A = 0.158$, $M_C = 0.079$ and $\sigma = 0.69$, and for stellar systems, e.g. binaries, $A = 0.086$, $M_C = 0.22$ and $\sigma = 0.57$. For $M > 1M_\odot$, the IMF of Chabrier (2003) is

$$\xi(\log(M)) = A \times M^{-x} \tag{2.48}$$

with $A = 0.0443$ and $x = 1.3$ for single objects. As described in Pillepich et al. (2017), the presence of magnetic fields in star-forming gas is treated in a somewhat simple manner, and can have the following outcomes:

(i) The gas is converted into a star

(ii) The gas is converted into wind

(iii) A fraction of the gas is converted into a star

(iv) A fraction of the gas is converted into wind

The newly formed stellar particles each correspond to one or more stellar populations which subsequently evolve and age. The mass and metal injection into the surrounding ISM over time is tracked through three evolutionary stages, namely AGB stars, SNe II and -Ia. IllustrisTNG assumes that stars with masses $1M_\odot - 8M_\odot$ go through the AGB phase, and stars with masses $8M_\odot - 100M_\odot$ become SNe II. The choices of elemental mass yields from AGB stars, SNe II and -Ia are given in table 2 of Pillepich et al. (2017).
Stellar- and SNe feedback is accounted for in the form of outflows on galactic scales, launched directly from the ambient gas through wind-phase particles. The kinetic winds are isotropically injected with a speed that is scaled to the local 1D velocity dispersion of dark matter, and

naturally follow the path of least resistance, producing galactic-scale patterns. The wind particles, with properties inherited from the originating gas cell, feed mass, momentum, metals, and thermal- and kinetic energy into the ISM as they leave the local region. The ISM is thereby chemically enriched by SNe Ia, SNe II and AGB stars, where a total of nine elements (H, He, C, N, O, Ne, Mg, Si and Fe) are tracked, in addition to the total of all untracked metals.

IllustrisTNG also includes prescriptions for black hole formation and growth, with black hole formation being subject to resolution issues similar to that of star formation processes. Super massive black holes are also accounted for, and black hole mergers occur when the distance between two black holes is small enough that one is situated in the accretion/feedback region of the other. The simulations also model kinetic feedback from AGN driven winds, even at low accretion rates. At high accretion rates, gas surrounding the black hole is heated by thermal AGN feedback. The prescription for AGN feedback additionally causes quenching of star formation in subhalos of $\sim 10^{12} - 10^{14} M_{\odot}$ halos (Pillepich et al., 2017).

IllustrisTNG has generally shown to predict reasonable galaxy populations consistent with present-day observations, with one example being the MMR (e.g. Torrey et al., 2019). This is illustrated in figure 2.10, which show the MMR of IllustrisTNG subhalos, together with the sample of observed galaxies from this work, plotted on top of a 2D histogram with values of SDSS galaxies.

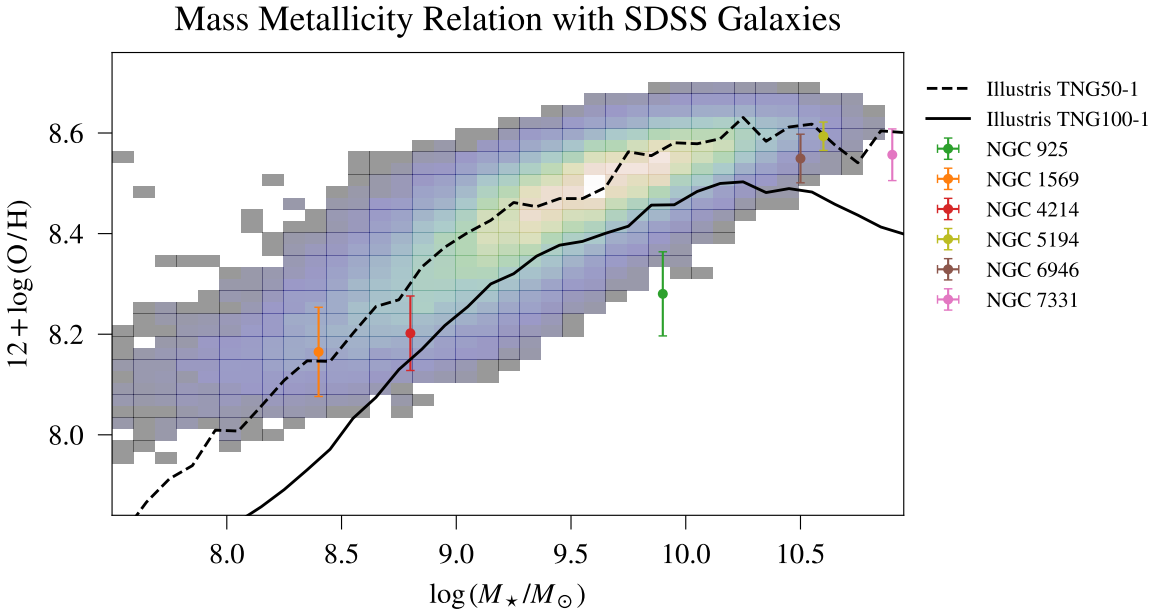

Figure 2.10: Mass metallicity relation of subhalos from IllustrisTNG50-1 (dashed black line, mean) and TNG100-1 (solid black line, mean), SDSS galaxies at $z \sim 0$ (2D histogram), and the sample of observed galaxies from this work (error bars).

Row	Parameter	IllustrisTNG50-1	IllustrisTNG100-1
0	$V_{\rm box}$	$51.7^3\,{\rm Mpc}^3$	$110.7^3\,{\rm Mpc}^3$
1	$L_{\rm box}$	$35\,{\rm Mpc}/h$	$75\,{\rm Mpc}/h$
2	$N_{\rm DM}$	2160^3	1820^3
3	$N_{\rm gas}$	2160^3	1820^3
4	$N_{\rm tracers}$	2160^3	2×1820^3
5	$m_{\rm baryon}$	$8.5 \times 10^5 M_\odot$	$1.4 \times 10^6 M_\odot$
6	$m_{\rm DM}$	$4.5 \times 10^5 M_\odot$	$7.5 \times 10^6 M_\odot$
7	FoF Groups	991,282,388	609,688,208
8	Subfind Groups	654,909,401	469,094,112
9	Subfind Subhalos at $z = 0$	5,688,113	4,371,211
10	Particles	1,995,432,581,886	1,193,030,999,901
11	Δs at $z = 0$	0.074 kpc	0.185 kpc

Table 2.10: Main characteristics of IllustrisTNG50-1 and IllustrisTNG100-1. The parameters are as follows: Row 0, $V_{\rm box}$: Box volume; Row 1, $L_{\rm box}$: Box side length; Row 2, $N_{\rm DM}$: Number of dark matter particles; Row 3, $N_{\rm gas}$: Number of gas particles; Row 4, $N_{\rm tracers}$: Number of tracer particles; Row 5, $m_{\rm baryon}$: Baryonic mass; Row 6, $m_{\rm DM}$: Dark matter mass; Row 7: Number of Friends-of-Fields (FoF) groups; Row 8: Number of Subfind Groups; Row 9: Number of Subfind subhalos at $z = 0$; Row 10: Number of particles; Row 11, Δs: Spatial resolution at $z = 0$.

2.2.1 Selection of Simulated Subhalo Candidates

Simulated galaxies were selected such that they are matched in stellar mass, gas mass and SFR. Galaxy candidates were selected from IllustrisTNG-50 for NGC 1569 and NGC 4214, IllustrisTNG-100 for NGC 5194 and NGC 6946, and from both IllustrisTNG-50 and TNG-100 for NGC 925 and NGC 7331. Values of stellar mass, gas mass, SFR and sSFR for the observed galaxies, means, standard deviations and sample sizes of the final sample of simulated galaxies are summarised in table 2.11. Histograms of stellar- and gas mass and SFR of the selected simulated galaxy candidates for each observed galaxy can be seen in figures 2.11, 2.12 and 2.13, respectively. As can be seen in figure 2.12, the gas mass distribution for the selected subhalos of NGC 5194 and NGC 6946 are very asymmetric. This is due to the fact that the sample of simulated galaxies, for any observed galaxy, were chosen based more heavily on similarity in stellar mass than in gas mass, while keeping a reasonable agreement with the SFR.

NGC 1569	$\log(M_\star/M_\odot)$	$\log(M_{\rm gas}/M_\odot)$	log(SFR)	log(sSFR)	Sample Size
Observed value	8.4	7.9	-1.222	-9.622	–
IllustrisTNG-50	8.41 ± 0.08	8.0 ± 0.1	-1.4 ± 1.5	-10.0 ± 0.4	17
NGC 4214	$\log(M_\star/M_\odot)$	$\log(M_{\rm gas}/M_\odot)$	log(SFR)	log(sSFR)	Sample Size
Observed value	8.8	8.7	-0.971	-9.771	–
IllustrisTNG-50	8.83 ± 0.08	8.7 ± 0.1	-1.1 ± 1.1	-10.0 ± 0.4	22
NGC 5194	$\log(M_\star/M_\odot)$	$\log(M_{\rm gas}/M_\odot)$	log(SFR)	log(sSFR)	Sample Size
Observed value	10.6	9.5	0.495	-10.105	–
IllustrisTNG-100	10.57 ± 0.07	9.7 ± 0.1	0.33 ± 0.05	-10.3 ± 0.2	14
NGC 6946	$\log(M_\star/M_\odot)$	$\log(M_{\rm gas}/M_\odot)$	log(SFR)	log(sSFR)	Sample Size
Observed value	10.5	9.8	0.51	-9.99	–
IllustrisTNG-100	10.47 ± 0.08	10.0 ± 0.1	0.5 ± 0.6	-9.97 ± 0.1	12
NGC 7331	$\log(M_\star/M_\odot)$	$\log(M_{\rm gas}/M_\odot)$	log(SFR)	log(sSFR)	Sample Size
Observed value	10.9	10.1	0.475	-10.425	–
IllustrisTNG-50	10.92 ± 0.07	10.3 ± 0.2	0.6 ± 0.3	-10.4 ± 0.2	10
IllustrisTNG-100	10.86 ± 0.06	10.3 ± 0.2	0.44 ± 0.03	-10.4 ± 0.2	5
Full Sample	11.00 ± 0.07	10.3 ± 0.2	0.5 ± 0.2	-10.4 ± 0.2	15
NGC 925	$\log(M_\star/M_\odot)$	$\log(M_{\rm gas}/M_\odot)$	log(SFR)	log(sSFR)	Sample Size
Observed value	9.9	9.8	-0.251	-10.151	–
IllustrisTNG-50	9.86 ± 0.07	10.0 ± 0.1	-0.3 ± 1.0	-10.1 ± 0.1	23
IllustrisTNG-100	9.9 ± 0.06	9.81 ± 0.06	-0.3 ± 1.0	-10.18 ± 0.09	30
Full Sample	9.88 ± 0.07	9.8 ± 0.1	-0.3 ± 0.9	-10.2 ± 0.1	53

Table 2.11: Overview of characteristics of the final selection of IllustrisTNG subhalos, together with the values of the observed galaxy for which the selection was based upon. The values listed under the IllustrisTNG simulations are $\mu \pm \sigma$ of the subhalo sample.

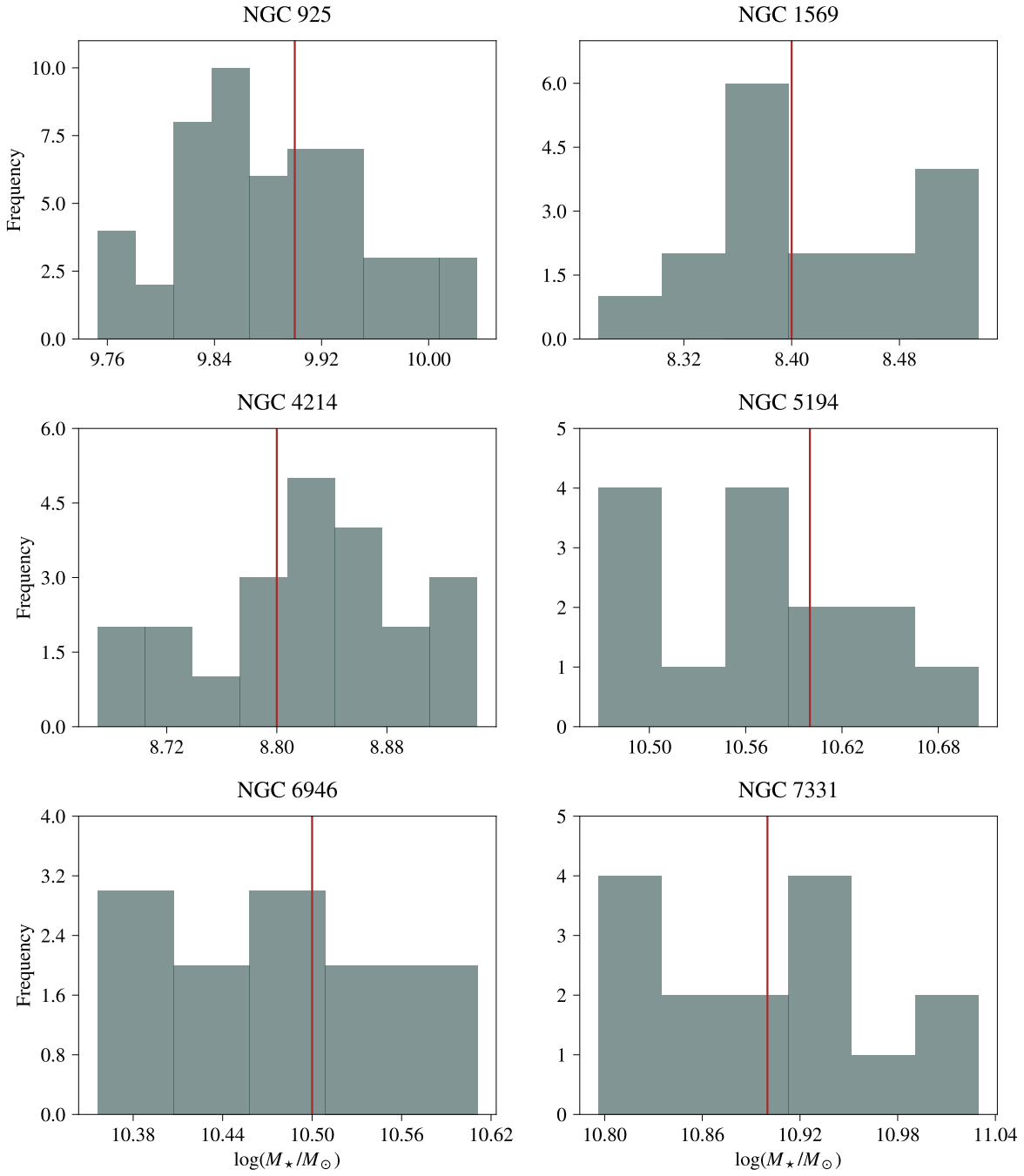

Figure 2.11: Histograms of stellar mass for the final sample of subhalos. The vertical red line is the stellar mass of the respective observed galaxy.

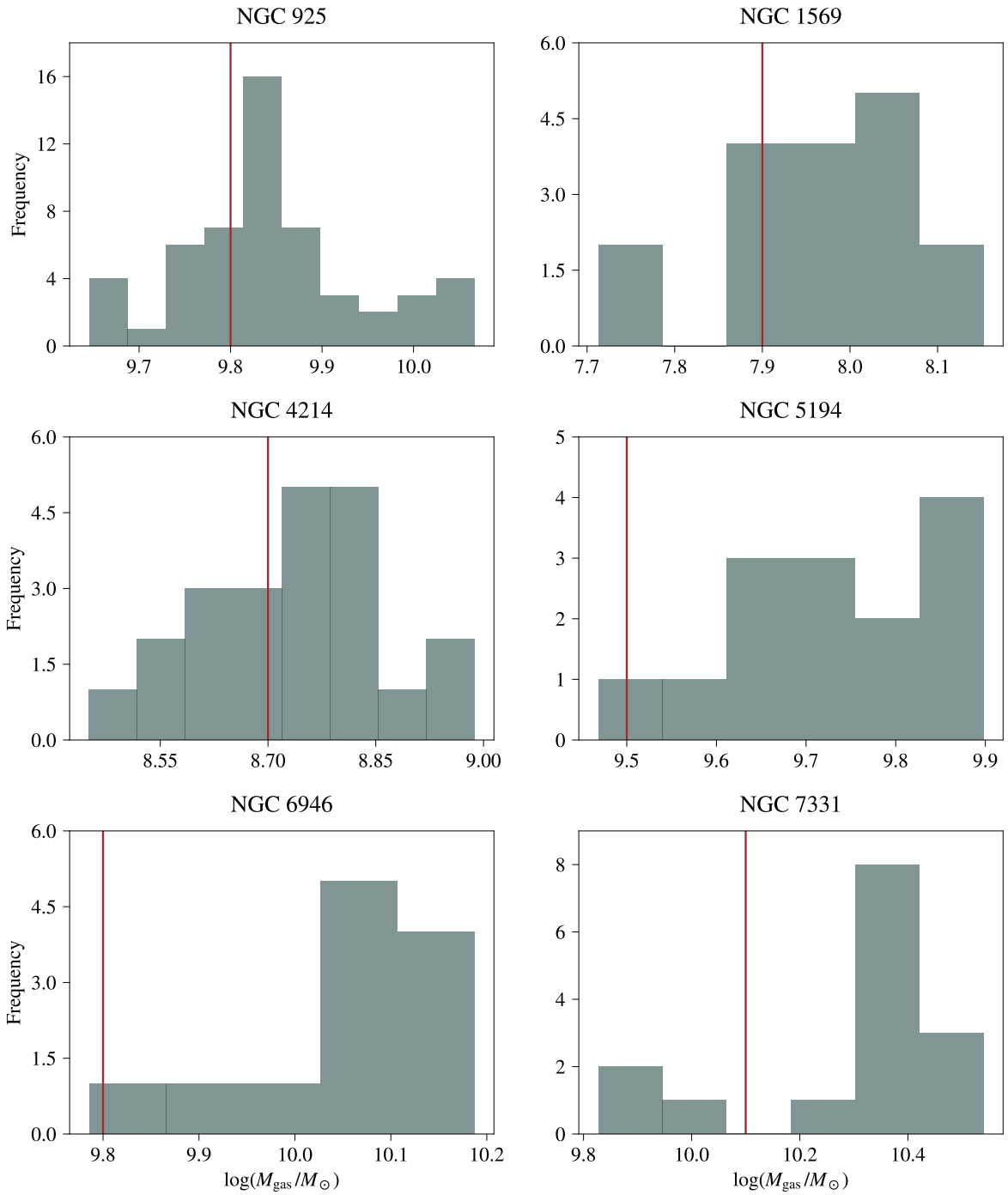

Figure 2.12: Histograms of gas mass for the final sample of subhalos. The vertical red line is the gas mass of the respective observed galaxy.

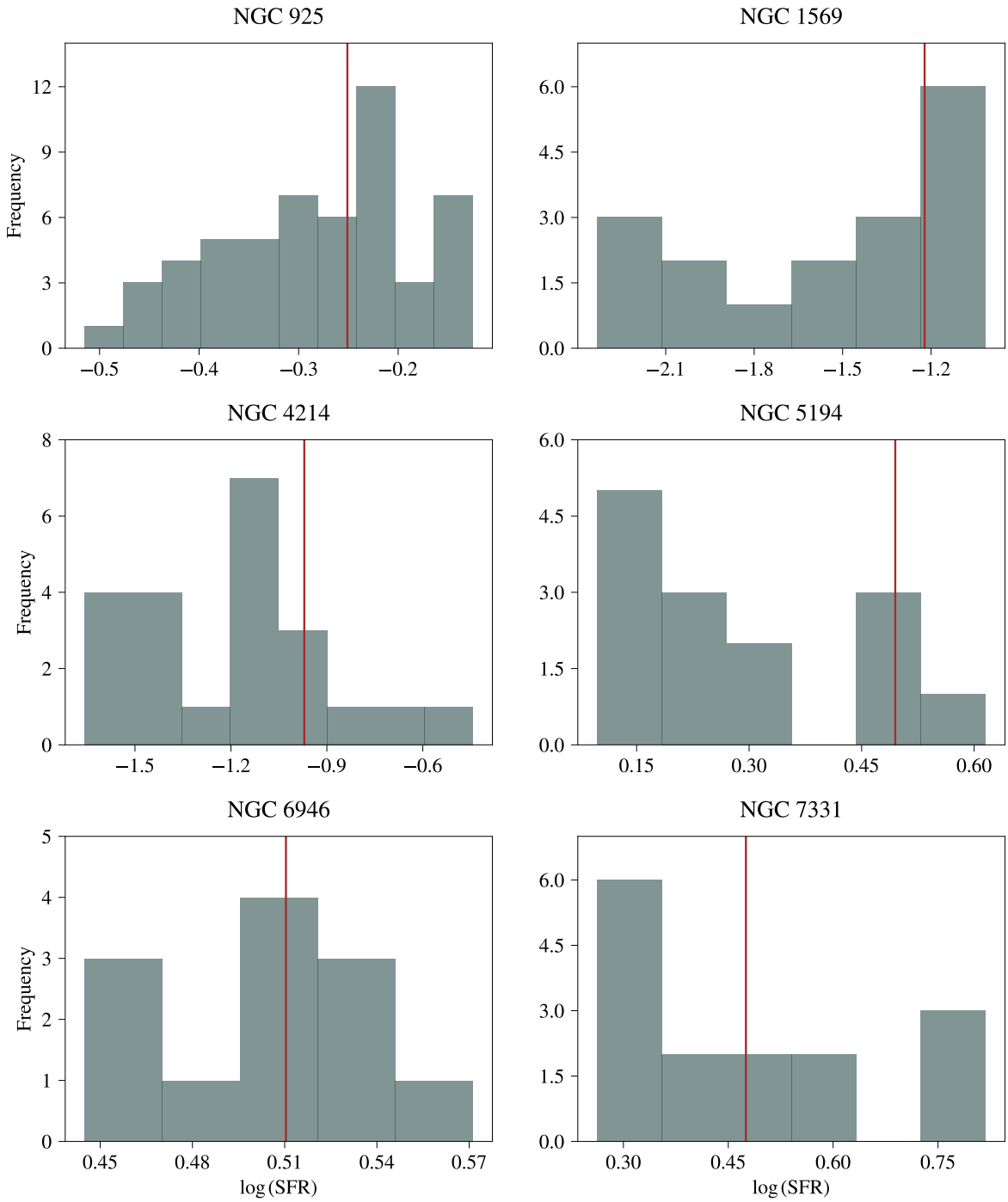

Figure 2.13: Histograms of log(SFR) for the final sample of subhalos. The vertical red line is log(SFR) of the respective observed galaxy.

2.2.2 Principal Axis Transformation

To analyze the gradients of the simulated galaxies from IllustrisTNG, the system must first be rotated face-on in order to measure radial gradients along the disc. The rotation is done by a principal axis transformation, using eigenvectors derived from the gas particles of a subhalo. In the following, the central coordinates and velocities of the subhalo is denoted x_0, y_0, z_0 and $v_{x,0}$, $v_{y,0}$, $v_{z,0}$, respectively. A virial radius of $r_{\mathrm{vir}} = 5\,[\mathrm{kpc}]$ is chosen, and inner gas particles are therefore defined as having $\boldsymbol{r}_\diamond \leqslant r_{\mathrm{vir}}$, with

$$\boldsymbol{r}_\diamond = \sqrt{(\boldsymbol{x}_\diamond - x_0)^2 + (\boldsymbol{y}_\diamond - y_0)^2 + (\boldsymbol{z}_\diamond - z_0)^2}$$

The first step in the coordinate transformation consists of deriving the eigenvectors. Defining an inertia vector with dimension 6:

$$\boldsymbol{M} = \begin{bmatrix} M_0 & M_1 & M_2 & M_3 & M_4 & M_5 \end{bmatrix}^{\mathrm{T}} \tag{2.49}$$

where:

$$\begin{aligned}
M_0 &= \sum_{i \in \text{inner}} (\boldsymbol{m}_{\diamond,i} \cdot \boldsymbol{x}^2_{\diamond,i}) \\
M_1 &= \sum_{i \in \text{inner}} (\boldsymbol{m}_{\diamond,i} \cdot \boldsymbol{y}^2_{\diamond,i}) \\
M_2 &= \sum_{i \in \text{inner}} (\boldsymbol{m}_{\diamond,i} \cdot \boldsymbol{z}^2_{\diamond,i}) \\
M_3 &= \sum_{i \in \text{inner}} (\boldsymbol{m}_{\diamond,i} \cdot \boldsymbol{y}_{\diamond,i} \cdot \boldsymbol{x}_{\diamond,i}) \\
M_4 &= \sum_{i \in \text{inner}} (\boldsymbol{m}_{\diamond,i} \cdot \boldsymbol{z}_{\diamond,i} \cdot \boldsymbol{x}_{\diamond,i}) \\
M_5 &= \sum_{i \in \text{inner}} (\boldsymbol{m}_{\diamond,i} \cdot \boldsymbol{z}_{\diamond,i} \cdot \boldsymbol{y}_{\diamond,i})
\end{aligned}$$

a 3×3 symmetric matrix A, consisting of the components of the inertia vector $\boldsymbol{M}$, can be defined:

$$A = \begin{bmatrix} M_0 & M_3 & M_4 \\ M_3 & M_1 & M_5 \\ M_4 & M_5 & M_2 \end{bmatrix} \tag{2.50}$$

From the spectral theorem, A is diagonalizable, the eigenspaces of A are mutually orthogonal and the eigenvalues of A are real. Thus, by diagonalizing A:

$$\det \left| A - \lambda I \right| = 0 \tag{2.51}$$

with I being an identity matrix, we obtain the eigenvalues λ_0, λ_1 and λ_2 with corresponding eigenvectors $\boldsymbol{u}_0$, $\boldsymbol{u}_1$ and $\boldsymbol{u}_2$.
Defining an index sorting vector, based on the eigenvalues:

$$\boldsymbol{b}_\lambda = \begin{bmatrix} b_{\lambda,0} \\ b_{\lambda,1} \\ b_{\lambda,2} \end{bmatrix} \tag{2.52}$$

the resulting eigenvectors for the x, y and z components (in this order) are found as:

$$\boldsymbol{e}_0 = \boldsymbol{u}[:, b_{\lambda,2}] \,/\, \sqrt{\left|\sum \boldsymbol{u}[:, b_{\lambda,2}]^2\right|} \tag{2.53}$$

$$\boldsymbol{e}_1 = \boldsymbol{u}[:, b_{\lambda,1}] \,/\, \sqrt{\left|\sum \boldsymbol{u}[:, b_{\lambda,1}]^2\right|} \tag{2.54}$$

$$\boldsymbol{e}_2 = \boldsymbol{u}[:, b_{\lambda,0}] \,/\, \sqrt{\left|\sum \boldsymbol{u}[:, b_{\lambda,0}]^2\right|} \tag{2.55}$$

The transformed coordinates $\boldsymbol{x'}$, $\boldsymbol{y'}$, $\boldsymbol{z'}$ and velocities $\boldsymbol{v'_x}$, $\boldsymbol{v'_y}$, $\boldsymbol{v'_z}$ (of any particle type) are then calculated by multiplying the position- and velocity vectors by the eigenvectors of each directional component:

$$\begin{aligned}
\boldsymbol{x'} &= (\boldsymbol{x} - x_0) \cdot e_{0,0} + (\boldsymbol{y} - y_0) \cdot e_{0,1} + (\boldsymbol{z} - z_0) \cdot e_{0,2} \\
\boldsymbol{y'} &= (\boldsymbol{x} - x_0) \cdot e_{1,0} + (\boldsymbol{y} - y_0) \cdot e_{1,1} + (\boldsymbol{z} - z_0) \cdot e_{1,2} \\
\boldsymbol{z'} &= (\boldsymbol{x} - x_0) \cdot e_{2,0} + (\boldsymbol{y} - y_0) \cdot e_{2,1} + (\boldsymbol{z} - z_0) \cdot e_{2,2} \\
\boldsymbol{v'_x} &= (\boldsymbol{v_x} - v_{x,0}) \cdot e_{0,0} + (\boldsymbol{v_y} - v_{y,0}) \cdot e_{0,1} + (\boldsymbol{v_z} - v_{z,0}) \cdot e_{0,2} \\
\boldsymbol{v'_y} &= (\boldsymbol{v_x} - v_{x,0}) \cdot e_{1,0} + (\boldsymbol{v_y} - v_{y,0}) \cdot e_{1,1} + (\boldsymbol{v_z} - v_{z,0}) \cdot e_{1,2} \\
\boldsymbol{v'_z} &= (\boldsymbol{v_x} - v_{x,0}) \cdot e_{2,0} + (\boldsymbol{v_y} - v_{y,0}) \cdot e_{2,1} + (\boldsymbol{v_z} - v_{z,0}) \cdot e_{2,2}
\end{aligned}$$

where the notation $e_{i,j}$ indicates the directional component i and the index j into $\boldsymbol{e}_i$.

2.2.3 Particle Selection Criteria, Calculations and Definitions for Extraction of Physical Quantities from Intrinsic Simulation Data

In the following, the notation of any parameter p_* will be:

$$\begin{aligned}
p_\star &\longrightarrow \text{Star particles} \\
p_\diamond &\longrightarrow \text{Gas particles} \\
p_\bullet &\longrightarrow \text{Black hole particles}
\end{aligned}$$

Specifically, regarding radii and masses, lower case notation r_* and m_* denotes radii and masses of individual particles, while upper case notation R_* and M_* denotes the radius and total mass of the subhalo. Central coordinates and velocities of each subhalo are denoted by x_0, y_0, z_0 and $v_{x,0}$, $v_{y,0}$, $v_{z,0}$, respectively, while for individual particles, the notation is x_*, y_*, z_* and $v_{x,*}$, $v_{y,*}$, $v_{z,*}$. Where relevant, bold notation is used for denoting vectors.

Only particles within the subhalo radius $R_{\rm Sub}$ are considered. See table 2.12 for an overview of notation, units, and field names used in the derivation of subhalo- and particle parameters from the IllustrisTNG simulations. Table A.1 in appendix A list the adopted notations and values of constants and conversion factors. Except otherwise noted, the Boltzmann constant is in CGS units in all calculations. The adopted Solar metallicity is $Z_\odot = 0.0127$.
The paragraphs below describe calculations of some selected parameters given in table 2.12, as well as definitions used in the selection criteria of star-, gas-, and black hole particles. The parameters derived from IllustrisTNG, and elaborated on here, are used in the modelling of emission arising from different sources, used to generate synthetic emission lines as described in 2.2.4.

Stellar parameters
The scale factor at the time of formation of a particle $a_\star$ is used to distinguish stars from wind phase gas cells, with stars having $a\star > 0$. This value is converted to stellar age in Gyr by first converting to redshift using $a = 1/(1+z)$, and then applying the function `lookback_time`, assuming a Planck15 cosmology, which is included in the sub-package COSMOLOGY of the

Python module Astropy (Price-Whelan et al., 2018). The Planck15 cosmology of the Astropy.Cosmology sub-package is a flat ΛCDM cosmology, with (at $z = 0$) Hubble constant $H_0 = 67.7\,\mathrm{km/Mpc/s}$, density of non-relativistic and baryonic matter $\Omega_{m,0} = 0.307$ and $\Omega_{b,0} = 0.0486$, respectively, both given in units of the the critical density at $z = 0$, Ω_{C} (2016, table 4). Post-AGB (hereafter PAGB) stars are then defined to have an age (i.e., time since formation) of $t_\star \geqslant 1$ Gyr.

Black hole parameters

The black hole accretion rate $\dot{M}_\bullet$ is considered for black hole particles situated at $r_\bullet \leqslant 1$ kpc.

Gas parameters

The mean molecular weight is defined by

$$\mu = \frac{4}{1 + 3 \cdot \mathcal{X}_{\mathrm{H}} + 4 \cdot \mathcal{X}_{\mathrm{H}} \cdot x_{e,\diamond}} \cdot m_{\mathrm{H}} \times 10^3 \tag{2.56}$$

with $\mathcal{X}_{\mathrm{H}} = 0.76$ being the Hydrogen mass fraction. The gas temperature is found according to *FAQ, Illustris TNG*:

$$T_\diamond = (\gamma - 1)\,\frac{\mu\, u_\diamond}{k_{\mathrm{B}}} \times 10^{10} \tag{2.57}$$

and the particle number density is calculated as:

$$\rho_\diamond = \frac{\rho_{0,\diamond}\, h^2}{m_{\mathrm{H}}\, a^3\, c_{\mathrm{d}}^3} \times 10^{10}\, M_\odot \tag{2.58}$$

Chemical abundances of interest, besides the intrinsic metallicity $Z_\diamond$, are the oxygen abundance and the carbon-to-oxygen abundance ratio:

$$12 + \log(\mathrm{O/H})_\diamond = 12 + \log\left(\frac{\mathrm{O}_{0,\diamond}/15.999}{\mathrm{H}_{0,\diamond}/1.00784}\right) \tag{2.59}$$

$$\log(\mathrm{C/O})_\diamond = \log\left(\frac{\mathrm{C}_{0,\diamond}/12.0107}{\mathrm{O}_{0,\diamond}/15.999}\right) \tag{2.60}$$

'GFM_Metals' yield mass-weighted abundances (see table 2.12), so when deriving chemical abundances using this field, the values are first divided by the atomic weight of the respective element. The average magnetic field strength $B_\diamond$ is just the magnitude of the magnetic field strength vector $\boldsymbol{B}_\diamond$:

$$B_\diamond = \sqrt{B_{0,\diamond}^2 + B_{1,\diamond}^2 + B_{2,\diamond}^2} \tag{2.61}$$

We define warm (or SF) gas particles following the density- and temperature criteria by Torrey et al. (2019)

$$\begin{aligned} \log(T/\,10^6\,\mathrm{K}) &\leqslant 0.25\, \log(\rho/405\,\mathrm{cm}^{-3}\,) \\ \rho &\geqslant 0.13\,\mathrm{cm}^{-3} \end{aligned} \tag{2.62}$$

while shock gas particles are defined by

$$\begin{aligned} \mathcal{M} &> 0 \\ \mathrm{SFR} &= 0 \end{aligned} \tag{2.63}$$

and AGN gas particles are selected to obey (2.63) and are situated at a radius $r_\diamond \leqslant 1$ kpc.

Creating Data Cubes

After performing the coordinate transformation (section 2.2.2) and deriving particle parameters (section 2.2.3), each subhalo is binned into (1 kpc × 1 kpc × 1 kpc) cubes. This is done by iterative looping over the spatial positions, such that the resulting cubes have well defined central coordinates. Each cube may contain several of the particle types (stars, gas and black holes). The parameter value of each cube is calculated as described in the following. Cube values are distinguished from unbinned cell values, p, by $\tilde{p}$.

PAGB star parameters
The age of stars in a cube is calculated as the mean of $t_\star$, the stellar mass as the sum of $m_\star$, and the stellar metallicity as the mean of $\log(Z_\star/Z_\odot)$, each for all enclosed star particles with $t_\star \geqslant 1$ Gyr.

Warm/SF gas parameters
Each value described here is computed for all enclosed gas particles obeying (2.62). The density and temperature of warm gas in a cube is calculated as the means of $\rho_\diamond$ and $T_\diamond$, respectively. The metallicity, oxygen abundance and carbon-to-oxygen abundance ratio are calculated as the mean of $\log(Z_\diamond/Z_\odot)$, $12 + \log(\mathrm{O/H})_\diamond$ and $\log(\mathrm{C/O})_\diamond$, respectively. The star formation rate ($\tilde{\mathrm{SFR}}_\diamond$), hydrogen- ($\tilde{\mathrm{H}}_\diamond$) and oxygen ($\tilde{\mathrm{O}}_\diamond$) chemical abundances as the sum of $\mathrm{SFR}_\diamond$, $\mathrm{H}_\diamond$ and $\mathrm{O}_\diamond$, respectively, where $\mathrm{O}_\diamond$ and $\mathrm{H}_\diamond$ are the values taken from 'GFM_Metals' and divided by the atomic weight. The uncertainty on $\mathrm{O}_\diamond$ and $\mathrm{H}_\diamond$, that is $\tilde{\sigma}_{\mathrm{O},\diamond}$ and $\tilde{\sigma}_{\mathrm{H},\diamond}$, are the standard deviations of $\mathrm{O}_\diamond$ and $\mathrm{H}_\diamond$.
Figure 2.14 shows density-temperature phase diagrams of subhalos of masses 9.5, 10.0, 10.5, 11.0 and 11.5. The dashed lines indicate the temperature-density cut given in equation (2.62), such that the lower right region is representing warm/SF gas. As previously discussed, an instantaneous SFR is attributed to each gas particle, in order to estimate the expected amount of gas that is converted into a star

$$\mathrm{SFR} = \frac{\epsilon_{\mathrm{SF}} \cdot m_{\mathrm{gas}}}{t_{\mathrm{ff}}} \tag{2.64}$$

where the star formation efficiency ϵ_{SF} ensures that sub-resolution turbulent motions that may affect the star formation is accounted for. The line seen in figure 2.14 is completely synthetic; in reality, higher density gas if colder. This is an implication of cosmological simulations not having the resolution needed to capture the multi-phase ISM. In particular, cosmological simulations are not able to resolve the cold denser gas phases, why an artificially pressurised gas phase (dense, but not cold) is introduced. It is also seen in figure 2.14 that the denser/colder gas have higher metallicities. The higher level of enrichment in these gas-phases stem from the metals being released into the surroundings of star-forming regions where SNe II explosions occur. In comparison, the gas-phase with low density and high temperature (the halo gas) is much more metal-poor, except for the most massive galaxies with $\log(M_\star/M_\odot) \approx 10.5$ (lower panel of figure 2.14), where metals are ejected into the circum-galactic medium through AGN feedback.

AGN gas parameters
The density, metallicity and carbon-to-oxygen abundance ratio are calculated as the mean of $\rho_\diamond$, $\log(Z_\diamond/Z_\odot)$ and $\log(\mathrm{C/O})_\diamond$, respectively, each for all enclosed gas particles obeying 2.63 and situated at $r_\diamond \leqslant 1$ kpc.

AGN black hole parameters
The black hole accretion rate is calculated as the sum of $\dot{M}_\bullet$ of all black hole particles situated at $r_\bullet \leqslant 1$ kpc.

NOTATION	FIELD NAME	UNIT	DESCRIPTION
Subhalo			
$M_\star$ / $M_{\rm gas}$	SubhaloMassType	$M_\odot$	Stellar- and gas mass
SFR	SubhaloSFR	$M_\odot$/yr	Star formation rate
$R_{\rm e}$	SubhaloHalfmassRadType	kpc	Stellar effective radius
$R_{\rm Sub}$	–	kpc	Subhalo radius, $R_{\rm Sub} = 5 \times R_{\rm e}$
x_0, y_0, z_0	SubhaloPos	kpc	Central coordinates
$v_{x,0}$, $v_{y,0}$, $v_{z,0}$	SubhaloVel	km/s	Central velocity components
All particle types			
m_*	Masses	$M_\odot$	Masses of particle cells
x_*, y_*, z_*	Coordinates	kpc	Coordinates of particle cells
$v_{x,*}$, $v_{y,*}$, $v_{z,*}$	Velocities	kpc	Velocity components of particle cells
Stars			
$a_\star$	GFM_StellarFormationTime	–	Scale factor at the time of formation
$\log(Z_\star/Z_\odot)$	GFM_Metallicity	$Z_\odot$	Metallicity
Black holes			
$\dot{M}_\bullet$	BH_Mdot	$M_\odot$/yr	Black hole accretion rate
Gas			
$\mathrm{SFR}_\diamond$	StarFormationRate	$M_\odot$/yr	Star formation rate
$x_{e,\diamond}$	ElectronAbundance	–	Electron abundance
$u_\diamond$	InternalEnergy	$(\mathrm{km/s})^2$	Internal (thermal) energy per unit mass
$T_\diamond$	–	K	Temperature (2.57)
$\mu_\diamond$	–	g	Mean molecular weight (2.56)
$\rho_{0,\diamond}$	Density	$\frac{10^{10}\,M_\odot/h}{(\mathrm{ckpc}/h)^3}$	Intrinsic co-moving mass density
$\rho_\diamond$	–	cm^{-3}	Particle number density (2.58)
$\log(Z_\diamond/Z_\odot)$	GFM_Metallicity	$Z_\odot$	Metallicity
$12 + \log(\mathrm{O/H})_\diamond$	GFM_Metals	dex	Oxygen abundance (2.59)
$\log(\mathrm{C/O})_\diamond$	GFM_Metals	dex	Carbon-to-oxygen abundance ratio (2.60)
$\boldsymbol{B}_\diamond$	MagneticField	G	Magnetic field strength vector
$B_\diamond$	–	μG	Average magnetic field strength (2.61)
$\mathcal{M}_\diamond$	Machnumber	–	Mach number
$v_{\mathrm{shock},\diamond}$	–	km/s	Shock velocity
$A_\diamond$	–	pc^2	Area of cell

Table 2.12: Table with an overview of the derived parameters from the IllustrisTNG simulations. Field names refer to available fields of the IllustrisTNG snapshot catalogs, as given in *Data Specifications, Illustris TNG*. References to equations are given in the last column ("Description") when applicable. Note that unit conversions have been applied in most cases.

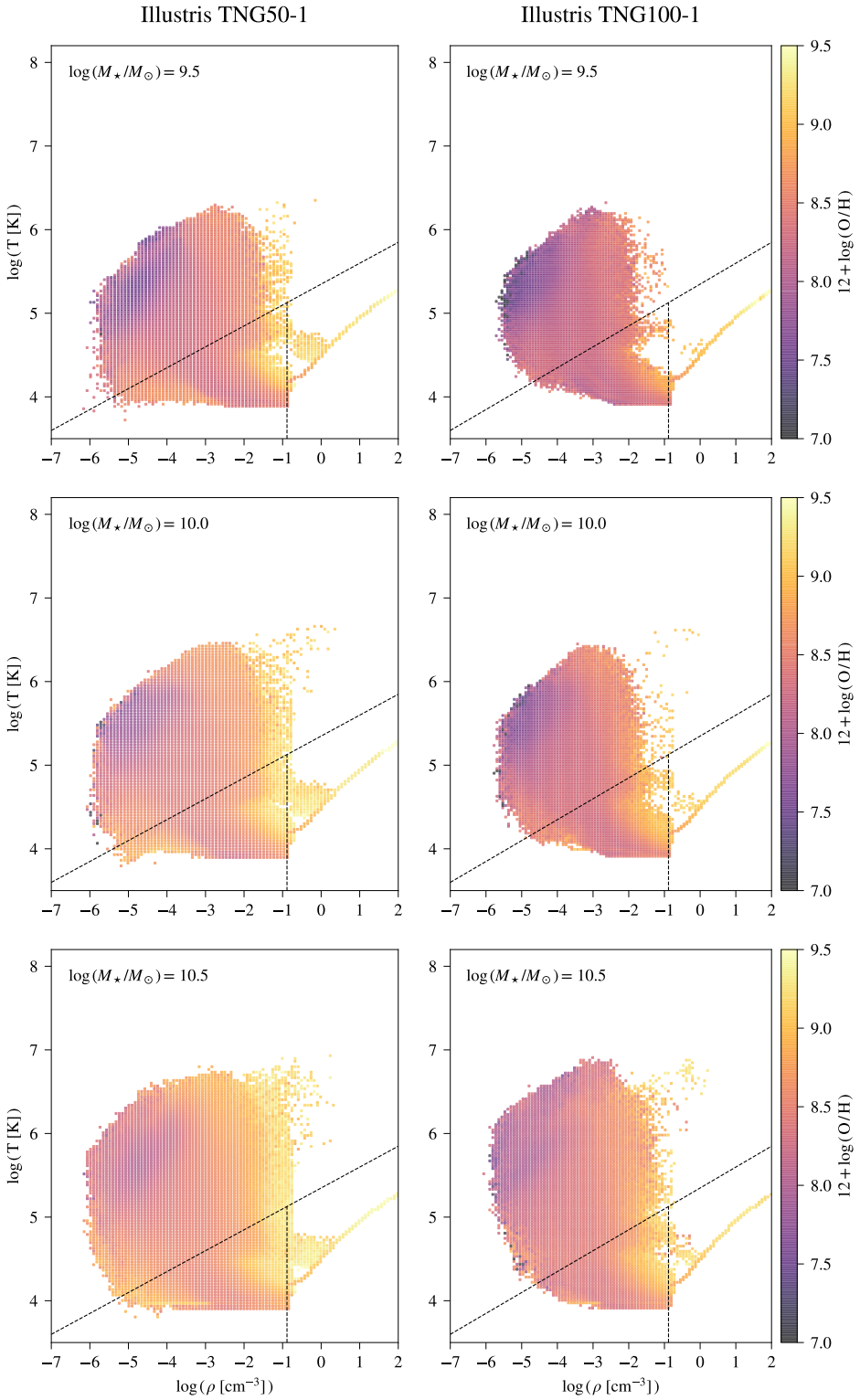

Figure 2.14: Density temperature phase diagrams of the 100 subhalos closest to the listed mass (upper left corner) for both IllustrisTNG50-1 (left column) and IllustrisTNG100-1 (right column). The 2D histograms are color-coded according to metallicity. The dashed lines indicate the temperature and density cuts applied when defining SF particles (equation 2.62). The upper region is the hot, circumgalactic medium, the lower left region is the cool, diffuse gas, and the lower right region is the cool, dense gas (star-forming interstellar medium).

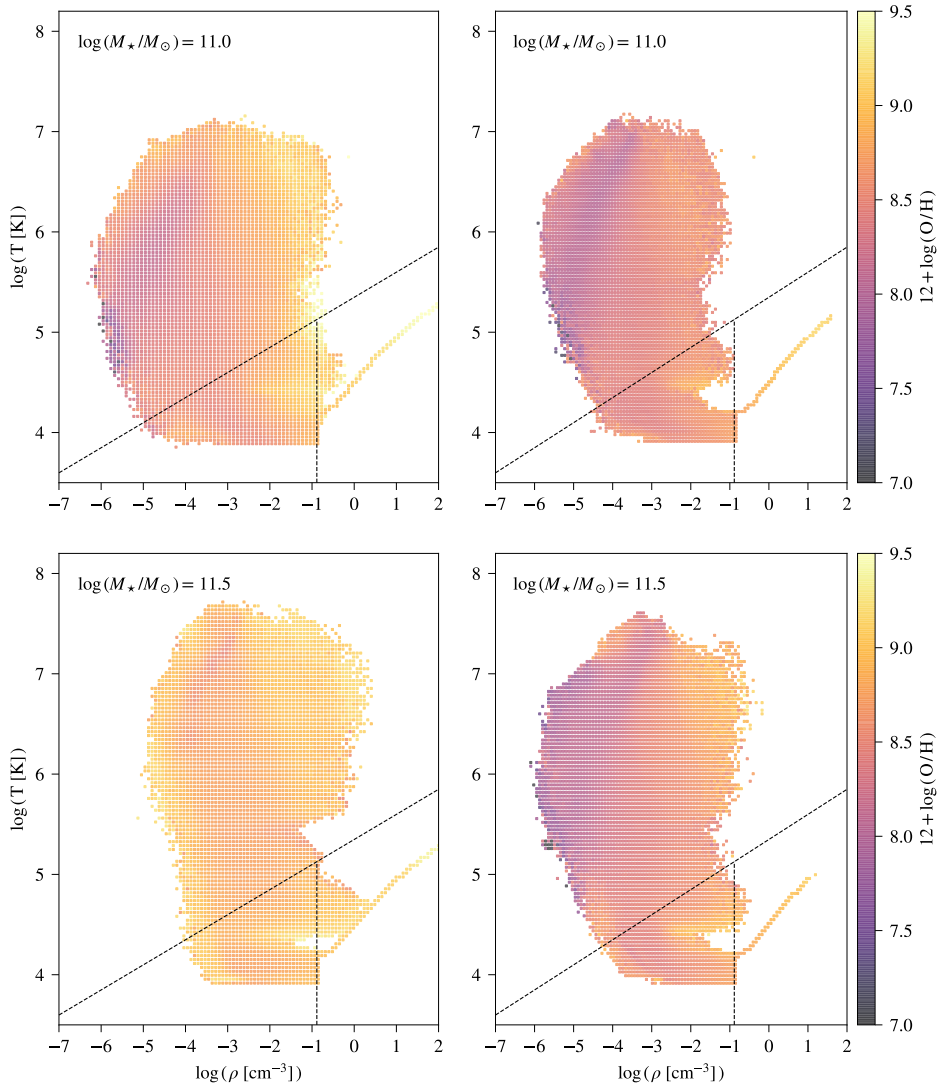

Figure 2.14: Density temperature phase diagrams of the 100 subhalos closest to the listed mass (upper left corner) for both IllustrisTNG50-1 (left column) and IllustrisTNG100-1 (right column). The 2D histograms are color-coded according to metallicity. The dashed lines indicate the temperature and density cuts applied when defining SF particles (equation 2.62). The upper region is the hot, circumgalactic medium, the lower left region is the cool, diffuse gas, and the lower right region is the cool, dense gas (star-forming interstellar medium).

2.2.4 Generating Spatially Resolved Emission Lines from Post-Processing of the IllustrisTNG Simulations

Spatially resolved synthetic emission lines are generated for the selected sample of subhalos from IllustrisTNG. This is done using the methodology described in Hirschmann et al. (2017) and Hirschmann et al. (2019), which contain self-consistent modelling of a variety of parameters, such as

- Nebular emission from H II regions around young stars
- Contributions to nebular emission from PAGB stellar populations
- Nebular emission from AGN narrow-line regions

Hence, by coupling the photoionization models with simulated galaxies from the cosmological (magneto-)hydrodynamic simulations IllustrisTNG, it is possible to produce mock observations of nebular emission. The integrated luminosities are then found by summing the contributions of each ionizing source (young stars, PAGB stars and AGN). The emission line models in Hirschmann et al. (2017) and Hirschmann et al. (2019) are computed using version c13.03 of Cloudy (Ferland et al., 2013), and accounts for dust grain interactions with photons, electrons and atomic ions in H II regions. I refer to table 1 of Hirschmann et al. (2017) for an overview of the parameters used in the nebular emission models.
The approach of generating synthetic emission lines is outlined in the following. Section 2.2.5 describe the approach of this work to effectively compare metallicity- and ionization gradients of the synthetic emission lines and intrinsic IllustrisTNG values to the ones of the observed galaxies.

Nebular emission from H II regions

The grid for modelling nebular emission of H II regions is adopted from Gutkin et al. (2016), which combine the stellar population synthesis model by Bruzual and Charlot (2003) with Cloudy following the method outlined by Charlot and Longhetti (2001). In this method, the spectral evolution of an H II region is convolved with a star formation history to yield galaxy-wide quantities. The final grid is build upon models wide ranges of

- Interstellar gas- and dust-phase metallicity, $Z_\star$
- Ionization parameter, $U_\star$, defined as the (dimensionless) ratio of the number density of hydrogen ionizing photons to that of hydrogen (equation 2.69)
- Dust-to-metal mass ratio, ξ_d
- H II region density, $n_{\mathrm{H},\star}$
- Carbon-to-oxygen abundance ratio, $(\mathrm{C/O})_\star$

The models (Hirschmann et al., 2017; Hirschmann et al., 2019) additionally adopt the default emission-line predictions of Gutkin et al. (2016) for 10 Myr old stellar populations with constant SFR. In addition, the Chabrier (2003) IMF (equations 2.47 - 2.48) is adopted, and is thereby consistent with the IMF used in IllustrisTNG. The metallicities of the ionizing stars are here adopted from the ambient ISM, which is a similar approach to that of IllustrisTNG. We here assume a fixed dust-to-metal mass ratio (ξ_d), as dust is not followed, a fixed hydrogen density n_{H}, as individual H II regions are not resolved, and a Solar C/O abundance.

Nebular emission from narrow-line regions of AGN

The grid of nebular emission models from Feltre et al. (2016) is adopted for AGN narrow-line regions. The AGN ionising spectrum, with radiation mostly in UV and soft X-ray, originate from the black hole gas accretion disk and the surrounding hot corona and is approximated by a broken power law (equation 5 of Feltre et al., 2016):

$$S_\nu \propto \begin{cases} \nu^{\alpha} & \text{for} \quad 0.001\,\mu\text{m} \leqslant \lambda \leqslant 0.25\,\mu\text{m} \\ \nu^{-1/2} & \text{for} \quad 0.25\,\mu\text{m} < \lambda \leqslant 10.0\,\mu\text{m} \\ \nu^{2} & \text{for} \quad \lambda 10.0\,\mu\text{m} \end{cases} \tag{2.65}$$

where α is adjustable in the frequency range of ionizing photons. The adopted grid from Feltre et al. (2016) is parametrized in terms of

- Interstellar metallicity in the narrow-line region, $Z_\bullet$
- Gas ionization parameter, $\mathrm{U}_\bullet$
- Dust-to-metal mass ratio, ξ_d
- The density of gas clouds, $n_{\mathrm{H},\bullet}$
- Carbon-to-oxygen abundance ratio, $(\mathrm{C/O})_\bullet$

and include both dust and radiation pressure.

Nebular emission from PAGB stellar populations

Contributions from PAGB stellar populations are modelled as described in Hirschmann et al. (2017). The grid is constructed from models of stellar populations with ages $3, 5, 7, 9$ Gyr and metallicities 0.008, 0.014, 0.017, 0.02 (see table 1 of Hirschmann et al., 2017). Each stellar population is modelled with CLOUDY using spectra of single-age, evolved stellar populations computed with the stellar population synthesis model by Bruzual and Charlot (2003). The final grid is described through the following parameters:

- Interstellar metallicity, $Z_\diamond$
- Stellar population age, $t_{\diamond,\mathrm{stars}}$
- Stellar population metallicity, $Z_{\diamond,\mathrm{stars}}$
- Gas ionization parameter, $\mathrm{U}_\diamond$
- Dust-to-metal mass ratio, ξ_d
- Hydrogen density, $n_{\mathrm{H},\diamond}$

where he last three parameters are consistent with those of the H II regions. As the stellar populations considered here are evolved, the interstellar metallicity $Z_\diamond$ is treated independently.

Coupling nebular emission models with IllustrisTNG galaxies

Appropriate nebular emission models for any simulated galaxy is selected by (self-consistently) matching model parameters to those of the simulated galaxy, as described in Hirschmann et al. (2017) and Hirschmann et al. (2019). In this approach, the spectral evolution of typical H II regions are convolved with the star formation history of the young stellar populations (age $< 10^8$ years) producing the ionizing photons (see Gutkin et al., 2016; Hirschmann et al., 2017)

to compute the integrated nebular emission of the galaxy. As described in Gutkin et al. (2016) and Hirschmann et al. (2017), optical line ratios in integrated spectra of nearby galaxies are similar to those of individual H II regions, and the parameters of the photoionization models in this approach should be interpreted as the galaxy-wide ones, thus describing an ensemble of H II regions. The methodology used here deviates from that of Hirschmann et al. (2017) and Hirschmann et al. (2019) in the sense that we couple the emission line models to simulations by matching model grid parameters to the values of individual cubes of each subhalo. As the cubes here are ($1\,\mathrm{kpc} \times 1\,\mathrm{kpc} \times 1\,\mathrm{kpc}$) in size, they are much larger than the size of typical H II regions ($\sim 10\,\mathrm{pc}$). The approach taken here can therefore be justified by the fact that each cube has the potential to host several H II regions with stellar populations of different ages. For model parameters not available from IllustrisTNG, the value is either computed (e.g. ionization parameter U, as will be described later) or sampled. Specifically, the Solar value is adopted for the dust-to-metal mass ratio $\xi_d = \xi_{d,\odot} = 0.36$, which sets the depletion of heavy elements onto dust grains.

The H II region models are coupled to IllustrisTNG subhalos by choosing a model with grid values that are closest to that of any given cube of a subhalo (see section 2.2.3). The interstellar metallicity $Z_\star$ is matched to the warm gas metallicity $\tilde{Z}_\diamond$ of the cube. For simplicity, the $\mathrm{C/O}_\diamond$ of any cube is assumed to be equal to the Solar value, as the value of the carbon-to-oxygen abundance ratio hardly affects the optical lines considered here (see e.g. Gutkin et al., 2016). In order to compare the grid model values of the gas ionization parameter $\mathrm{U}_\star$, the "simulated" ionization parameter U_sim first need to be estimated. First, the global volume-averaged gas density $\rho_{\diamond,\mathrm{glob}}$ is found from $\tilde{\rho}_\diamond$, which is used to get the volume-filling factor

$$\epsilon = \frac{\rho_{\diamond,\mathrm{glob}}}{\tilde{\rho}_{\diamond,\mathrm{SF}}} \tag{2.66}$$

where $\tilde{\rho}_{\diamond,\mathrm{SF}}$ is the density of warm/SF gas particles in the cube. This is used in conjunction with the metallicity $\tilde{Z}_\diamond$, $(\mathrm{C/O})_\diamond$ ($= (\mathrm{C/O})_\odot$), and ξ_d ($= \xi_{d,\odot} = 0.36$) as input for the emission line models, which predict rate of ionizing photons Q_H, obtained by multiplying the SFR by the rate output of a 10 Myr old stellar population with unit SFR and metallicity $Z_\star$ (Hirschmann et al., 2017). This value of Q_H is then used to compute the volume-averaged ionization parameter of the cube, as in equation 1 of Hirschmann et al. (2017):

$$\mathrm{U} = \frac{3\,\alpha_B^{2/3}}{4\,c} \left(\frac{3\,Q_\mathrm{H}\,\epsilon^2\,\tilde{\rho}_{\diamond,\mathrm{SF}}}{4\,\pi} \right)^{1/3} \tag{2.67}$$

where α_B is the recombination coefficient of hydrogen in the Strömgren theory for the Case B approximation, which is appropriate for most nebulae (Osterbrock and Ferland, 2006). Equation (2.67) can be derived from integrating the gas ionization parameter $\mathrm{U}(r)$, with r being the distance to the source, over a Strömgren sphere with radius R_S (see appendix B of Panuzzo et al., 2003):

$$\langle \mathrm{U} \rangle = \int_0^{R_\mathrm{e}} \frac{\mathrm{U}(r)\,4\,\pi\,r^2}{\frac{4\pi}{3} R_\mathrm{S}^2} \mathrm{d}r \tag{2.68}$$

where

$$\mathrm{U}(r) = \frac{Q(r)}{4\,\pi\,r^2\,n_\mathrm{H}\,c} \tag{2.69}$$

$$Q(r) = Q_\mathrm{H} - \frac{4\pi}{3} r^3 n_\mathrm{H}^2\,\alpha_B\,\epsilon, \text{ and} \tag{2.70}$$

$$R_\mathrm{S} = \left(\frac{3 Q_\mathrm{H}}{4\,\pi\,n_\mathrm{H}^2\,\alpha_B\,\epsilon} \right)^{1/3} \tag{2.71}$$

U thus depends on the SFR via the rate of ionizing photons Q_{H}, and global volume-averaged gas density $\rho_{\diamond,\mathrm{glob}}$ (via the filling factor ϵ). The definition of U in equation (2.67) will hereafter be referred to as the *intrinsic* ionization parameter of the IllustrisTNG subhalos. The intrinsic simulation values are described in sections 2.2.3 and 2.2.3 and table 2.12.

When coupling AGN nebular emission models to the simulations, model parameters are matched to the central values, that is cubes at $R < 1$ kpc. This is naturally only considered if a central accreting black hole is present in the subhalo, which is not always the case. Hence, the interstellar ionization, metallicity, (C/O) and density of the narrow-line region are matched to the central values of warm gas particles from the simulations. The luminosity L_{AGN} is matched to simulations using the accretion rate $\dot{M}_{\bullet}$ of central black hole.

The PAGB models are selected based on similarity of both PAGB parameters and parameters adopted from the H II region models, as noted above, to those of individual cubes in a subhalo. Hence, the quantities used in this selection process include: The age and -metallicity of PAGB stars (age > 1 Gyr), the interstellar metallicity and (C/O) abundance ratio, as well as the ionization parameter. The last quantity, the ionization parameter of gas ionized by emission from PAGB stars, is dependant on both the mass of PAGB stars $\tilde{M}_{\star,\mathrm{PAGB}}$ and the global volume-averaged gas density $\rho_{\diamond,\mathrm{glob}}$.

2.2.5 Simulated Metallicity- and Ionization Gradients

Deriving Gradients from 2D Maps of Simulated Galaxies

Synthetic Emission Lines

For the IllustrisTNG subhalos, a principal axis transformation was performed on all star-, gas- and black hole particles as described in section 2.2.2, where after the subhalos were projected face-on, and the radial coordinates are found using equation (2.34). Following the face-on projection, each cube is 'collapsed' into two dimensional squares (from now on referred to as spaxels) in the following manner. For the synthetic emission lines, the resulting luminosity $L_{i,j}$ for each spaxel (x_i, y_j) is found as the sum of the luminosities $\tilde{L}(x_i, y_j, z_k)$ of all cubic bins along the $z-$direction:

$$L_{i,j} = \sum_k \tilde{L}(x_i, y_j, z_k) \tag{2.72}$$

The luminosities $L_{i,j}$ are thereafter converted to fluxes $\mathcal{F}_{i,j}$, assuming each subhalo is situated at redshift z_g, with z_g being the redshift of (or distance to) the observed galaxy that the subhalo was selected upon. This conversion is carried out by first computing the luminosity distance of the respective subhalo (or, equivalently, observed galaxy), $D_{L,g}$, using the function `luminosity_distance` (assuming a Planck15 cosmology) included in the sub-package Cosmology of the Python module Astropy (Price-Whelan et al., 2018). The flux $\mathcal{F}_{i,j}$ of any spaxel (x_i, y_j) is then found by

$$\mathcal{F}_{i,j} = \frac{1}{4\pi\, D_{L,g}} \times 10^{L_{i,j}}\, L_{\odot} \tag{2.73}$$

SF spaxels are selected as having

$$\mathrm{SFR}_{i,j} = \sum_k \tilde{\mathrm{SFR}}_{\diamond}(x_i, y_j, z_k) > 10^{-8}\, M_{\odot}\,\mathrm{yr}^{-1} \tag{2.74}$$

with $\tilde{\mathrm{SFR}}_{\diamond}$ defined in section 2.2.3, as well as being categorised as SF according to the [N II] BPT diagnostic (as done for the observations). The selected spaxels are then used to derive the metallicity and ionization parameter using the calibrations described in sections 2.1.5 and 2.1.5, thus following the same prescription as for the observations.

Intrinsic Values from IllustrisTNG

The same spaxels selected above are selected for deriving the intrinsic IllustrisTNG metallicity and ionization. The metallicity of each spaxel $(\mathrm{O/H})_{i,j}$ is computed from the intrinsic hydrogen- and oxygen abundances of SF gas; that is, cube values $\tilde{\mathrm{H}}_\diamond$ and $\tilde{\mathrm{O}}_\diamond$ (as defined in section 2.2.3) calculated from gas particles obeying equation (2.62). Hence, applying an approach similar to equation (2.74), the metallicity of any spaxel is

$$12 + \log(\mathrm{O/H})_{i,j} = 12 + \log\left(\frac{\sum\limits_k \tilde{\mathrm{O}}_\diamond(x_i, y_j, z_k)}{\sum\limits_k \tilde{\mathrm{H}}_\diamond(x_i, y_j, z_k)}\right) \tag{2.75}$$

using the same notation as in section 2.2.3. The ionization of each spaxel is calculated as the first moment taken along the $z-$direction:

$$\mathrm{U}_{i,j} = \frac{1}{N}\sum_k \mathrm{U}(x_i, y_j, z_k) \tag{2.76}$$

with $\mathrm{U}(x_i, y_j, z_k)$ being the *intrinsic* ionization as defined in section 2.2.4.

Comparison of Synthetic- and Intrinsic Abundances

An overview of characteristics as well as results from this analysis, including the slope of metallicity gradients and total metallicities, is given in appendix E.

Figure 2.15 show the total metallicity $12+\log(\mathrm{O/H})$ derived from the intrinsic simulation values versus the value derived from the synthetic emission lines for the full sample of IllustrisTNG subhalos. It is evident here that the intrinsic metallicities are much higher (~ 0.4 dex) than the ones derived from the synthetic emission lines. This discrepancy is also seen in the derived metallicity gradients, and will be discussed in the following.

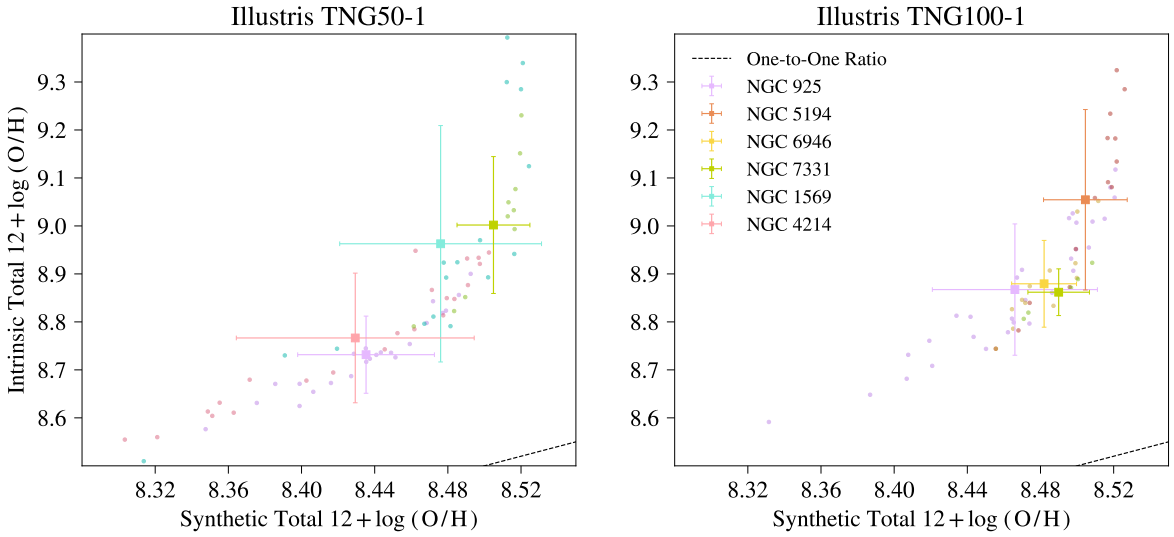

Figure 2.15: Same as figure 2.18 but showing the total metallicity $12 + \log(\mathrm{O/H})$.

The metallicity gradients for some selected galaxies, derived as described in section 2.2, using the synthetic emission lines and intrinsic values are shown in figures 2.16 and 2.17, respectively. A flattening of the gradient in the outer regions is present for several subhalos with masses $M_\star \gtrsim 10^{9.8} M_\odot$ (e.g. subhalos 411451, 336519 and 117256 in figures 2.16 and 2.17). This flattening is also seen in several observational and theoretical studies, as mentioned in chapter

1. It likewise reflects what is seen in the SF region of the density-temperature phase diagram in figure 2.14, that is, the SF gas with lower density but higher temperature have metallicities comparable to those with higher densities but lower temperatures.
It should be noted that we did not fit a set region for the whole sample, as is done in most large-scale studies. Rather, we chose a range suitable for each galaxy. This approach was exactly taken to exclude the flattening in the outer region while including as many data points as possible; the point of the truncation varies not only from galaxy to galaxy ($\sim 1.4R_e$ to $\sim 5.0R_e$), but also between the synthetic and intrinsic gradients. In particular, the truncation is often seen at larger radii for the intrinsic gradients compared to the synthetic (for each individual galaxy), and in some cases, the flattening is only observed (or, more prominent) in the intrinsic values. Hence, a common suitable fit range (i.e. for both the synthetic and intrinsic gradients) was chosen for each individual galaxy.
A flattening in the central region is also observed in both the synthetic (e.g. subhalos 411451, 336519 and 117256 in figure 2.16) and, to a lesser extent, the intrinsic gradients (e.g. subhalo 117256 in figure 2.17) for some of the more massive galaxies of our sample. Additionally, the intrinsic gradients sometimes present a steeper gradient towards the centre not seen in the synthetic ones. One example is subhalo 336519 (IllustrisTNG100), for which a flattening is observed in the inner region ($\lesssim 1.4R_e$) in the synthetic gradient (bottom left panel of figure 2.16), while a steepening is evident in the same region in the intrinsic gradient (bottom left panel of figure 2.17). This discrepancy most likely arise from resolution issues of the simulations.
While we intentionally excluded the outer region for galaxies exhibiting an exterior truncation, the flattening/steepening of the inner region was included in the fit (that is, at radii larger than the spatial resolution limit of the simulations). This may have contributed to the flattened synthetic gradients of the most massive galaxies (specifically those with $M_\star \gtrsim 10^{10.25} M_\odot$) of our sample. A better agreement may therefore have been found between the slopes of the synthetic and intrinsic gradients (and the corresponding normalizations, as discussed below) if the central region was excluded for galaxies with this feature.
The normalization $\beta_{\mathrm{O/H}}$ of the gradients derived from the two methods are clearly different, with the intrinsic ones on average being ~ 0.6 dex higher. The intrinsic $\nabla_{\mathrm{O/H\ [dex/}R_e\mathrm{]}}$ is likewise on average steeper by $\sim 0.15\,[\mathrm{dex}/R_e]$ and the intrinsic $\nabla_{\mathrm{O/H\ [dex/kpc]}}$ is on average steeper by $\sim 0.05\,[\mathrm{dex/kpc}]$. This discrepancy is illustrated in figure 2.18, which show $\nabla_{\mathrm{O/H}}$ in units of dex/R_e derived from the intrinsic simulation values versus the value derived from the synthetic emission lines for the full sample of IllustrisTNG subhalos. This is despite the fact that the gradients are measured in the same region using the same spaxels. These variations may arise from several factors, such as bias in the empirical calibrations used for the synthetic emission lines, and the fact that H II regions are unresolved in both the simulations and nebular emission line models, meaning we consider the gas metallicity of the ISM. The intrinsic metallicity gradients are based on the *intrinsic* oxygen abundances traced in the simulations, and the *entire* oxygen abundance is therefore considered. On the contrary, the synthetic gradients are based on model emission of H II regions, derived from photoionization models matched to the characteristics of each cube. The oxygen abundance is then derived using the same approach as for the observed galaxies, that is using emission of strong optical nebular lines. Assuming that our modelling of emission lines is reasonable, these discrepancies may be an indication that the PG16 calibration does not yield the correct oxygen abundances due to biases. However, several assumptions are made in the emission line models, in particular on the arrangement of H II regions and in the modelling of the ionization parameter. This will be discussed further in chapter 3 when considering the relation of the ionisation parameter with various strong line-ratios.

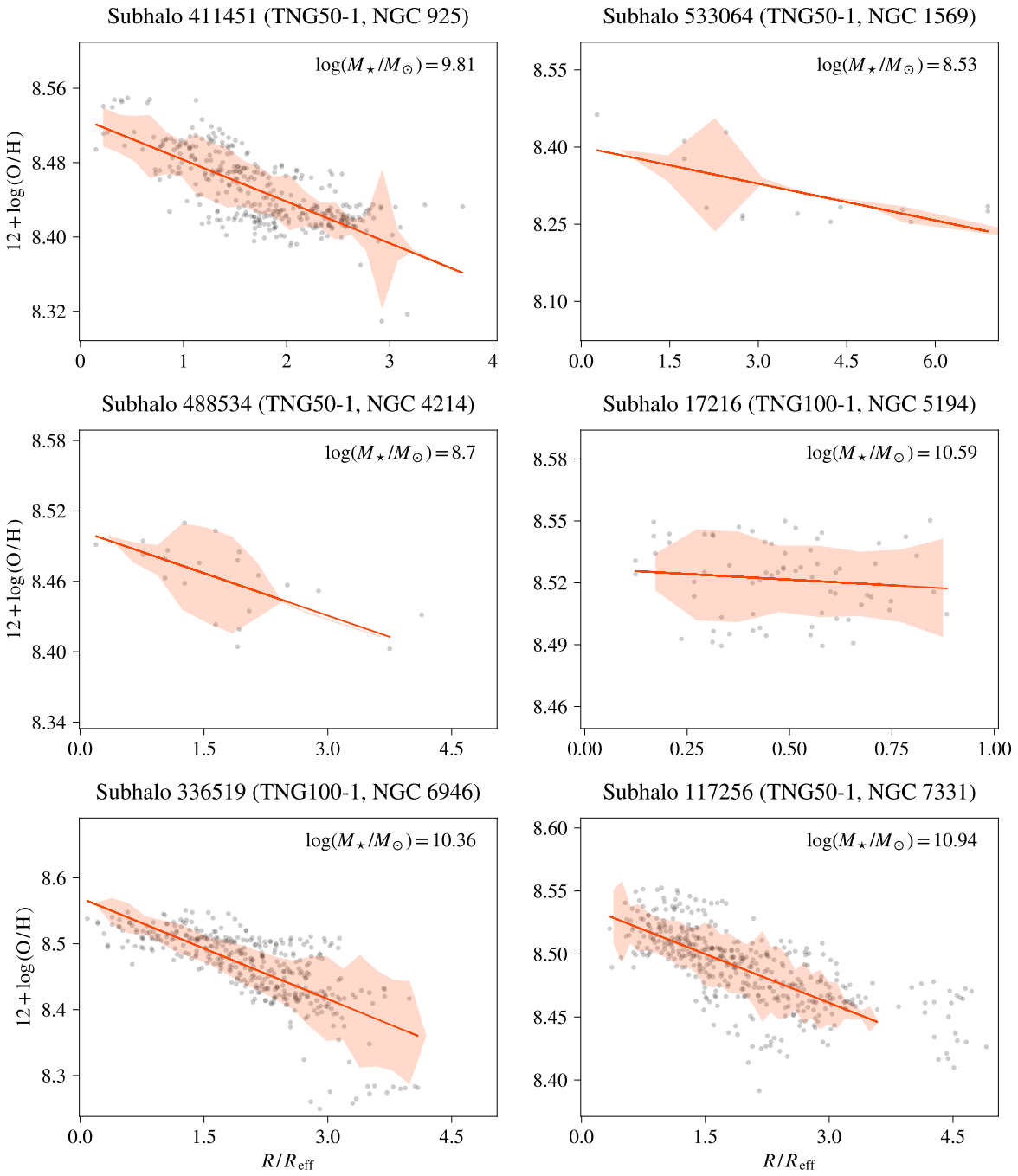

Figure 2.16: Metallicity gradients of some of the selected IllustrisTNG subhalos in units of [dex/R_e]. The red line is a linear χ^2 regression, the dots are metallicities derived from the synthetic emission lines, each categorized as SF from the [N II] diagnostic in section 2.1.4, and the shaded area is a 1σ scatter.

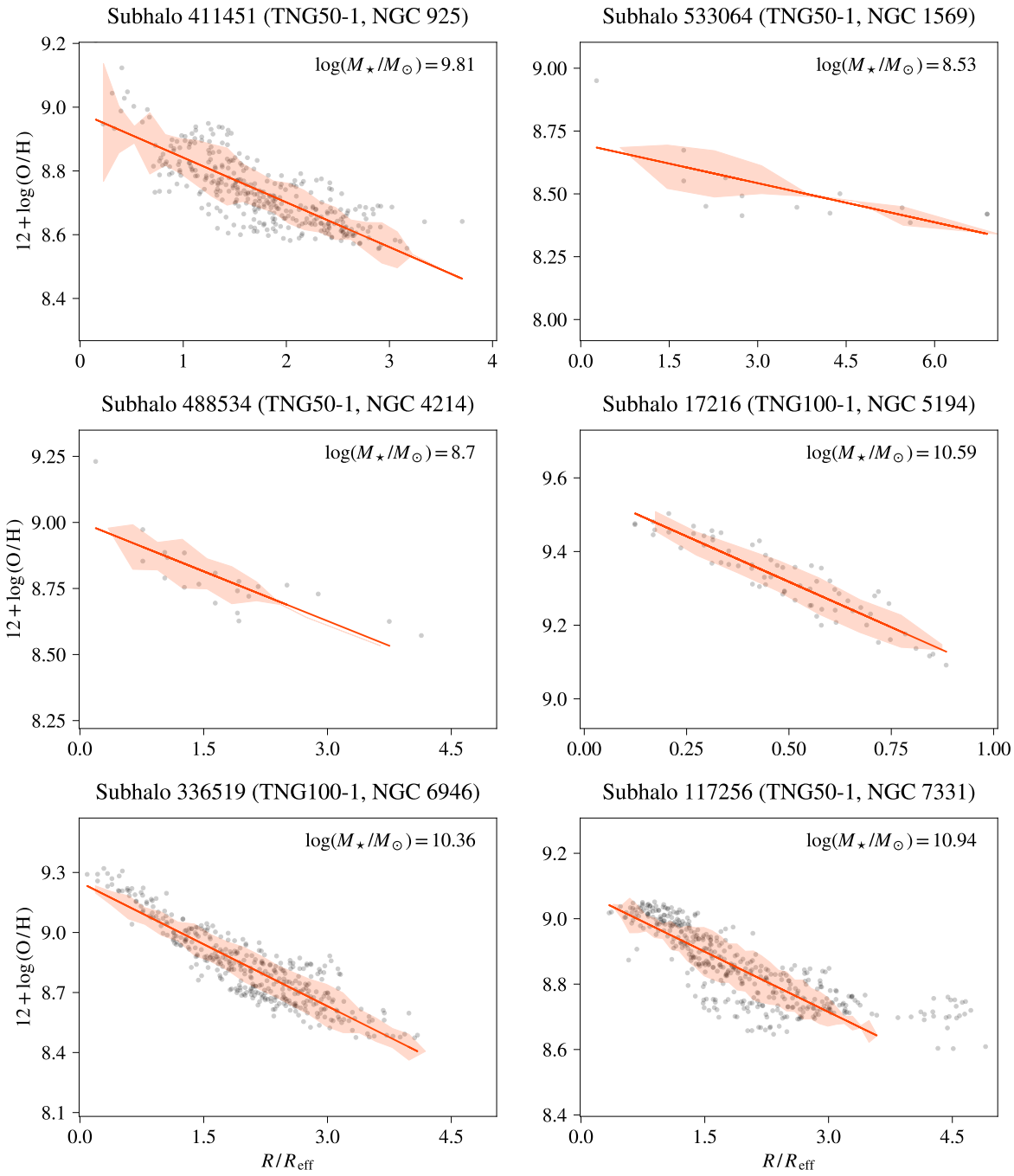

Figure 2.17: Same as figure 2.16, but derived from the intrinsic abundances of IllustrisTNG.

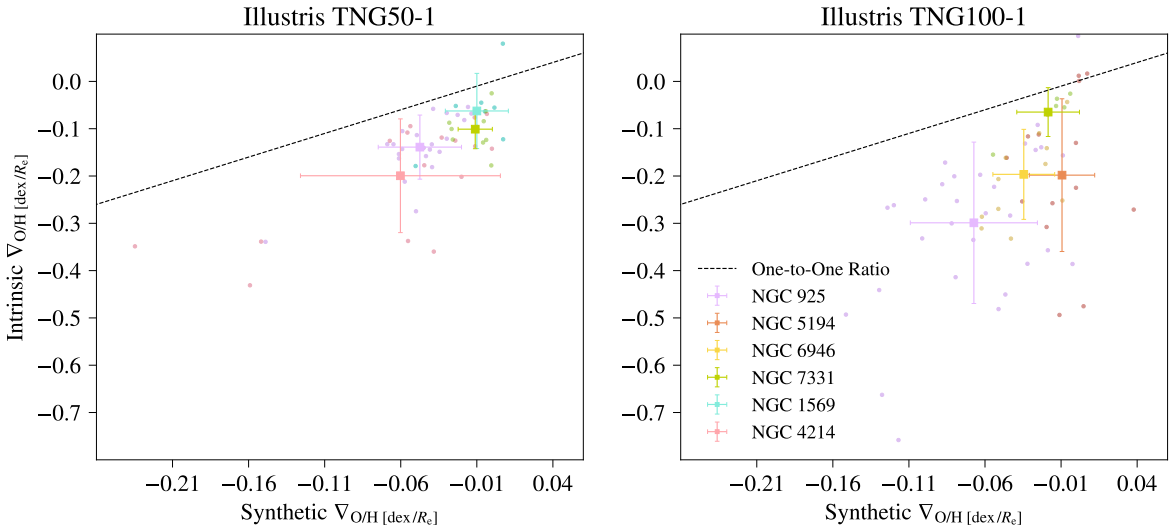

Figure 2.18: Slope of metallicity gradients in units of [dex/R_e] of the full sample of IllustrisTNG50 (left) and TNG100 (right) subhalos. The y-axis show the metallicity gradient derived from intrinsic simulation values, and the x-axis show the corresponding value for the same subhalo derived from the synthetic emission lines using PG16. The dashed line is a one-to-one relation. The color-coding denotes the observed galaxy to which any subhalo was matched, and the error bars show $\mu \pm \sigma$ for the respective samples.

Similarly, figure 2.19 illustrate the difference between ionization parameter gradients derived using the value predicted from the photoionization models (equation 2.67) versus the gradients derived using the Dors et al. (2016) calibration with the synthetic emission lines. The intrinsic ionization gradients are mostly positive, with slopes as large as $\sim$ 0.4 dex/R_e, while the synthetic gradients are much shallower, mostly scattered around -0.15 - 0.1 dex/R_e. This likely arise from assumptions made in the modelling of the ionization parameter, and will be discussed further in chapter 3.

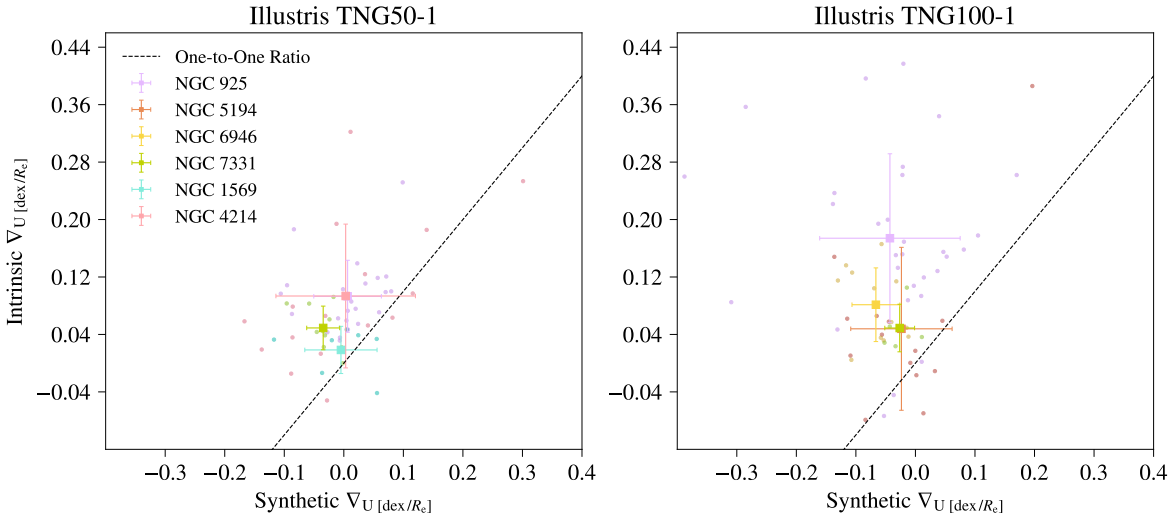

Figure 2.19: Slope of ionization gradients in units of [dex/R_e] of the full sample of IllustrisTNG50 (left) and TNG100 (right) subhalos. The y-axis show the ionization gradient derived using U_{sim} as predicted from the photoionization models, and the x-axis show the corresponding value for the same subhalo derived from the synthetic emission lines using the Dors et al. (2016) calibration. The dashed line is a one-to-one relation. The color-coding denotes the observed galaxy to which any subhalo was matched, and the error bars show $\mu \pm \sigma$ for the respective samples.

Origin of the Simulated Radial Metallicity Profile

This section focuses assessing which processes related to characteristic galactic properties are most prominent in shaping the metallicity gradients of simulated galaxies. Specifically, by comparing simulated galaxies of similar stellar mass, it is investigated how variations in SFR, sSFR, disc scale-length, AGN accretion rate, total metallicity and merger history affect the shape of metallicity gradients. Finally, the effect of changes in AGN- and star-formation driven feedback on the cosmic evolution of the metallicity gradient is examined through case studies in section 2.2.5.

Galactic Characteristics

Figure 2.20 show the slope of the derived metallicity gradients and total metallicities (using synthetic emission lines) versus stellar mass, sSFR, SFR and (central, < 1 kpc) black hole accretion rate for the sample of IllustrisTNG subhalos. The large scatter at low masses in panel (A) likely arise from resolution issues. As seen here, the slope of $\nabla_{\mathrm{O/H}}$ normalized to R_{e} exhibit only a weak correlation with stellar mass, where higher mass imply a shallower gradient. The same conclusion is found when considering the gas mass of the simulated galaxies. These general relations are also found in both observational- (Belfiore et al., 2017; Poetrodjojo et al., 2018; Sánchez-Menguiano et al., 2016) and theoretical (Tissera et al., 2015; Ma et al., 2017) studies, where the latter agree that no clear relation between metallicity gradient and stellar mass is present. Tissera et al. (2018) do, however, find a clear correlation between the gradient and disc size, such that larger discs imply flatter gradients, which has also been found in this analysis.

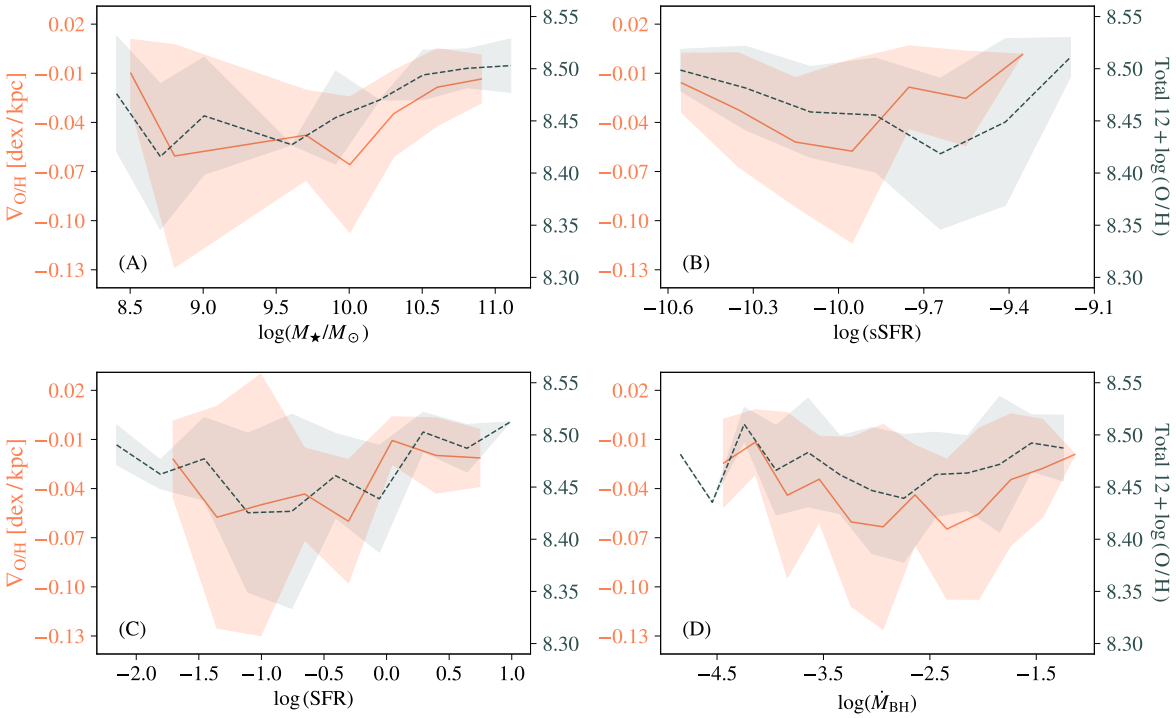

Figure 2.20: Slope of metallicity gradient $\nabla_{\mathrm{O/H\ [dex/}R_{\mathrm{e}}\mathrm{]}}$ (red, solid) and total metallicity (grey, dashed) derived from synthetic emission lines using PG16, versus stellar mass (A), sSFR (B), SFR (C) and central (< 1 kpc) BH accretion rate (D). Lines and shaded area denote $\mu \pm \sigma$ of $\nabla_{\mathrm{O/H}}$ resp. 12+log(O/H) in bins along the x-axis of sizes 0.3 dex (A), 0.2 dex (B), 0.35 dex (C) and 0.3 dex (D) bins.

In general, when considering the full subhalo sample, no clear correlations are found with any parameters with the shape of the metallicity gradient. However, when considering subhalos of similar stellar mass, some trends do show. In particular, subhalos with stellar

masses in the ranges $M_\star \lesssim 10^{9.5} M_\odot$ and $10^{9.5} M_\odot \lesssim M_\star \lesssim 10^{10.1} M_\odot$ have great varieties in the slope of the derived metallicity gradients ($\mu \pm \sigma = -0.04 \pm 0.06$ and -0.06 ± 0.04, respectively), while subhalos with stellar masses $M_\star \gtrsim 10^{10.1} M_\odot$ all exhibit shallow gradients ($\mu \pm \sigma = -0.02 \pm 0.02$).

Merger History

Merger trees of each subhalo is retrieved from the SubLink merger trees, which are available in the IllustrisTNG simulations. These merger trees are constructed at the subhalo level with the SubLink algorithm (see Rodriguez-Gomez et al., 2015), and a unique descendant is thereby assigned to each subhalo. We here follow only the main progenitor branch, meaning we follow only the descendant with the "most massive history" behind it. Using these merger trees, it is possible to detect mergers. We here define the *type* of merger by the stellar mass fraction of the merging subhalos, $f_\star$. Minor mergers are defined as having a stellar mass fraction $0.1 < f_\star \leqslant 0.25$ and major mergers are defined by $f_\star > 0.25$. The stellar- and gas mass used for calculating $f_\star$ and $f_{\rm gas}$ are measured within $2R_{\rm e}$.

It should be mentioned that the results discussed here are by no means statistically complete, as we are only considering simulated galaxies following the stellar mass, gas mass and SFR distributions of the six observed galaxies. The results can therefore be biased compared to a statistically significant sample of galaxies.

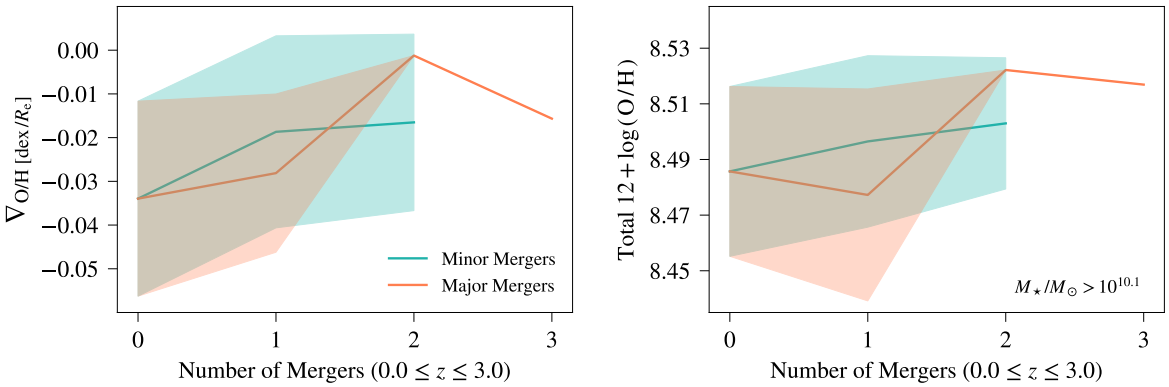

Figure 2.21: Slope of metallicity gradient (left) and total metallicity (right) derived from synthetic emission lines, versus number of mergers between $0.0 \leqslant z \leqslant 3.0$ for galaxies with $M_\star/M_\odot > 10^{10.1}$. The blue lines show galaxies that only experienced minor mergers, and the red lines show subhalos that only experienced major mergers. Lines and shaded area denote $\mu \pm \sigma$ of $\nabla_{\rm O/H}$ resp. $12 + \log({\rm O/H})$ in bins for each number of mergers.

Figure 2.21 show the slope of the metallicity gradient (in units of dex/$R_{\rm e}$) and total metallicity versus number of minor/major mergers for galaxies with stellar mass $M_\star/M_\odot > 10^{10.1}$ (a total of 96 galaxies). In the time between $0.0 \leqslant z \leqslant 3.0$, the distribution is as follows for this sub sample: 45 galaxies experienced no mergers; 32 galaxies experienced only minor mergers (i.e. no major mergers), of which 27 galaxies had 1 minor merger, and 5 galaxies had 2 minor mergers; 19 galaxies of the selected sample experienced only major mergers (i.e. no minor mergers), of which 17 galaxies had 1 major merger, 1 galaxy had 2 major mergers, and 1 galaxy had 3 major mergers.

As can be seen in figure 2.21, with increasing number of mergers, the slope of metallicity gradient flatten and the total metallicity increase. As only two galaxies experienced more than one major merger, the scatter is very large, and the sample here is very limited, no conclusions can be drawn on whether minor or major mergers have the largest impact on the gradient. The relation seen here is not likely to arise from a bias in stellar mass, as all subhalos independent of merger history have similar stellar mass, as highlighted in table 2.13.

As has been suggested in several observational studies (e.g. Sánchez-Menguiano et al., 2016),

interactions and minor mergers may increase the metallicity in the outer regions if the companion has a sufficiently high metal content, thus evening out the gradient. In general, mergers of galaxies in the local Universe have been confirmed in both observations and simulations to show shallower gradients. The flattening may arise from several merger-induced processes, such as radial inflows of metal poor gas diluting the inner ISM (Kewley et al., 2010; Rupke et al., 2010b; Rupke et al., 2010a; Perez et al., 2011; Sánchez et al., 2014b), galactic-scale metal redistribution (Ma et al., 2017), and feedback from merger-induced bursts of star-formation (Wuyts et al., 2016; Kobayashi, 2004).

(1) $N_{\rm M}$	(2) $S_{\rm min}$	(3) $M_{\rm min}$	(4) $S_{\rm maj}$	(5) $M_{\rm maj}$
1	27	10.5 ± 0.3	17	10.6 ± 0.2
2	5	10.5 ± 0.3	1	10.4
3	0	–	1	10.6

Table 2.13: Column 1: Number of mergers $N_{\rm M}$ between $0.0 \leqslant z \leqslant 3.0$; Column 2: Number of galaxies $S_{\rm min}$ that had $N_{\rm M}$ minor mergers between $0.0 \leqslant z \leqslant 3.0$; Column 3: Mean and standard deviation of stellar masses of the $S_{\rm min}$ galaxies from column 2; Column 4: Number of galaxies $S_{\rm maj}$ that had $N_{\rm M}$ major mergers between $0.0 \leqslant z \leqslant 3.0$; Column 5: Mean and standard deviation of stellar masses of the $S_{\rm maj}$ galaxies from column 4;. Only galaxies with stellar mass $M_\star/M_\odot > 10^{10.1}$ are considered here. The mean and standard deviation of stellar masses of the 45 galaxies with no mergers between $0.0 \leqslant z \leqslant 3.0$ is 10.5 ± 0.2.

The Cosmic Evolution of the Radial Metallicity Profile

This section contains a case-by-case study of three selected subhalos all from IllustrisTNG50; the first two with SubhaloIDs 63881 and 651841, sampled for NGC 925 and the third with SubhaloID 682134, sampled for NGC 1569;. We here follow the cosmic evolution of the intrinsic $\log(Z)$ metallicity gradient in units of effective radii, $\nabla_{Z\,[\mathrm{dex}/R_\mathrm{e}]}$, fitted in the region $R \leqslant 2\,R_\mathrm{e}$, along with merger history, AGN activity (through $\dot{M}_{\rm BH}$), star formation history (through SFR), as well as stellar- and cold (i.e. star-forming) gas mass. For consistency, the gradient is calculated using SF particles as defined in equation (2.62), and subhalos are projected face-on. In addition, some general observed trends will be discussed and compared to results from literature.

Subhalo 63881 (IllustrisTNG50-1, NGC 925)

Figure 2.22 show the cosmic evolution of subhalo 63881 from IllustrisTNG50-1, selected based on similarity to NGC 925. This subhalo experienced three mergers after $z = 2$:

- Major merger at $z \approx 1.5$, with $f_\star = 0.62$ and $f_{\rm gas} = 0.07$
- Minor merger at $z \approx 1.35$, with $f_\star = 0.16$ and $f_{\rm gas} = 0.04$
- Minor merger at $z \approx 0.68$, with $f_\star = 0.14$ and $f_{\rm gas} = 0.1$

While the gradient is seen to initially flatten until $z \sim 1.7$ in figure 2.22, it steepens as the AGN activity increase and the SFR drops. Specifically, the SFR is seen to drop by $\sim 0.4 M_\odot$/yr during the 700 Myr leading up to the major merger event. Around 255 Myr preceding the major merger ($z \sim 1.5$), $\dot{M}_{\rm BH}$ rapidly decline and the gradient is flattened ~ -0.47 to ~ -0.02 dex/R_e. The flattening of the gradient seen here, in conjunction with the decrease in BH accretion rate and low SFR, may be an indication of strong feedback from AGN. This feedback could potentially halt the accretion on the the BH, quench star formation, and eject

enriched gas out of the center.
In the 360 Myr between the major merger and the earliest minor merger, the gradient is slightly flattened by 0.04 dex/R_e, while the SFR and $\dot{M}_{BH}$ both increase to values similar to the ones before the initial drop at $z \sim 1.5$. It can also be seen in this epoch, between the two merger events, how the stellar mass and cold gas-phase metal content increase as a response to the major merger by $\sim 256\%$ and $\sim 1111\%$ with respect to their original values. The steepening of ∇_Z is again present just before the merger; the gas content can be affected by tidal forces occurring both before and during the merger event, which in turn affect the metallicity gradient.
After the first minor merger, $M_\star$ and $M_\diamond$ increase by $\sim 30\%$ and $\sim 3.6\%$, respectively. A rapid steepening of the gradient by ~ 0.35 dex/R_e is also evident here. A possible explanation for this steepening is the inflow of metal-poor gas from the interacting galaxy; the metal-poor gas can either settle in the outskirts, thus steepening the gradient, and/or potentially induce star-formation in the central region, enriching the central ISM with metals. The left panel of figure 2.22 suggests that from $z \lesssim 1.2$, the slope of the metallicity gradient correlate with the SFR, such that an increase in SFR yield shallower gradients, and vice-versa for a decrease in SFR.
The same trend of a sudden steepening of ∇_Z leading up to the merger event is seen by the time of the second (and last) minor merger. At around $z \sim 0.4$, the AGN activity increase, the SFR slowly decrease and ∇_Z reach somewhat of a stable value in the range -0.3 to -0.4 dex/R_e at $z \lesssim 0.25$.

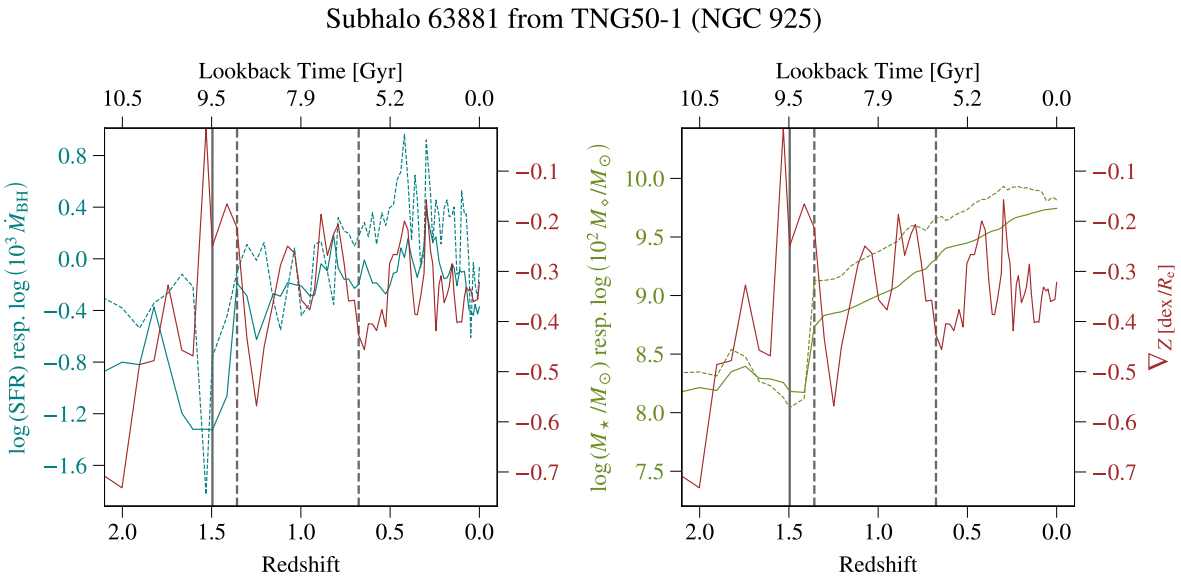

Figure 2.22: Cosmic evolution of slope of (intrinsic) metallicity gradient $\nabla_{Z\,[\mathrm{dex}/R_e]}$ measured at $\leqslant 2R_e$ in units [dex/R_e] (red line) for subhalo 63881 from IllustrisTNG50-1, with stellar mass $\log(M_\star/M_\odot) = 9.74$ at $z = 0$. The vertical black lines indicate major (solid) and minor (dashed) mergers. Left: Star formation rate log(SFR) (solid blue line) and (central $\leqslant 1$ kpc) black hole accretion rate $\log(\dot{M}_{BH})$ (dashed blue line). Right: Stellar mass $\log(M_\star/M_\odot)$ (solid green line) and cold (i.e. star-forming) gas mass $\log(M_\diamond/M_\odot)$ (dashed green line). The lower x-axis show redshift and the upper x-axis show the corresponding look back time in Gyr.

Subhalo 651841 (IllustrisTNG50-1, NGC 925)

Figure 2.23 shows the cosmic evolution of subhalo 651841 from IllustrisTNG50-1, that like subhalo 63881 was selected based on its similarity to NGC 925. This subhalo has not experienced any mergers after $z = 3.0$, which allow us to see how AGN- and star formation feedback affect the cosmic evolution of the metallicity gradient. As seen in figure 2.23, the slope of the metallicity gradient slowly flatten over time, besides the period $0.5 \lesssim z \lesssim 1.2$, where a large variation in ∇_Z occur. The first dip at $z \sim 1.25$, where ∇_Z steepens by ~ 0.15 dex/$R_{\rm e}$, is associated with corresponding declines in the cold gas mass $M_{\diamond}$ of ~ 0.15 dex (right panel of figure 2.23), a decrease in SFR of $\sim 0.55 M_{\odot}$/yr (left panel), and an increase in $\dot{M}_{\rm BH}$ of $\sim 7 \times 10^{-3} M_{\odot}$/yr. The second dip at $z \sim 0.9$, where ∇_Z steepens by ~ 0.17 dex/$R_{\rm e}$, is likewise associated with declines in $M_{\diamond}$ of ~ 0.16 dex, a decrease in SFR of $\sim 0.32 M_{\odot}$/yr, and an increase in $\dot{M}_{\rm BH}$ of $\sim 4 \times 10^{-3} M_{\odot}$/yr.

Following this epoch, the gradient slowly flatten with time, and after $z \sim 0.6$, the gradient seem to couple to the SFR, such that an increase in SFR corresponds to a flatter gradient, and a decrease in SFR corresponds to a steeper gradient. This is consistent with the first case study (subhalo 63881 from IllustrisTNG50-1, also selected for NGC 925). To some extent, the under-lying trigger here is the amount of cold gas; more cold gas increase the SFR, which flatten the gradient, while a lower inflow of cold gas decrease the SFR and in turn steepens the metallicity gradient.

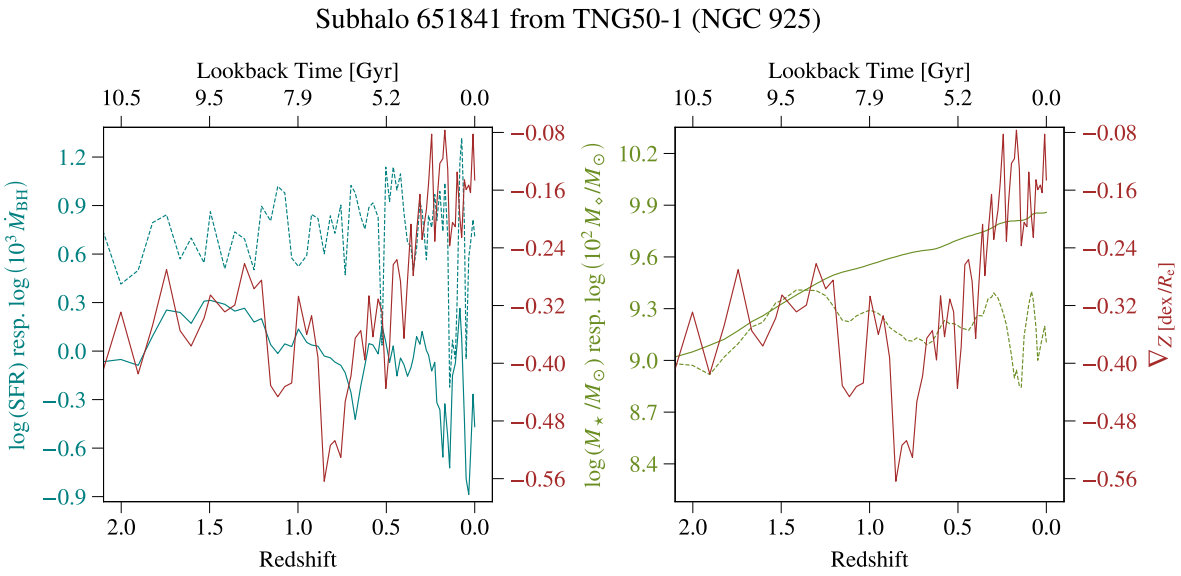

Figure 2.23: Same as figure 2.22 but for subhalo 651841 from IllustrisTNG50-1, with stellar mass $\log(M_\star/M_\odot) = 9.86$ at $z = 0$.

Subhalo 682134 (IllustrisTNG50-1, NGC 1569)

The cosmic evolution of subhalo 682134 from IllustrisTNG50-1, selected based on similarity to NGC 1569, is depicted in figure 2.24. This subhalo experienced two mergers after $z = 2$:

- Minor merger at $z \approx 1.11$, with $f_\star = 0.19$ and $f_{\text{gas}} = 0.08$
- Major merger at $z \approx 0.68$, with $f_\star = 0.39$ and $f_{\text{gas}} = 0.09$

During the 450 Myr leading up to the first (minor) merger at $z \sim 1.1$, the SFR increase by $\sim 0.02 M_\odot$/yr, and the gradient flattens by ~ 0.3 dex/R_e.
Between the minor and major merger, the SFR oscillates between 0.03 and $0.08 M_\odot$/yr, and a somewhat synchronized oscillation is present in the slope of the metallicity gradient between -0.77 and -0.05 dex/R_e, where, as seen before, an increase in SFR corresponds to a flattening of ∇_Z. In this time period, the stellar- and cold gas mass increase by $\sim 208\%$ and $\sim 141\%$. At $z \sim 0.85$, a central black hole is created and starts accreting at a relatively low rate of $\dot{M}_{\text{BH}} \sim 10^{-4} M_\odot$/yr.
In the 182 Myr leading up to the major merger occurring at $z \sim 0.7$, the gradient completely turns; the slope changes from $\nabla = -0.44$ dex/R_e at $z \approx 0.73$ to $\nabla = +0.49$ dex/R_e at $z \approx 0.7$. In the same period, the SFR drops by $\sim 0.01 M_\odot$/yr, and the stellar- and cold gas mass both decrease by 52.7% and 78.2%, respectively. The effective radius is also reduced from ~ 1.17 kpc to ~ 0.7 kpc. Figure 2.25 show the gas column density (top) and gas metallicity (bottom) of progenitors of subhalo 682134 at $z \sim 0.73$ (left) and $z \sim 0.7$ (right). When looking at the change in gas column density, the gas is not only expanded, but also morphologically disturbed; the two streams of gas, barely visible at $z = 0.73$, protrudes much farther (~ 50 ckpc) from the central region at $z = 0.7$. The mass loss seen in figure 2.24 is hence likely to be caused by the galaxy-galaxy interactions prior to the merger, either through expansion from tidal shocks or tidal stripping. While these streams are not as prominent when looking at the change in the gas metallicity distribution (bottom row of figure 2.25), the metallicity increase in particular in the lower-right region. The overall picture is nonetheless that the disturbances not only affect the large-scale distributions (as illustrated here), but also the small scale ones (illustrations can be retrieved from *Data Visualization, Illustris TNG*). As the metallicity gradient is measured from star forming gas particles, selected based on a density- and temperature cut and radial distance, the interaction at $0.7 \leqslant z \leqslant 0.73$ largely affects the selection of gas particles and

thereby the measured gradient.
After the major merger event, the SFR momentarily increases from $0.03 - 0.11 M_\odot$/yr, before it drops to $0.06 M_\odot$/yr. At this point since the merger, $\dot{M}_{\rm BH}$ has increased by $6 \times 10^{-4} M_\odot$/yr, the effective radius has changed from 0.56 to 1.47 kpc, and the gradient has evolved from being essentially flat to having a negative slope of $\nabla_Z = -0.98$ dex/$R_{\rm e}$. The major merger increased the stellar- and cold gas mass by 0.72 dex and 0.8 dex, respectively.
After $z \sim 0.64$, the SFR, $\dot{M}_{\rm BH}$ and cold gas mass slowly decrease until the present. The stellar mass slowly increases, the effective radius stays roughly constant, and the gradient evolves to a value of $\nabla_Z = -0.47$ dex/$R_{\rm e}$ at $z = 0$.

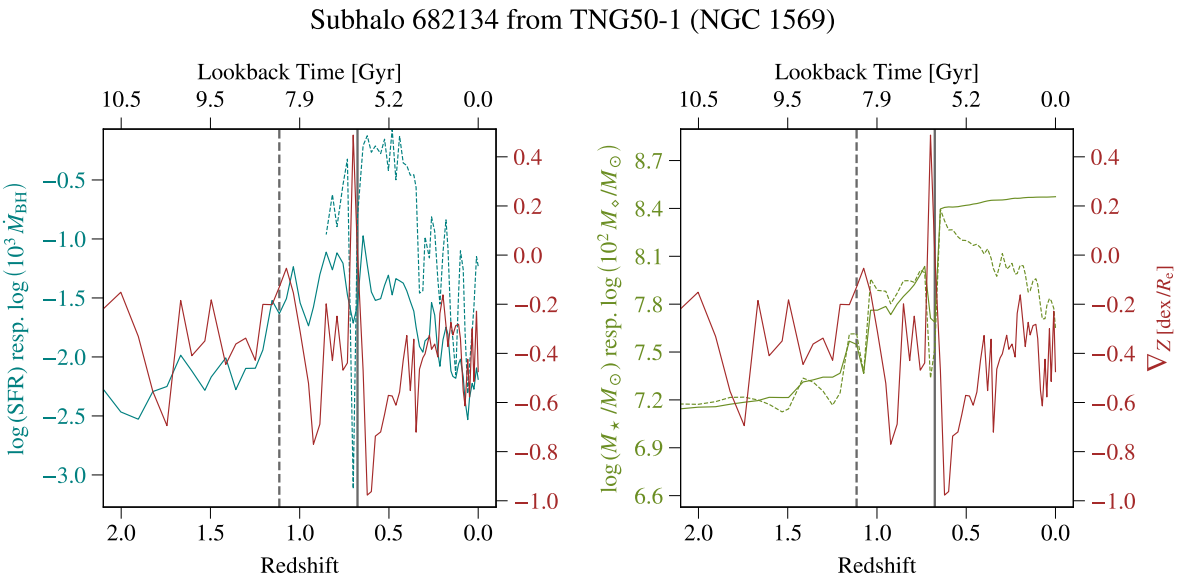

Figure 2.24: Same as figure 2.22 but for subhalo 682134 from IllustrisTNG50-1, with stellar mass $\log(M_\star/M_\odot) = 8.47$ at $z = 0$.

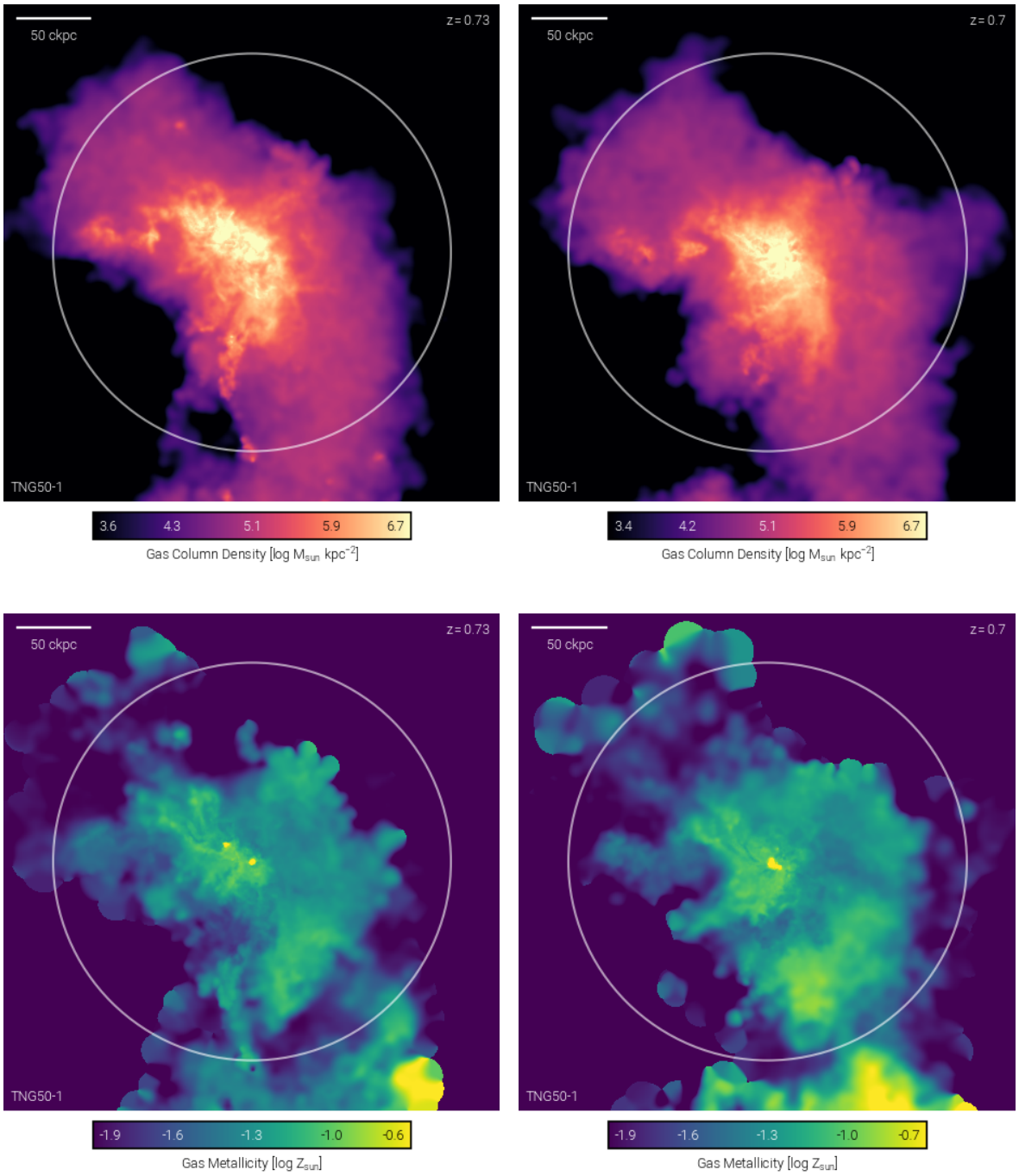

Figure 2.25: Gas column density (top) and gas metallicity (bottom) of progenitors of subhalo 682134 from IllustrisTNG50-1. The left column show the progenitor at $z = 0.73$, and the right show the progenitor at $z = 0.7$. The indicated scales of 50 ckpc correspond to 42.6 kpc at $z = 0.73$ and 43.4 kpc at $z = 0.7$. Image credit: *Data Visualization, Illustris TNG*.

From the above cases, some general trends can be derived:

- The metallicity gradient slowly flatten with time when not subject to any major disturbances (e.g. mergers, starbursts, large AGN activity). This likely happen as a product of the cold gas being exhausted in the inner regions, where star-formation initially was high (as evident from the steep gradient), and the outer regions, with slower rates of star-formation, have time to enrich the gas. For massive galaxies, re-accretion of previously ejected metals into the halo may also constitute to this observed flattening.
- Variations in ∇_Z on $\lesssim$ Gyr time-scales are mainly associated with mergers, changes in SFR and $\dot{M}_{\rm BH}$.
- At evolutionary stages temporally separated from merger events, the steepening of ∇_Z is often seen in conjunction with a decrease in SFR, indicating a lack of gas accretion.
- Galaxy-galaxy interactions prior to merger events can radically change ∇_Z along with SFR and $\dot{M}_{\rm BH}$. Initially, the gradient flattens as metal-poor gas in the outskirts is mixed with enriched gas from the companion. Inflow of low-metallicity gas, arising from loss of angular momentum due to turbulent motions, likewise flatten ∇_Z as the central ISM is diluted. Major merger events are indeed often followed by an increase in SFR and a flattening of ∇_Z. A subsequent (negative) steepening in ∇_Z is observed as a response to central star formation induced by the increase in gas density from the inflow.
- ∇_Z seem to be coupled with the SFR in several cases, such that an increase in SFR initially corresponds to a flatter gradient. This may be explained by the cold gas reservoir, as a larger amount of cold gas increase the SFR, which flatten the gradient, while a lower inflow of cold gas decrease the SFR and in turn steepens the metallicity gradient. A subsequent steepening of ∇_Z is also seen, indicating that massive stars have injected metals into the ISM.

Hence, these results point towards the cosmic evolution of ∇_Z being mainly governed by (i) merger events, which can cause gas mixing and induce star formation, (ii) strong starburst driven feedback, which can create intense outflows that redistribute metals on galactic scales, and (iii) gradual flattening over time, as the outer regions have time reach higher metallicities due to the lower SFR. This agrees with several results from literature as mentioned in chapter 1 (e.g. Fu et al., 2013; Belfiore et al., 2016; Ma et al., 2017).

Chapter 3

Discussion

This chapter includes first a comparison between the simulations and observations (section 3.1), followed by a discussion of some of the caveats of observations (section 3.2), simulations and emission line modelling (section 3.3), and our comparison technique (section 3.4). Specifically, the focus will be on the approach and methodology used in this work. Lastly, section 3.5 includes a comparison to metallicity gradients found in both theoretical (Hemler et al., 2021) and observational (Sánchez-Menguiano et al., 2016) studies.

3.1 Comparison of Simulations and Observations

3.1.1 Integrated Metallicity and Ionization Parameter

A comparison of the total metallicities obtained from the observations, synthetic emission lines and intrinsic simulation values are shown in figure 3.1. There is no question here, that using synthetic emission lines from photoionization models greatly improves the agreement between simulated and observed galaxies. For the three observed galaxies with stellar mass $< 10^10 M_\odot$, the total metallicities derived from the synthetic emission lines are generally higher by $\sim$ 0.17, 0.32 and 0.23 dex for NGC 925, NGC 1569 and NGC 4214, respectively. The agreement is much better for NGC 5194, NGC 6946 and NGC 7331, where the synthetic total metallicities are generally $\sim$ 0.09, 0.07 and 0.06 dex lower than the observed ones, respectively. The agreement between abundances derived from emission line models and observations, when compared to the higher intrinsic simulation abundances, may indicate (as previously mentioned) that the metallicity calibration we use (PG16) does not yield the correct values. Indeed, observations show large variations in metallicities derived using different calibrations. The difference between the metallicities derived using synthetic emission lines and intrinsic simulations could potentially be smaller or greater if another calibration was used. This is, however, beyond the scope of this work.

A similar comparison of the integrated ionization parameter is shown in figure 3.2. While the total metallicities derived using synthetic emission lines are in better agreement with the observations, the total ionization tend to be under-estimated. This point, together with the derived metallicities, is discussed later in sections 3.3 and 3.4.

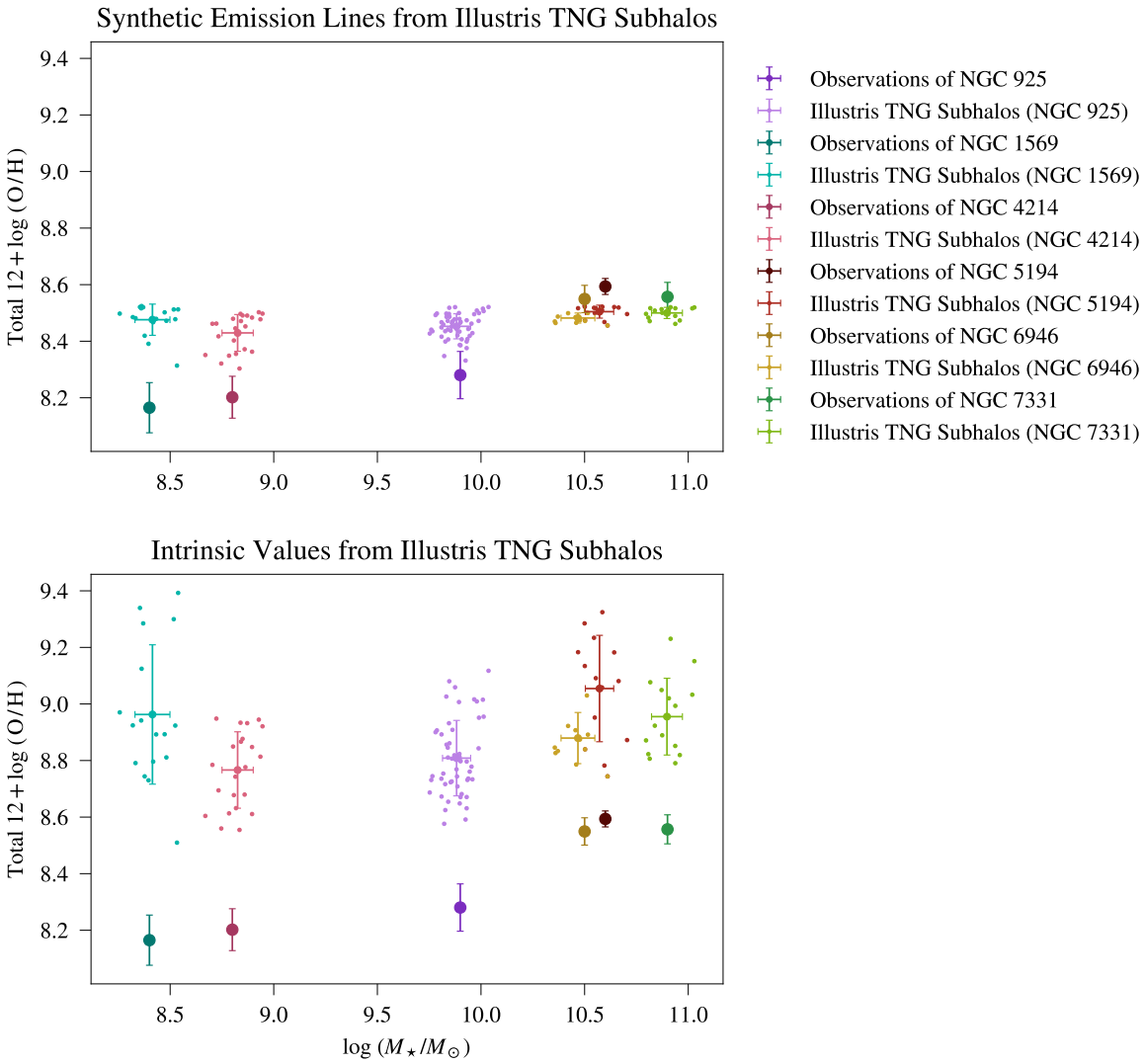

Figure 3.1: Total metallicity, derived from synthetic emission lines (top) and intrinsic simulation values (bottom), versus stellar mass of the full sample of IllustrisTNG subhalos. The small dots are values for individual subhalos, color-coded by the observed galaxy to which any subhalo was matched, and the error bar of the same color is $\mu \pm \sigma$ for the respective subhalo sample. The darker colored error bars show values of the observed galaxies. Values from the synthetic emission lines and observations are derived using the PG16 calibration.

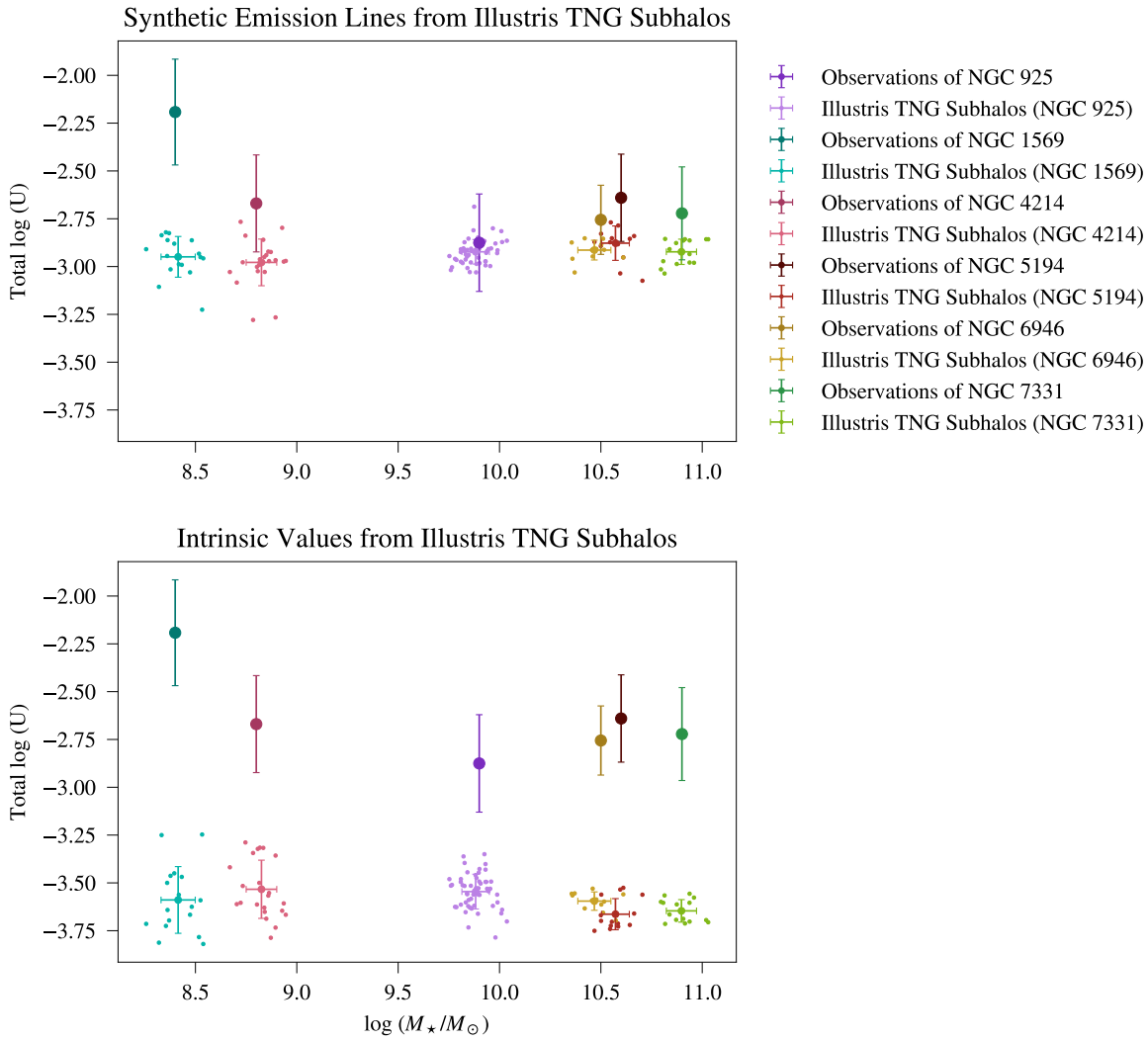

Figure 3.2: Total ionization, derived from synthetic emission lines (top) and intrinsic simulation values (bottom), versus stellar mass of the full sample of IllustrisTNG subhalos. The small dots are values for individual subhalos, color-coded by the observed galaxy to which any subhalo was matched, and the error bar of the same color is $\mu \pm \sigma$ for the respective subhalo sample. The darker colored error bars show values of the observed galaxies. Values from the synthetic emission lines and observations are derived using the calibration by Dors et al. (2016).

3.1.2 Radial Metallicity and Ionization Parameter Gradients

A comparison of results obtained from the observations, synthetic emission lines and intrinsic simulation values are shown in figures 3.3 and 3.4 for the slopes of the metallicity and ionization gradients in units of [dex/R_e], respectively. A better agreement between synthetic emission lines and observations are again present. It also worth noting that, even when basing the subhalo selection solely on stellar mass, gas mass and SFR, we are in most cases able to reproduce the observed gradients (see figure 3.3). This is despite no clear correlations were found among these parameters individually, as discussed in chapter 2. The intrinsic gradients also follow, albeit with a high scatter, the observed relation between $\nabla_{O/H}$ and stellar mass, that is; both the least massive ($M_\odot \lesssim 10^{8.7} M_\odot$) and the most massive ($M_\odot \gtrsim 10^{10.7} M_\odot$) galaxies have shallower gradients, whereas the other exhibit negative slopes.

As evident from figure 3.4, the intrinsic ionization gradients are mostly positive, while the synthetic ones mostly display values in the range -0.15 - 1.5 dex/R_e. NGC 4214 and NGC 925 both exhibit positive gradients in ionization parameter, and the best agreement with the intrinsic- and synthetic values is also found here. This will be discussed in further detail by considering caveats present in our methodology. Specifically, observational biases are discussed in section 3.2, the simulations and modelling of emission lines are discussed in section 3.3, and caveats of our approach in comparing simulations and observations are described in section 3.4.

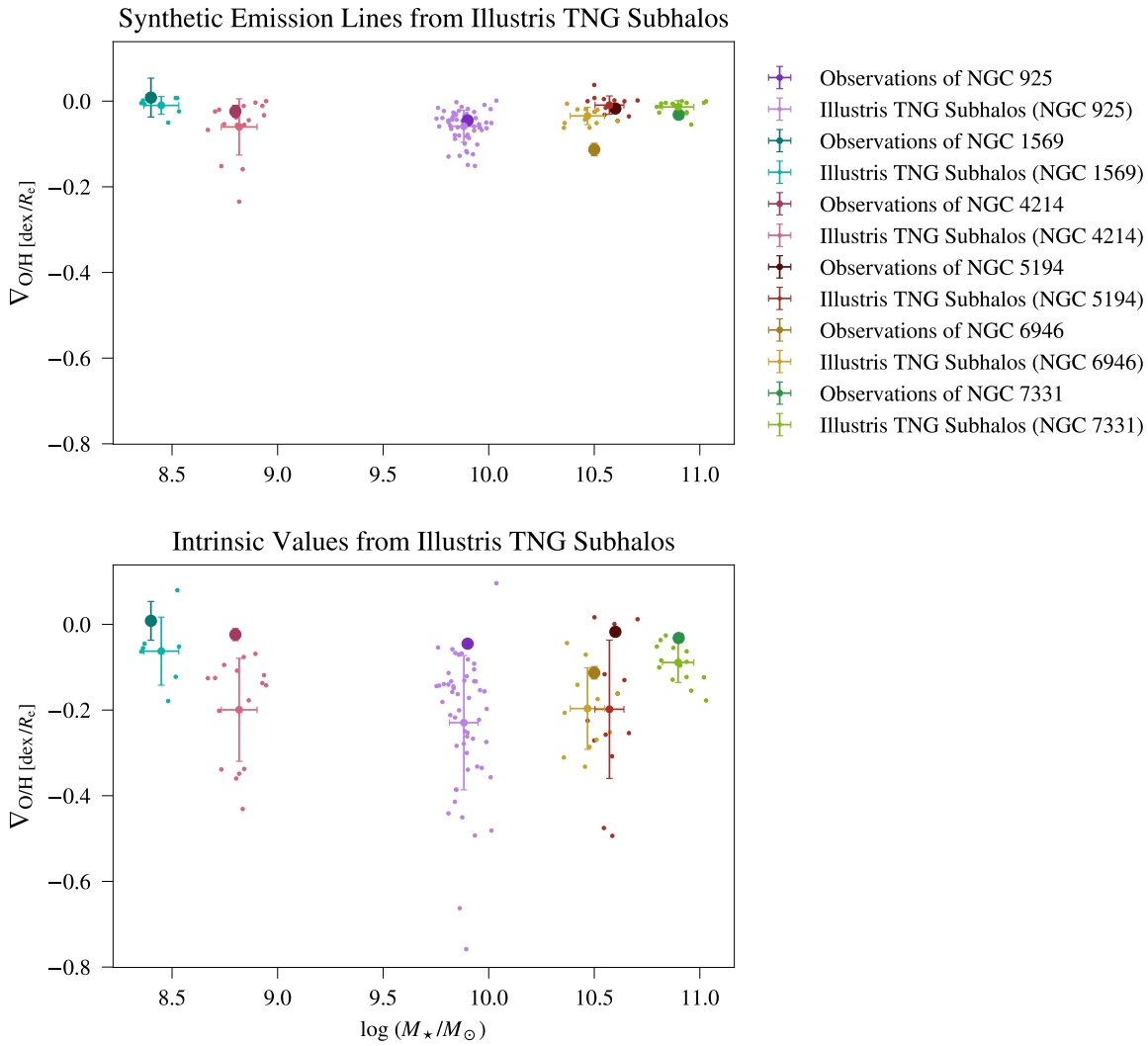

Figure 3.3: Slope of metallicity gradients in units of [dex/R_e], derived from synthetic emission lines (top) and intrinsic simulation values (bottom), versus stellar mass of the full sample of IllustrisTNG subhalos. The small dots are values for individual subhalos, color-coded by the observed galaxy to which any subhalo was matched, and the error bar of the same color is $\mu \pm \sigma$ for the respective subhalo sample. The darker colored error bars show values of the observed galaxies. Values from the synthetic emission lines and observations are derived using the PG16 calibration.

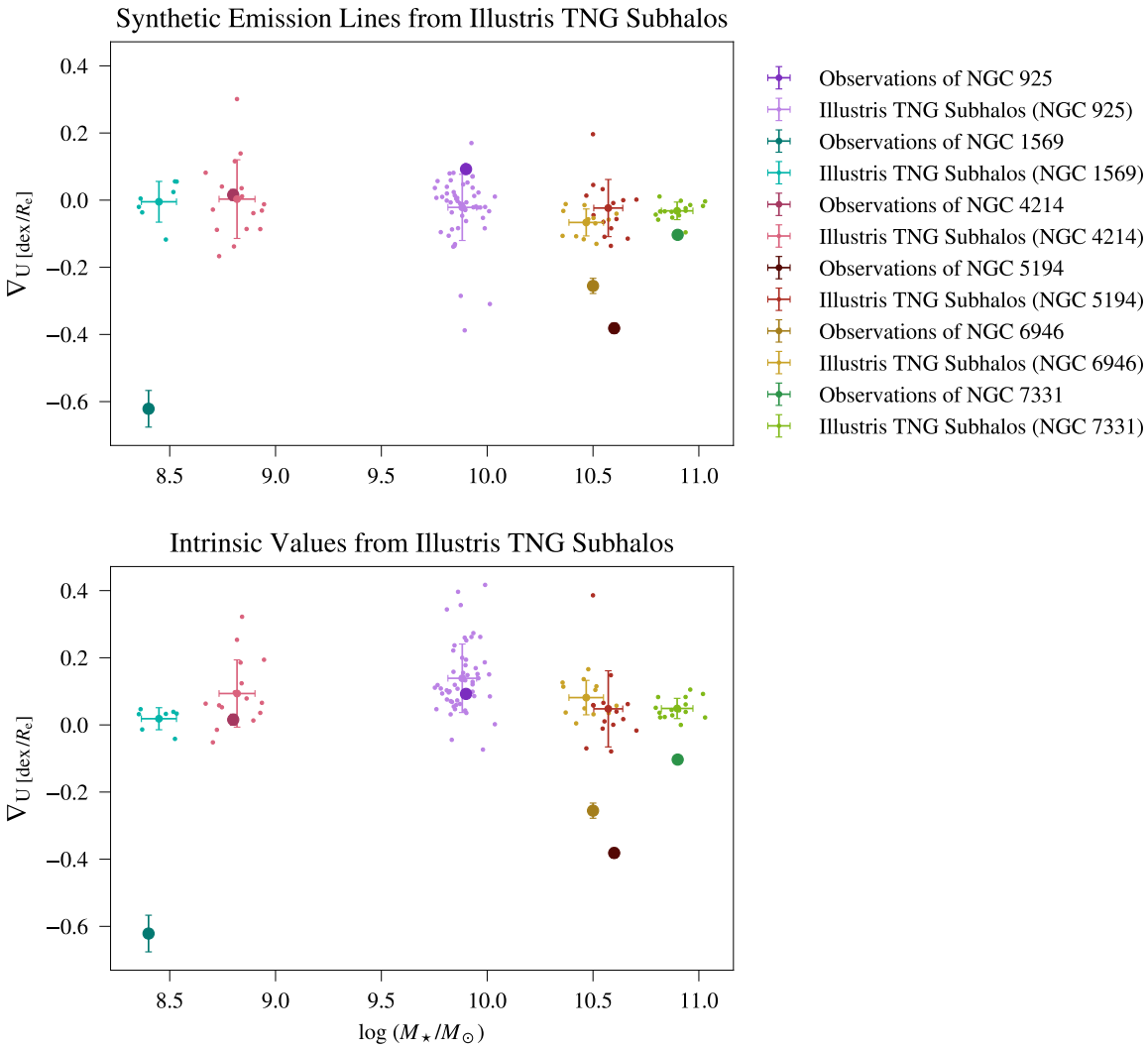

Figure 3.4: Slope of ionization parameter gradients in units of [dex/R_e], derived from synthetic emission lines (top) and intrinsic simulation values (bottom), versus stellar mass of the full sample of IllustrisTNG subhalos. The small dots are values for individual subhalos, color-coded by the observed galaxy to which any subhalo was matched, and the error bar of the same color is $\mu \pm \sigma$ for the respective subhalo sample. The darker colored error bars show values of the observed galaxies. Values from the synthetic emission lines and observations are derived using the calibration by Dors et al. (2016).

3.2 Caveats of Observations

The study by Kreckel et al. (2019) was previously considered in section 2.1.6, when interpreting over-abundances in metallicity present in the observed galaxies. To summarise this discussion, Kreckel et al. (2019) found that regions with enhanced oxygen abundances to be associated with high ionization parameter and higher Hα luminosity. On the other hand, our results presented a somewhat twofold relation between these parameters. Specifically, in agreement with Kreckel et al. (2019), oxygen-enhanced spaxels in NGC 925 and NGC 1569, tended to be associated with higher ionization parameter and/or higher Hα flux. It is worth noting here, that NGC 925 has a negative metallicity gradient ($\nabla_{\mathrm{O/H}}$ [dex/R_{e}] $= -0.045 \pm 0.008$) but a positive ionization gradient (∇_{U} [dex/R_{e}] $= 0.092 \pm 0.01$), while NGC 1569 has a flat metallicity gradient ($\nabla_{\mathrm{O/H}}$ [dex/R_{e}] $= 0.01 \pm 0.05$) and a negative ionization gradient (∇_{U} [dex/R_{e}] $= -0.62 \pm 0.05$). For NGC 5194, NGC 6946 and NGC 7331, a similar enhancement in oxygen abundance is mostly associated with either lower ionization parameter or higher Hα luminosity. These galaxies all exhibit negative, but flattened, metallicity gradients, along with negative ionization gradients (see table 2.7). The effect of possible biases in the calibrations we use to estimate metallicity and ionization parameter are hence discusses in the following, as motivated by observations by Kreckel et al. (2019).

Kreckel et al. (2019) observe a positive correlation between the metallicity and ionization parameter within each galaxy. The positive correlation between $12 + \log(\mathrm{O/H})$ (denoted Z in the remainder of this paragraph) and log(U) in individual galaxies is also seen in our sample for NGC 5194, NGC 6946 and NGC 7331. Although the PG16 calibration used for the metallicity estimation accounts for the degeneracy with ionization, the calibration we use for the ionization parameter (Dors et al., 2016) is a function of the derived metallicity; hence, the correlation in our sample likely arise from degeneracy. Another fact supporting this claim is that $\gtrsim 98\%$ of the spaxels of NGC 5194, NGC 6946 and NGC 7331 have metallicities $Z/Z_{\odot} > 0.97$ (with $Z_{\odot} = 8.69$) and $\log(N_2) \geqslant -0.6$ (with $N_2 = [\mathrm{N\,II}]\,\lambda\lambda\,6548, 84/\mathrm{H}\beta$, see equation 2.25), while $\gtrsim 97\%$ of the spaxels of NGC 925 and NGC 4214 also have $\log(N_2) \geqslant -0.6$, but with metallicities $Z/Z_{\odot} \leqslant 0.97$. For NGC 1569, $\gtrsim 66\%$ have $Z/Z_{\odot} \leqslant 0.97$ and $\log(N_2) \geqslant -0.6$, while $\gtrsim 34\%$ have $Z/Z_{\odot} \leqslant 0.97$ and $\log(N_2) < -0.6$. The division at $Z/Z_{\odot} \sim 0.97$ is chosen as two clearly separated, roughly Gaussian metallicity distributions with $\mu \pm \sigma = 0.94 \pm 0.01$ and $\mu \pm \sigma = 0.985 \pm 0.006$ arise when plotting a histogram of $Z/Z_{\odot}$ for all spaxels of all galaxies. The point $\log(N_2) \sim -0.6$, is what is used to divide the "upper" ($\log(N_2) \geqslant -0.6$) and "lower" ($\log(N_2) < -0.6$) branch in the PG16 metallicity calibration (see section 2.1.5). In fact, all spaxels with $\log(N_2) < -0.6$ have $Z/Z_{\odot} \leqslant 0.97$. Thus, considering spaxels with only $\log(N_2) \geqslant -0.6$ and $Z/Z_{\odot} > 0.97$, that is:

- 1646 spaxels from NGC 5194
- 1472 spaxels from NGC 6946
- 666 spaxels from NGC 7331

it is found that they exhibit a positive correlation in $Z/Z_{\odot}$ - log(U). Each galaxy is considered individually, and the correlation found using the Pearson correlation coefficient with a significance level of 0.05, along with a visual inspection of the data. This trend is however also found for the 386 spaxels in NGC 1569 with $\log(N_2) \geqslant -0.6$ and $Z/Z_{\odot} \leqslant 0.97$.

Contrary to our results, Kreckel et al. (2019) found no radial gradients in log(U). This may again be an indication of a degeneracy with metallicity in the calibration we use to estimate the ionization parameter. This would explain the negative ionization gradients seen in NGC 5194, NGC 6946 and NGC 7331, which all exhibit positive correlations between $Z/Z_{\odot}$ - log(U). The very negative ionization gradient ($\nabla_{\mathrm{U\ [dex/}R_{\mathrm{e}}]} = -0.62 \pm 0.05$) of NGC 1569, along with

the slightly positive metallicity gradient ($\nabla_{\mathrm{O/H\ [dex/}R_e\mathrm{]}} = 0.01 \pm 0.05$) may instead to a higher degree reflect local physical environment. NGC 1569 is characterized by a large starburst ($\log(\mathrm{sSFR}) = -9.62$), so the high ionization parameter in the central regions likely arise from the ongoing star-formation, while the positive metallicity gradient may indicate that metal-rich gas has been blown out from the center via supernova feedback and strong stellar winds.

Based on the above discussion, the discrepancies seen between observed and simulated values of both total ionization parameter and ∇_{U}, may hence reflect biases in the adopted calibrations. The following sections will, among others, further consider this issue.

3.3 Caveats of Simulations and Emission Line Modelling

While the issues described in the previous sections, being that the intrinsic simulations presents large discrepancies with observations relative to the emission line models, may reflect the calibrations used, there are also challenges arising from the simulations and the emission line modelling. Specifically, the simulations are unable to resolve the structure of the ISM, such as H II regions, and uncertain sub-resolution models are applied to account for this. Hence, the outputs of the photoionization models used to generate the synthetic emission lines describe an ensemble of H II regions. Additionally, interactions between the photon field and gas are not followed. The ionization parameter is hence derived using a number of assumptions, as described in section 2.2.4, and the emission lines and ionization parameter from the photoionization models are thus approximate.
With this in mind, we now show that our modelling approach is still consistent with observed relations. This section focuses on the $\mathrm{U} \propto Z^{-0.8}$ dependence, while section 3.4 explore differences and similarities to observed relations of metallicity and ionization parameter with strong line ratios.

Carton et al. (2017) examined the theoretical $\mathrm{U} \propto Z^{-0.8}$ dependence using SDSS DR7 sample, and found an anti-correlation between ionization parameter, $\log(\mathrm{U})$, and central metallicity, $\log(Z)$. Possible explanations for this dependence, as suggested by Kewley et al. (2013) and Dopita et al. (2006), include: (i) high metallicities yield higher opacities of the stellar winds, reducing the ionization parameter of the surrounding H II region by absorption of ionizing photons; (ii) photons are scattered more efficiently in photospheres at high metallicities, converting luminous energy flux to mechanical energy flux, leading to a lower degree of ionization of the surrounding H II region (Dopita et al., 2006).
Figure 3.5 show the total (intrinsic) ionization parameter versus total intrinsic metallicity $\log(Z/Z_\odot)$ for the sample of IllustrisTNG subhalos ($\mu \pm \sigma$, purple), together with a fit to the values of all spaxels (dashed black line, $\alpha = -0.57 \pm 0.03$) and the relation $\mathrm{U} \propto Z^{-0.8}$ (solid black line) from Carton et al. (2017). While Carton et al. (2017) considered galaxies from the SDSS DR7 sample with metallicities $-1.0 \lesssim \log(Z/Z_\odot) \lesssim 0.2$, the values from this thesis range $-2.0 \lesssim \log(Z/Z_\odot) \lesssim 0.6$. As can be seen in figure 3.5, at $-1.0 \lesssim \log(Z/Z_\odot)$, the intrinsic $\mathrm{U} \propto Z^{-q}$ relation is steeper, while it is shallower at $\log(Z/Z_\odot) \gtrsim 0.2$. Both these parameters, that is $\log(\mathrm{U_{sim}})$ (estimated from photoionization models) and $\log(Z/Z_\odot)$ (intrinsic value from IllustrisTNG), are used as inputs for the emission line models that produce the synthetic emission lines. Even though the intrinsic simulation values does not agree fully with this $\mathrm{U} \propto Z^{-0.8}$ relation, there is still an overall $\mathrm{U} \propto Z^{-q}$ trend present.

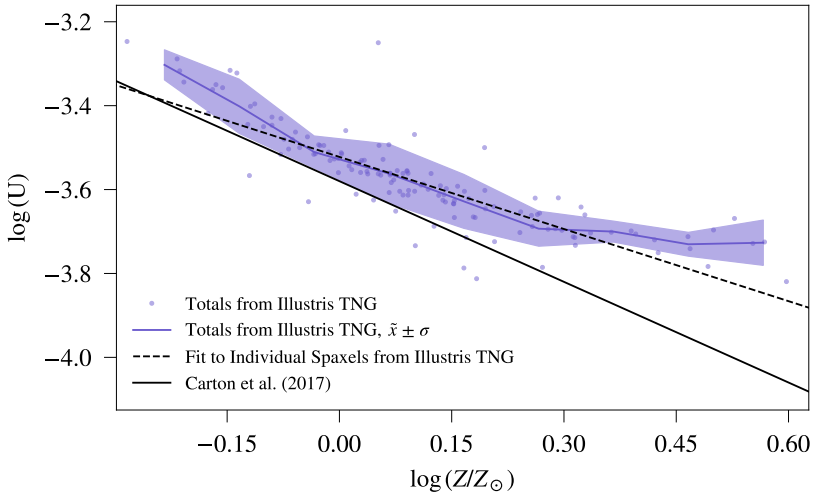

Figure 3.5: Total ionization versus total intrinsic metallicity $\log(Z/Z_\odot)$ of all selected IllustrisTNG galaxies. The purple line is the mean, and the shaded area is the standard deviation of 0.1 dex bins. The dashed black line is a fit with slope $\alpha = -0.57 \pm 0.03$ of all individual spaxels of these subhalos (individual spaxels are not shown in the plot). The solid black line is adopted from Carton et al. (2017) with $\alpha = -0.8$, using the total ionization parameter and central metallicity $\log(Z/Z_\odot)$ of the SDSS DR7 sample.

Figure 3.6 show the total ionization parameter versus total metallicity $12 + \log(\mathrm{O/H})$ of all observed galaxies (error bars), synthetic emission lines (green) and intrinsic simulation values (blue). The dashed black line is a fit to all individual spaxels (observed, synthetic and intrinsic). While this plot show $\log(\mathrm{U})$ versus $12 + \log(\mathrm{O/H})$, it is interesting to note that the values derived from the synthetic emission lines (shown in green) reproduce the observed change at $12 + \log(\mathrm{O/H}) \approx 8.4$. This is also seen when considering individual spaxels of both observed and synthetic galaxies; at $8.0 \lesssim 12 + \log(\mathrm{O/H}) \lesssim 8.4$, a higher ionization parameter imply lower metallicity, and at $12 + \log(\mathrm{O/H}) \gtrsim 8.4$, a higher ionization parameter imply a higher metallicity. This point traces back to the discussion in sections 2.1.6 and 3.2.

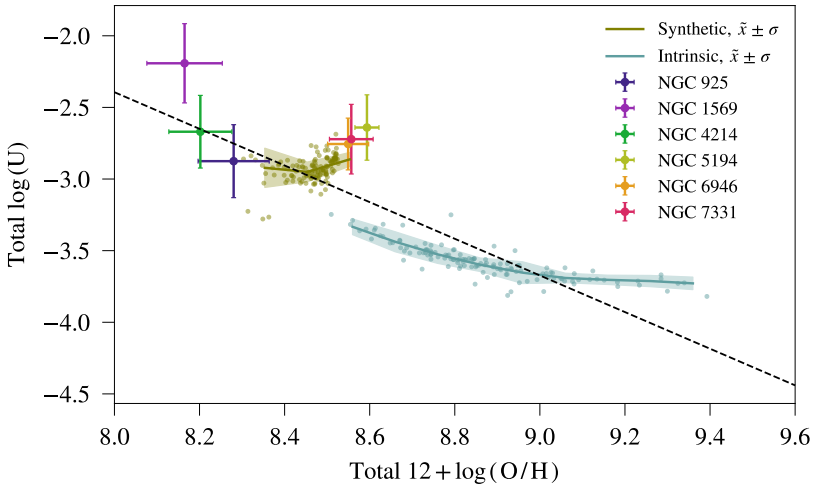

Figure 3.6: Total ionization versus total metallicity of all observed galaxies (error bars), synthetic emission lines (green) and intrinsic values (blue) derived from selected IllustrisTNG galaxies. The dashed black line is a fit with slope $\alpha = -1.3 \pm 0.2$ of all individual spaxels of both observations, synthetic emission lines and intrinsic values (individual spaxels are not shown in the plot). The solid green (blue) line and shaded area are the mean and standard deviation of 0.1 dex bins for parameters derived from the synthetic emission lines (intrinsic values) of IllustrisTNG.

3.4 Caveats of Comparison

As evident from the results presented in this work, a good agreement in found between observed values and those derived using emission line models. Summarising points made in the previous discussions, the discrepancy to the intrinsic simulations is likely two-fold, and may be due to (i) short-comings in the modelling of ionization parameter, as described above, and (ii) biases in the strong line calibrations. In order to assess these possibilities, we in this section compare observed relations of metallicity and ionization parameter with strong line ratios to the simulations.

Figure 3.7 show values of the metallicity versus the line ratios

$$\frac{[\mathrm{S\,II}]\,\lambda\lambda\,6717,31}{\mathrm{H}\alpha}, \quad \frac{[\mathrm{N\,II}]\,\lambda\,6584}{\mathrm{H}\beta}, \quad \frac{[\mathrm{O\,III}]\,\lambda\,5007}{\mathrm{H}\beta} \tag{3.1}$$

color coded by ionization parameter for each spaxel, both for observations and simulations. Similar diagrams, but for values of the ionization parameter versus the line ratios, color coded by metallicity, are shown in figure 3.8.
For the simulations (right panel in both figures), both the metallicity and ionization parameter is derived from the intrinsic simulation values, while values of the line ratios are taken from the synthetic lines of the same spaxel. Corresponding plots comparing observations to parameters derived solely from the synthetic emission lines are shown in figures D.1 and D.2 in appendix D.

It is clear from figures 3.7 and 3.8 that, while the synthetic line ratios are in good correspondence with observed values, the intrinsic metallicities and ionization parameters are not. The intensity of emission lines in H II regions are governed not only by metallicity, but also variations in electron density and continuum ionization (Kewley et al., 2013). In particular, the value for $\log(\mathrm{U_{sim}})$, which captures these quantities, has implications on the synthetic metallicities, as this parameter is used as input for the synthetic emission line models as described in section 2.2.4. In fact, at fixed metallicities, the ionization parameter largely affects the variation in line ratios (Kewley et al., 2013; Dopita et al., 2000). At high metallicities, Kewley et al. (2013) find that a higher ionization parameter yield smaller [N II]/Hα values, while at low metallicities, higher ionization parameter yield larger values of [O III]/Hβ. As we are effectively putting bounds on the photoionization powered by UV radiation from young, massive stars, this limits the values of collisionally excited lines like [S II] $\lambda\lambda\,6717,31$, [N II] $\lambda\,6584$ and [O III] $\lambda\,5007$ with respect to the recombination lines Hα and Hβ. Indeed, higher values for the ionization parameter $\log(\mathrm{U_{sim}})$ would allow lower values of the line ratios given in (3.1). This would correspondingly allow lower values of metallicity, thereby lessening the discrepancy between results from the synthetic emission line models and observations, as seen in e.g. figure 3.1 (top panel). In general, a wider range in values of $\log(\mathrm{U_{sim}})$ would yield greater varieties in the derived metallicity, thereby affecting $\nabla_{\mathrm{O/H}}$.

The main take away from this discussion is, that while simulations and observations are in rough agreement on the relation between metallicity and the considered line ratios, a larger discrepancy is present for the relation with log(U). It is hence likely that both points stated in the beginning of this section are contributors, that being biased calibrations used in the observations, and simplified modelling in the simulations.

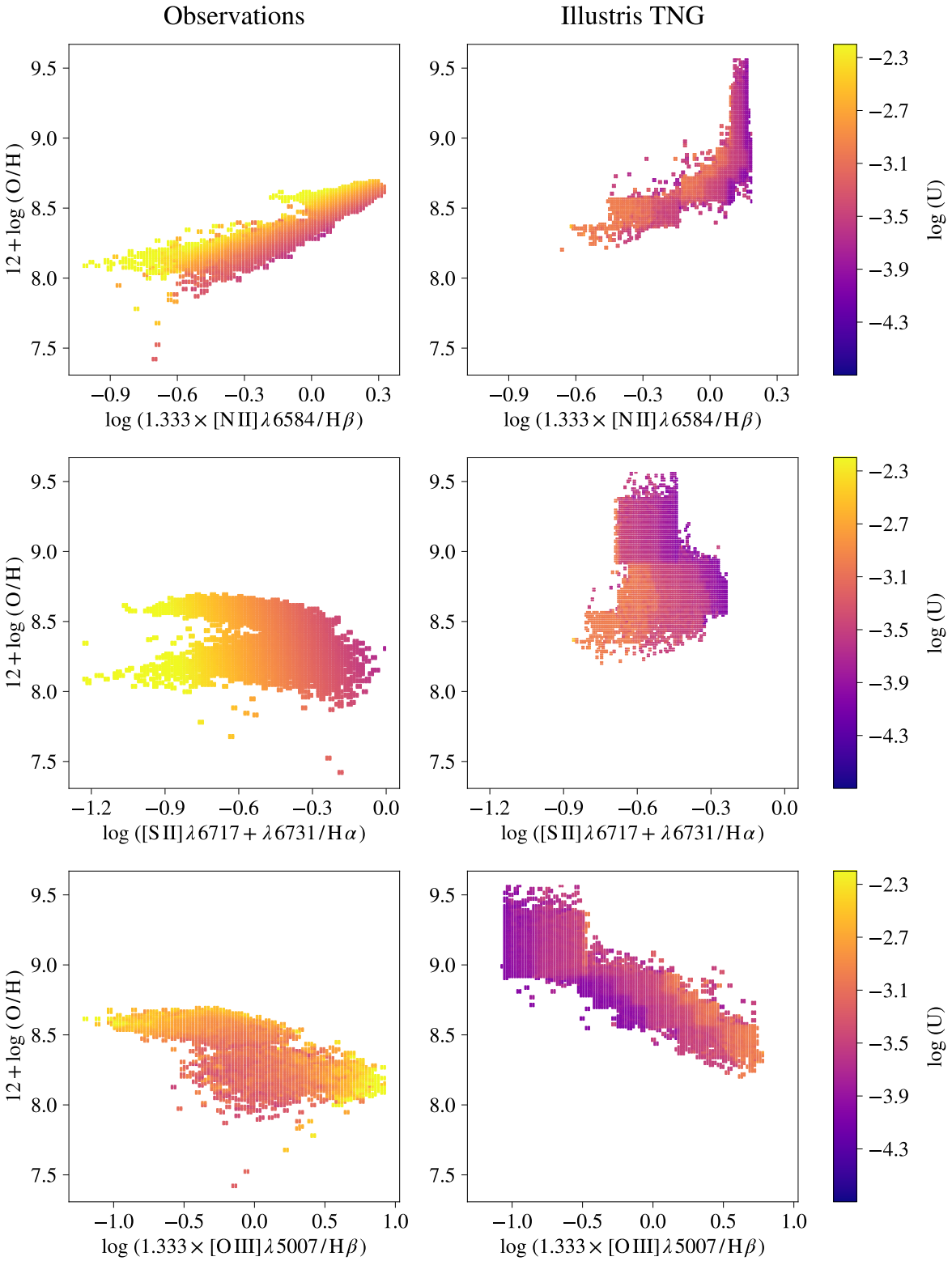

Figure 3.7: 2D histogram showing line ratios versus metallicity for individual spaxels in the observed sample (left) and the simulated sample (right), color-coded by ionization parameter. For the simulated sample, both the metallicity and ionization parameter are derived from the intrinsic IllustrisTNG values, while the line ratios are derived from the synthetic emission lines.

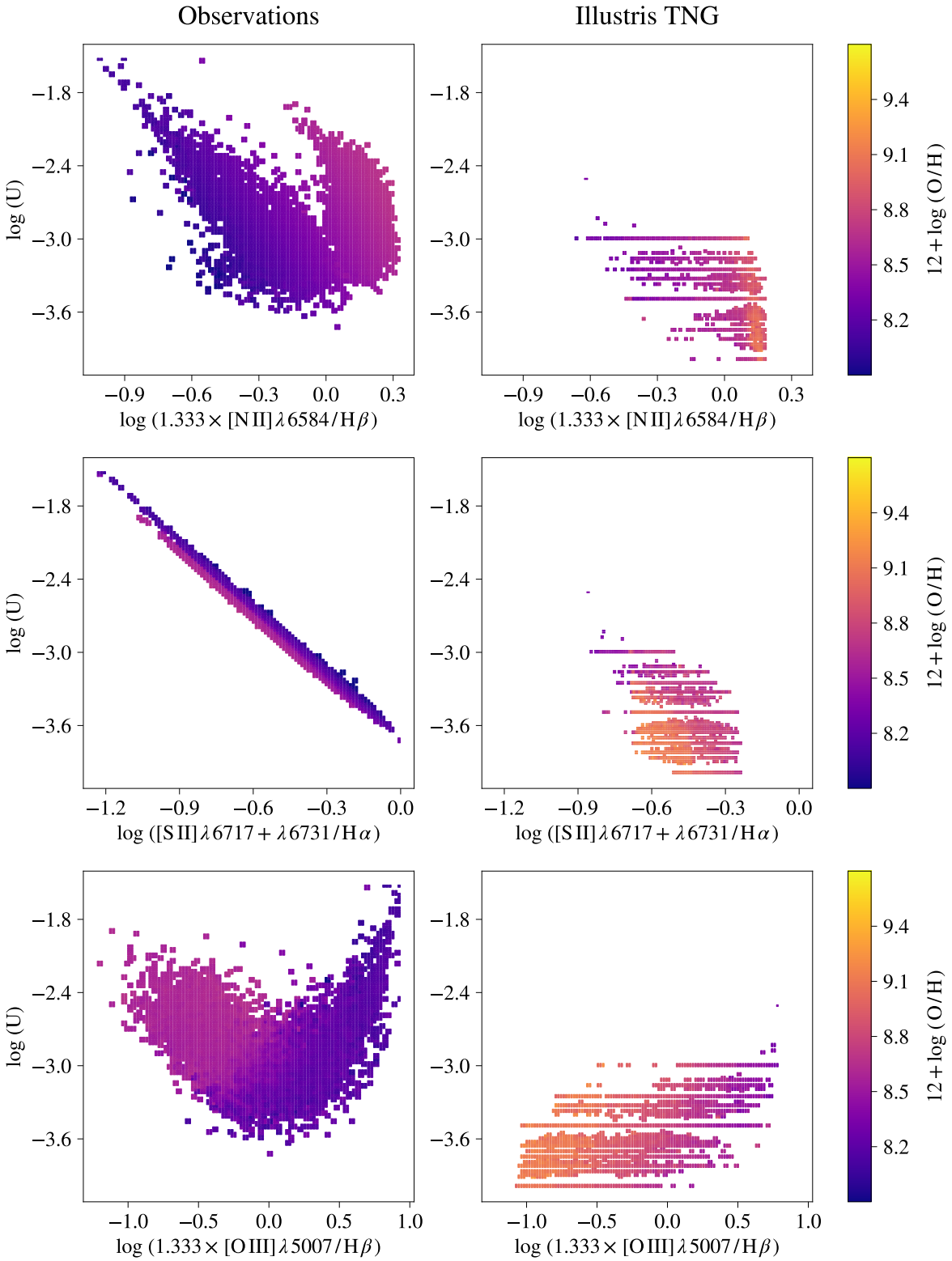

Figure 3.8: 2D histogram showing line ratios versus ionization parameter for individual spaxels in the observed sample (left) and the simulated sample (right), color-coded by metallicity. For the simulated sample, both the metallicity and ionization parameter are derived from the intrinsic IllustrisTNG values, while the line ratios are derived from the synthetic emission lines.

3.5 Comparison to Literature

Hemler et al. (2021) measured metallicity gradients of IllustrisTNG50 star-forming galaxies. Their gradients were based on median and standard deviations in abundances from pixels in 2D maps, consisting of gas particles with $n_{\rm H} \geqslant 0.13{\rm cm}^{-3}$. They only fitted the region $R_{\rm in} + 0.25(R_{\rm out} - R_{\rm in})$, where $R_{\rm in}$ is the 3D distance from the center of the galaxy for which 5% of the total SFR of a galaxy is enclosed, and $R_{\rm out}$ is the distance for which 90% of the total SFR within 10 kpc of $R_{\rm in}$ is enclosed. Figure 3.9 compares the gradients derived in this work to the results of Hemler et al. (2021) at $z = 0$. The values adopted from Hemler et al. (2021) are peak and spread of log-normal fits to the gradient distributions of mass bins centered at 9.75 (423 galaxies), 10.25 (263 galaxies), and 10.75 (102 galaxies). While the results are comparable at $M_\star \gtrsim 10^{10.25} M_\odot$, the gradients from this work using the intrinsic abundances are much steeper at $M_\star \lesssim 10^{10.25} M_\odot$ than those listed in Hemler et al. (2021). Reasons for this difference may include, among others: (i) the metallicities of each individual spaxel are calculated differently, (ii) different regions are fitted, (iii) the spaxels used for measuring the gradients are selected using different criteria, and (iv) different galaxy populations are considered.

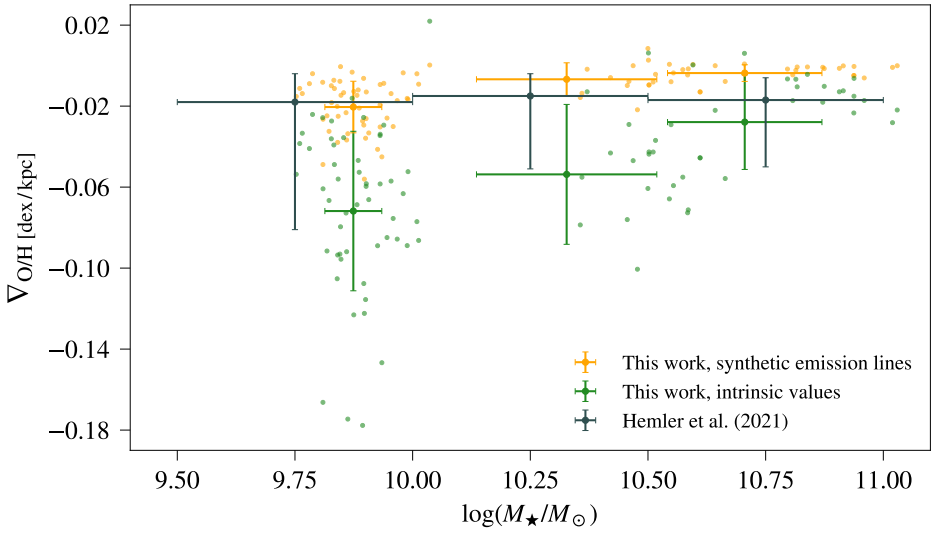

Figure 3.9: Slope of metallicity gradients in units of [dex/kpc] versus stellar mass. The dark grey error bars are values adopted from Hemler et al. (2021), and show peak and spread of log-normal fits to the gradient distributions of 0.25 dex mass bins centered at 9.75, 10.25, and 10.75 for IllustrisTNG50 galaxies. The orange (green) dots are gradients derived in this work from synthetic emission lines (intrinsic abundances) of IllustrisTNG50 and TNG100 galaxies, and the orange (green) error bars are $\mu \pm \sigma$ of stellar mass bins with edges equal to those of Hemler et al. (2021).

Figure 3.10 compare the total metallicities and metallicity gradients of galaxies with stellar mass $M_\star \leqslant 10^9 M_\odot$ derived in this work from the synthetic emission lines, to values of 122 spiral galaxies from the CALIFA survey measured by Sánchez-Menguiano et al. (2016). They estimated metallicities of SF spaxels using the O3N2 calibration from Marino et al. (2013), and the gradients were measured in the region $0.5 - 2.0 R_{\rm e}$. While the calibration used here to estimate metallicity is different from the one used in Sánchez-Menguiano et al. (2016), the overall trends can still be compared. Contrary to what our results show, Sánchez-Menguiano et al. (2016) found no relation between stellar mass and metallicity gradient. Specifically, they report a characteristic slope for their sample of $\alpha_{\rm O/H} = -0.075$ dex/$R_{\rm e}$ with a scatter of $\sigma = 0.016$ dex/$R_{\rm e}$, independent of the integrated stellar mass of the galaxies. Additionally, they find no dependencies of $\nabla_{\rm O/H}$ on morphology, absolute magnitude, and the presence or absence

of bars, similar to previous results (e.g. Sánchez et al., 2012; Sánchez et al., 2014a). The galaxy sample studied in Sánchez-Menguiano et al. (2016) is comprised of face-on spiral galaxies with morphological types between Sa and Sm, including barred galaxies, with no evident signatures of interaction or merging. Their sample is thus more constrained than ours, as we have not based the selection on morphological type. The relation between stellar mass and metallicity gradient evident in our results, with more massive galaxies exhibiting shallower gradients, may thus be a reflection of the variety of galaxies in our sample. Sánchez et al. (2014a) found a weak trend toward slightly flatter gradients for galaxies with $M_\star > 4.5 \times 10^{10} M_\odot$, but note that this result should be interpreted with care, as some of these galaxies only have few H II regions and/or a less clearly defined disc.

However, as seen in figure 3.10, our results are overall consistent with those of Sánchez-Menguiano et al. (2016). Specifically, a good agreement is found for the MMR, despite the use of different calibrations. Most of the total metallicities from our work lie within the $\mu \pm \sigma$ of 0.2 dex stellar mass bins of the CALIFA sample (right panel of figure 3.10), with an average RMSE of 0.026 (for all stellar mass bins).

Our derived gradients (left panel of figure 3.10) on the other hand are generally flatter, especially at $M_\star \gtrsim 10^{10.6} M_\odot$. This may be due to both the metallicity estimation as well as the range in which we choose to measure the gradients. The latter may in particular contribute to the discrepancy; Sánchez-Menguiano et al. (2016) specifically fitted the region $0.5 \leqslant R/R_e \leqslant 2.0$, as they observed at nearly flat distribution or even a drop at $< 0.5 R_e$, and a flattening at $> 2.0 R_e$. A flattening of the central and exterior regions is also observed in some of the more massive galaxies of our sample (see e.g. figure 2.16). While we intentionally excluded the exterior region for galaxies where an outer truncation was present, the flattening of the inner region was included in the fit (see section 2.2.5). This may have contributed to the flattened gradients of the most massive galaxies of our sample. Indeed, a better agreement is found between our sample and CALIFA for galaxies with $M_\star < 10^{10.6} M_\odot$, and is virtually independent on whether the comparison is based on the mean ($\mathrm{RMSE}_\mu = 0.052$) or the reported characteristic slope ($\mathrm{RMSE}_\alpha = 0.047$). On the other hand, our gradients derived for the most massive galaxies ($M_\star \gtrsim 10^{10.6} M_\odot$) were more comparable to the mean value ($\mathrm{RMSE}_\mu = 0.047$) than to $\alpha_{\mathrm{O/H}}$ ($\mathrm{RMSE}_\alpha = 0.061$).

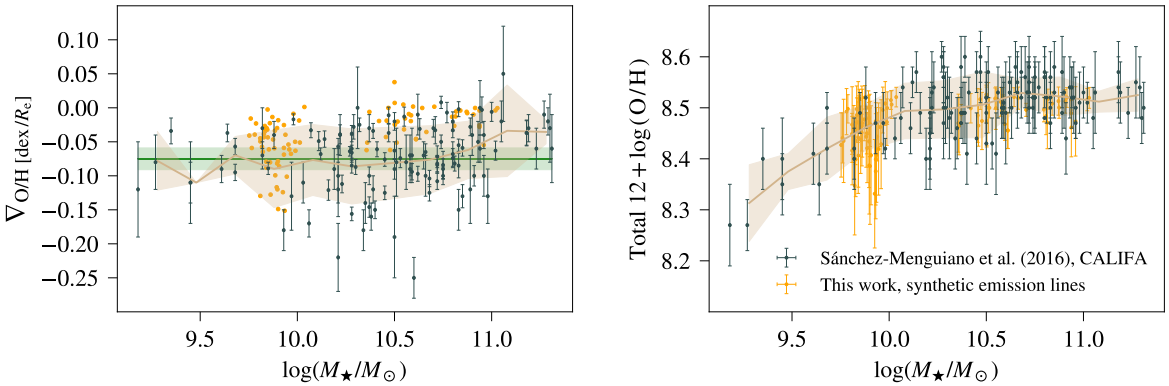

Figure 3.10: Slope of metallicity gradient in units of [dex/R_e] (left) and total metallicity (right) versus stellar mass. The orange dots show results from this work, with metallicities derived from synthetic emission lines of IllustrisTNG50 and TNG100 galaxies using PG16. The dark grey error bars are values for 122 CALIFA spiral galaxies adopted from Sánchez-Menguiano et al. (2016). Corresponding $\mu \pm \sigma$ of 0.2 dex bins in stellar mass of values from this sample are indicated in each panel by a tan line and shaded area. The green line and shaded area in the left panel is the characteristic slope $\alpha_{\mathrm{O/H}} = -0.075$ dex/R_e and corresponding scatter $\sigma = 0.016$ dex/R_e reported by Sánchez-Menguiano et al. (2016).

Chapter 4

Summary and Conclusion

The gas-phase metallicity- and ionization parameter were estimated for six nearby galaxies observed with integral field spectroscopy using the calibrations of Pilyugin and Grebel (2016) and Dors et al. (2016), respectively. Negative metallicity gradients were derived for the four spiral galaxies NGC 925, NGC 5194, NGC 6946 and NGC 7331 and the dwarf irregular galaxy NGC 4214, while a flat metallicity gradient was measured for NGC 1569.

Synthetic, spatially resolved optical emission lines were generated using emission line models (Hirschmann et al., 2017) for a sample of simulated IllustrisTNG galaxies. The simulated galaxies were selected based on similarity to the observed ones in stellar mass, gas mass and SFR. Gas-phase metallicity and ionization parameter gradients of simulated galaxies were derived both from the synthetic optical emission lines and the intrinsic simulation values. Metallicity and ionization parameter were estimated from the synthetic emission lines with the same calibrations used for the observations, allowing for the first time a fair comparison of observed and simulated metallicities and metallicity gradients.
While both the synthetic emission lines and the intrinsic simulation abundances were able to reproduce the observed metallicity gradients, the use of line ratios from the emission line models proved to be a great improvement to the intrinsic simulations. Specifically, both the normalization and slope of the derived metallicity gradients, as well as the total metallicities, are found to be comparable to the observed ones when selected simulated galaxies based on similarity in stellar mass, gas mass and SFR. On the other hand, the intrinsically predicted values from the simulations overestimate the normalization and produce much steeper gradients. Both the intrinsic- and synthetic ionization gradients exhibit large deviations from the observed ones compared to the metallicity gradients.

The simulations presented relations between O/H and strong line ratios comparable to those seen in observations, but a larger discrepancy was found when considering log(U) versus the strong line ratios. This discrepancy may on one hand be due to a simplified modelling in the simulations, or on the other hand arise from biases in the strong line-ratio calibrations adopted in the observations. Some of the main caveats of the simulations and emission line modelling needing to be addressed in future work, to allow for a more reliable comparison to observations, include (i) uncertain sub-resolution models, (ii) not resolving the structure of the ISM such as individual H II regions, (iii) assumptions in the arrangement of H II regions, and (iv) modelling of the ionisation parameter.

The main results of our analysis are that:

- The observational metallicity gradients agree with the general tendencies from the literature, in the sense that flatter gradients are found for low-mass galaxies ($M_\star \approx 10^8 M_\odot$) and the most massive systems ($M_\star \gtrsim 10^{10.5} M_\odot$), while the other exhibit negative slopes.

- Integrated metallicity and ionization parameter, along with corresponding radial profiles, were derived for a sample of simulated galaxies from IllustrisTNG50-1 and IllustrisTNG100-1, selected based on similarity to the observed galaxies in stellar mass, gas mass and SFR.
- Spatially resolved synthetic emission line maps were generated for the simulated galaxies using emission line models, allowing for the first time an accurate confrontation of observed galaxies and galaxies from cosmological, hydrodynamical simulations.
- The integrated metallicities derived from both the synthetic emission lines and the intrinsic simulation abundances are in agreement with observed trends, such as the mass-metallicity relation, as well as the presence of shallow metallicity gradients in low- and high-mass systems, and negative gradients in intermediate-mass galaxies.
- The synthetic emission lines are in much better agreement to observations than the intrinsic simulation values for both the total metallicity and ionization parameter, as well as the radial gradients of these parameters. Albeit, a much larger scatter was present for the ionization parameter than the metallicities.

In addition, the main physical mechanisms found to shape the gas metallicity gradients in the simulated galaxies are summarised below.

- At low masses ($M_\star < 9.5 M_\odot$), simulated galaxies with steep negative gradients tend to have lower total metallicity at the same SFR or sSFR compared to galaxies with shallower gradients, and likewise exhibit lower total metallicity at the same R_e.
- At intermediate masses ($9.5 < M_\star/M_\odot < 10.1$), no clear relations with the metallicity gradient were present. However, at similar total metallicity, negative gradients are often associated with higher AGN activity.
- At high masses ($M_\star > 10.1 M_\odot$), steeper negative metallicity gradients are most often present in galaxies with either (i) higher black hole accretion rate and low total metallicity in conjunction with intermediate to high values of SFR and sSFR, or (ii) lower disc scale-length (R_e) at similar values of SFR.
- Simulated galaxies that experienced more mergers after $z = 3.0$ exhibit flatter gradients and higher total metallicities, with major mergers having the largest impact. In particular, galaxies that experienced more recent merger events have shallower gradients than galaxies with mergers at earlier times.
- Variations in the cosmic evolution of the metallicity gradient is mainly governed by the merger history and feedback from AGN and starbursts. The shape of the metallicity gradient is moreover found to gradually flatten over time.

Bibliography

(Sept. 2016). In: *Astronomy & Astrophysics* 594, A13. DOI: 10.1051/0004-6361/201525830.

Afflerbach, Churchwell, and Werner (Mar. 1997). In: *The Astrophysical Journal* 478.1, pp. 190–205. DOI: 10.1086/303771.

Asari et al. (Oct. 2007). In: *Monthly Notices of the Royal Astronomical Society* 381.1, pp. 263–279. DOI: 10.1111/j.1365-2966.2007.12255.x.

Athanassoula (Nov. 1992). In: *Monthly Notices of the Royal Astronomical Society* 259.2, pp. 345–364. DOI: 10.1093/mnras/259.2.345.

Baldwin, Phillips, and Terlevich (Feb. 1981). In: *Publications of the Astronomical Society of the Pacific* 93, pp. 5–19. DOI: 10.1086/130766.

Belfiore et al. (May 2016). In: *Monthly Notices of the Royal Astronomical Society* 487.1, pp. 456–474. DOI: 10.1093/mnras/stz1165.

Belfiore et al. (Apr. 2017). In: *Monthly Notices of the Royal Astronomical Society* 469.1, pp. 151–170. DOI: 10.1093/mnras/stx789.

Bilitewski and Schönrich (Oct. 2012). In: *Monthly Notices of the Royal Astronomical Society* 426.3, pp. 2266–2282. DOI: 10.1111/j.1365-2966.2012.21827.x.

Boissier and Prantzos (Aug. 1999). In: *Monthly Notices of the Royal Astronomical Society* 307.4, pp. 857–876. DOI: 10.1046/j.1365-8711.1999.02699.x.

Bresolin (July 2019). In: *Monthly Notices of the Royal Astronomical Society* 488.3, pp. 3826–3843. DOI: 10.1093/mnras/stz1947.

Bresolin et al. (Sept. 2005). In: *Astronomy & Astrophysics* 441.3, pp. 981–997. DOI: 10.1051/0004-6361:20053369.

Bresolin et al. (Mar. 2009a). In: *The Astrophysical Journal* 695.1, pp. 580–595. DOI: 10.1088/0004-637x/695/1/580.

Bresolin et al. (July 2009b). In: *The Astrophysical Journal* 700.1, pp. 309–330. DOI: 10.1088/0004-637x/700/1/309.

Bruzual and Charlot (Oct. 2003). In: *Monthly Notices of the Royal Astronomical Society* 344.4, pp. 1000–1028. DOI: 10.1046/j.1365-8711.2003.06897.x.

Cairós et al. (Oct. 2012). In: *Astronomy & Astrophysics* 547, A24. DOI: 10.1051/0004-6361/201219598.

Calura et al. (July 2009). In: *Astronomy & Astrophysics* 504.2, pp. 373–388. DOI: 10.1051/0004-6361/200911756.

Cardelli, Clayton, and Mathis (1989). In: *The Astrophysical journal* 345, p. 245. DOI: 10.1086/167900.

Carton, David et al. (Mar. 2017). In: *Monthly Notices of the Royal Astronomical Society* 468.2, pp. 2140–2163. DOI: 10.1093/mnras/stx545.

Cavichia et al. (Dec. 2013). In: *Monthly Notices of the Royal Astronomical Society* 437.4, pp. 3688–3701. DOI: 10.1093/mnras/stt2164.

Cedrés et al. (Sept. 2012). In: *Astronomy & Astrophysics* 545, A43. DOI: 10.1051/0004-6361/201219571.

Chabrier (July 2003). In: *Publications of the Astronomical Society of the Pacific* 115.809, pp. 763–795. DOI: 10.1086/376392.

Charlot and Longhetti (May 2001). In: *Monthly Notices of the Royal Astronomical Society* 323.4, pp. 887–903. DOI: 10.1046/j.1365-8711.2001.04260.x.

Cheung et al. (June 2015). In: *The Astrophysical Journal* 807.1, p. 36. DOI: 10.1088/0004-637x/807/1/36.

Chiappini, Matteucci, and Romano (June 2001). In: *The Astrophysical Journal* 554.2, pp. 1044–1058. DOI: 10.1086/321427.

Christensen-Dalsgaard (Mar. 2008). *Lecture Notes on Stellar Structure and Evolution.*

Churchill (2010). *Lecture Notes in the Interstellar Medium.* URL: http://astronomy.nmsu.edu/cwc/Teaching/ASTR605/.

Collacchioni et al. (Jan. 2020). In: *Monthly Notices of the Royal Astronomical Society* 495.3, pp. 2827–2843. DOI: 10.1093/mnras/staa1334.

Curti et al. (Nov. 2019). In: *Monthly Notices of the Royal Astronomical Society* 491.1, pp. 944–964. DOI: 10.1093/mnras/stz2910.

Data Specifications, Illustris TNG. URL: https://www.tng-project.org/data/docs/specifications/#sec1.

Data Visualization, Illustris TNG. URL: https://www.tng-project.org/data/vis/.

Deharveng et al. (Jan. 2000). In: *Monthly Notices of the Royal Astronomical Society* 311.2, pp. 329–345. DOI: 10.1046/j.1365-8711.2000.03030.x.

Delgado, González et al. (Feb. 2014). In: *Astronomy & Astrophysics* 562, A47. DOI: 10.1051/0004-6361/201322011.

Delgado, González et al. (Sept. 2015). In: *Astronomy & Astrophysics* 581, A103. DOI: 10.1051/0004-6361/201525938.

Dembinski et al. (2021). DOI: 10.5281/ZENODO.3949207.

Dopita et al. (Oct. 2000). In: *The Astrophysical Journal* 542.1, pp. 224–234. DOI: 10.1086/309538.

Dopita et al. (Aug. 2006). In: *The Astrophysical Journal* 647.1, pp. 244–255. DOI: 10.1086/505418.

Dors et al. (Dec. 2016). In: *Monthly Notices of the Royal Astronomical Society* 466.1, pp. 726–737. DOI: 10.1093/mnras/stw3115.

Dutil and Roy (May 1999). In: *The Astrophysical Journal* 516.1, pp. 62–76. DOI: 10.1086/307100.

Ellison et al. (Dec. 2007). In: *The Astrophysical Journal* 672.2, pp. L107–L110. DOI: 10.1086/527296.

FAQ, Illustris TNG. URL: https://www.tng-project.org/data/docs/faq/#gen5.

Feltre, Charlot, and Gutkin (Jan. 2016). In: *Monthly Notices of the Royal Astronomical Society* 456.3, pp. 3354–3374. DOI: 10.1093/mnras/stv2794.

Ferguson and Clarke (Aug. 2001). In: *Monthly Notices of the Royal Astronomical Society* 325.2, pp. 781–791. DOI: 10.1046/j.1365-8711.2001.04501.x.

Ferland et al. (Apr. 2013). In: *Revista Mexicana de Astronomía y Astrofísica* 49, pp. 137–163.

Fernandes et al. (Apr. 2005). In: *Monthly Notices of the Royal Astronomical Society* 358.2, pp. 363–378. DOI: 10.1111/j.1365-2966.2005.08752.x.

Friedli (Jan. 1998). In: *Abundance Profiles: Diagnostic Tools for Galaxy History*. Ed. by Friedli et al. Vol. 147. Astronomical Society of the Pacific Conference Series, p. 287.

Friedli and Benz (Sept. 1995). In: *Astronomy & Astrophysics* 301, p. 649.

Friedli, Benz, and Kennicutt (Aug. 1994). In: *The Astrophysical Journal* 430, p. L105. DOI: 10.1086/187449.

Fu et al. (Apr. 2009). In: *The Astrophysical Journal* 696.1, pp. 668–675. DOI: 10.1088/0004-637x/696/1/668.

Fu et al. (July 2013). In: *Monthly Notices of the Royal Astronomical Society* 434.2, pp. 1531–1548. DOI: 10.1093/mnras/stt1117.

Genzel et al. (Oct. 2014). In: *The Astrophysical Journal* 796.1, p. 7. DOI: 10.1088/0004-637x/796/1/7.

Goetz and Koeppen (Sept. 1992). In: *Astronomy and Astrophysics* 262.2, pp. 455–467.

Gutkin, Charlot, and Bruzual (July 2016). In: *Monthly Notices of the Royal Astronomical Society* 462.2, pp. 1757–1774. DOI: 10.1093/mnras/stw1716.

Harlan J. Smith Telescope (Mar. 2020). URL: https://mcdonaldobservatory.org/research/telescopes/HJSmith.

Harrison (2014). PhD thesis. Durham University.

Hayden et al. (Apr. 2014). In: *The Astronomical Journal* 147.5, p. 116. DOI: 10.1088/0004-6256/147/5/116.

Heckman (1980). In: *Astronomy & Astrophysics* 500, pp. 187–199.

Hemler et al. (June 2021). In: *Monthly Notices of the Royal Astronomical Society* 506.2, pp. 3024–3048. DOI: 10.1093/mnras/stab1803.

Hill et al. (2008). In: vol. 7014. SPIE, pp. 2408–2422. DOI: 10.1117/12.790235.

Hirschmann et al. (Aug. 2017). In: *Monthly Notices of the Royal Astronomical Society* 472.2, pp. 2468–2495. DOI: 10.1093/mnras/stx2180.

Hirschmann et al. (May 2019). In: *Monthly Notices of the Royal Astronomical Society* 487.1, pp. 333–353. DOI: 10.1093/mnras/stz1256.

Ho, Filippenko, and Sargent (Oct. 1997). In: *The Astrophysical Journal* 487.2, pp. 568–578. DOI: 10.1086/304638.

Hou, Prantzos, and Boissier (Oct. 2000). In: *Astronomy & Astrophysics* 362, pp. 921–936.

IRAF: calibrate (Mar. 1993). URL: https://iraf.net/irafhelp.php?val=calibrate&help=Help+Page.

IRAF: sensfunc (Mar. 1993). URL: http://iraf.noao.edu/scripts/irafhelp?sensfunc.

IRAF: standard (Jan. 2000). URL: http://iraf.noao.edu/scripts/irafhelp?standard.

Kaplan et al. (June 2016). In: *Monthly Notices of the Royal Astronomical Society* 462.2, pp. 1642–1682. DOI: 10.1093/mnras/stw1422.

Karachentsev et al. (Apr. 2004). In: *The Astronomical Journal* 127.4, pp. 2031–2068. DOI: 10.1086/382905.

Kauffmann et al. (Dec. 2003). In: *Monthly Notices of the Royal Astronomical Society* 346.4, pp. 1055–1077. DOI: 10.1111/j.1365-2966.2003.07154.x.

Kewley and Dopita (Sept. 2002). In: *The Astrophysical Journal Supplement Series* 142.1, pp. 35–52. DOI: 10.1086/341326.

Kewley et al. (July 2001). In: *The Astrophysical Journal* 556.1, pp. 121–140. DOI: 10.1086/321545.

Kewley et al. (Nov. 2006). In: *Monthly Notices of the Royal Astronomical Society* 372.3, pp. 961–976. DOI: 10.1111/j.1365-2966.2006.10859.x.

Kewley et al. (Aug. 2010). In: *The Astrophysical Journal* 721.1, pp. L48–L52. DOI: 10.1088/2041-8205/721/1/l48.

Kewley et al. (Aug. 2013). In: *The Astrophysical Journal* 774.2, p. 100. DOI: 10.1088/0004-637x/774/2/100.

Kobayashi (Jan. 2004). In: *Monthly Notices of the Royal Astronomical Society* 347.3, pp. 740–758. DOI: 10.1111/j.1365-2966.2004.07258.x.

Kobulnicky and Kewley (Dec. 2004). In: *The Astrophysical Journal* 617.1, pp. 240–261. DOI: 10.1086/425299.

Kreckel et al. (Dec. 2019). In: *The Astrophysical Journal* 887.1, p. 80. DOI: 10.3847/1538-4357/ab5115.

Lacey and Fall (Mar. 1985). In: *The Astrophysical Journal* 290, p. 154. DOI: 10.1086/162970.

Lara-López et al. (Oct. 2010). In: *Astronomy & Astrophysics* 521, p. L53. DOI: 10.1051/0004-6361/201014803.

Lara-López et al. (Jan. 2021). In: *The Astrophysical Journal* 906.1, p. 42. DOI: 10.3847/1538-4357/abc892.

Larson and Tinsley (Jan. 1978). In: *The Astrophysical Journal* 219, p. 46. DOI: 10.1086/155753.

Leaman et al. (2014). In: *Memorie della Societa Astronomica Italiana* 85, p. 504.

Lee, Skillman, and Venn (Feb. 2005). In: *The Astrophysical journal* 620.1, pp. 223–237. DOI: 10.1086/427019.

Lee et al. (Aug. 2006). In: *The Astrophysical Journal* 647.2, pp. 970–983. DOI: 10.1086/505573.

Léna et al. (2012). *Observational Astrophysics*. Springer Berlin Heidelberg. DOI: 10.1007/978-3-642-21815-6.

Lequeux et al. (Dec. 1979). In: *Astronomy & Astrophysics* 80, p. 155.

Lian, Thomas, and Maraston (Sept. 2018). In: *Monthly Notices of the Royal Astronomical Society*. DOI: 10.1093/mnras/sty2506.

López-Sánchez (Dec. 2006). PhD Thesis. PhD thesis. La Laguna University.

Ma et al. (Dec. 2015). In: *Monthly Notices of the Royal Astronomical Society* 456.2, pp. 2140–2156. DOI: 10.1093/mnras/stv2659.

Ma et al. (Jan. 2017). In: *Monthly Notices of the Royal Astronomical Society*, stx034. DOI: 10.1093/mnras/stx034.

Maiolino et al. (July 2008). In: *Astronomy & Astrophysics* 488.2, pp. 463–479. DOI: 10.1051/0004-6361:200809678.

Mannucci et al. (Sept. 2010). In: *Monthly Notices of the Royal Astronomical Society* 408.4, pp. 2115–2127. DOI: 10.1111/j.1365-2966.2010.17291.x.

Marino et al. (July 2012). In: *The Astrophysical Journal* 754.1, p. 61. DOI: 10.1088/0004-637x/754/1/61.

Marino et al. (Nov. 2013). In: *Astronomy & Astrophysics* 559, A114. DOI: 10.1051/0004-6361/201321956.

Martin and Roy (May 1995). In: *The Astrophysical Journal* 445, p. 161. DOI: 10.1086/175682.

Mateus et al. (Aug. 2006). In: *Monthly Notices of the Royal Astronomical Society* 370.2, pp. 721–737. DOI: 10.1111/j.1365-2966.2006.10565.x.

Matteucci and François (Aug. 1989). In: *Monthly Notices of the Royal Astronomical Society* 239.3, pp. 885–904. DOI: 10.1093/mnras/239.3.885.

Michelsen and Petersen (2018). Chi-Square minimisation with iMinuit, Course material from "Applied Statistics: From Data to Results". URL: https://github.com/AppliedStatisticsNBI/AppStat2020/blob/main/Week1/original/ChiSquareTest/ChiSquareTest_original.ipynb.

Mingozzi et al. (Apr. 2020). In: *Astronomy & Astrophysics* 636, A42. DOI: 10.1051/0004-6361/201937203.

Mitchell Spectrograph (Mar. 2020). URL: https://mcdonaldobservatory.org/research/instruments/mitchell-spectrograph.

Mo, Bosch, and White (2010). *Galaxy Formation and Evolution*. Cambridge University Press. ISBN: 978-0-511-72962-1.

Moustakas (2006). PhD Thesis. PhD thesis. University of Arizona.

Moustakas et al. (Sept. 2010). In: *The Astrophysical Journal Supplement Series* 190.2, pp. 233–266. DOI: 10.1088/0067-0049/190/2/233.

Narlikar (Nov. 1995). *From Black Clouds to Black Holes*. World Scientific. DOI: 10.1142/2541.

Newman et al. (Nov. 2012). In: *The Astrophysical Journal* 761.1, p. 43. DOI: 10.1088/0004-637x/761/1/43.

Osterbrock and Ferland (2006). *Astrophysics of Gaseous Nebulae and Active Galactic Nuclei*. 2nd ed. University Science Books. ISBN: 1891389343.

P3D (Mar. 2020). URL: https://p3d.sourceforge.io/index.php?page=about.

Panuzzo et al. (Oct. 2003). In: *Astronomy & Astrophysics* 409.1, pp. 99–114. DOI: 10.1051/0004-6361:20031094.

Peimbert (Dec. 1967). In: *The Astrophysical Journal* 150, p. 825. DOI: 10.1086/149385.

Peimbert (June 1979). In: *IAU Symposium* 84, p. 307.

Perez, Michel-Dansac, and Tissera (Aug. 2011). In: *Monthly Notices of the Royal Astronomical Society* 417.1, pp. 580–590. DOI: 10.1111/j.1365-2966.2011.19300.x.

Pérez et al. (Jan. 2013). In: *The Astrophysical Journal* 764.1, p. L1. DOI: 10.1088/2041-8205/764/1/l1.

Pérez-Montero et al. (Oct. 2016). In: *Astronomy & Astrophysics* 595, A62. DOI: 10.1051/0004-6361/201628601.

Peters and Hirschi (2013). "The Evolution of High-Mass Stars". In: *Planets, Stars and Stellar Systems*. Springer Netherlands, pp. 447–484. DOI: 10.1007/978-94-007-5615-1_9.

Pillepich et al. (Oct. 2017). In: *Monthly Notices of the Royal Astronomical Society* 473.3, pp. 4077–4106. DOI: 10.1093/mnras/stx2656.

Pilyugin (Aug. 2000). In: *Astronomy & Astrophysics* 362, pp. 325–332.

— (Apr. 2001). In: *Astronomy & Astrophysics* 369.2, pp. 594–604. DOI: 10.1051/0004-6361:20010079.

Pilyugin and Grebel (Jan. 2016). In: *Monthly Notices of the Royal Astronomical Society* 457.4, pp. 3678–3692. DOI: 10.1093/mnras/stw238.

Pilyugin and Thuan (Sept. 2005). In: *The Astrophysical Journal* 631.1, pp. 231–243. DOI: 10.1086/432408.

Pisano and Wilcots (Mar. 1998). In: *The Astronomical Journal* 115, pp. 975–999.

Poetrodjojo et al. (July 2018). In: *Monthly Notices of the Royal Astronomical Society* 479.4, pp. 5235–5265. DOI: 10.1093/mnras/sty1782.

Portinari and Chiosi (Oct. 1999). In: *Astronomy & Astrophysics* 350, pp. 827–839.

— (Mar. 2000). In: *Astronomy & Astrophysics* 355, pp. 929–948.

Prantzos and Boissier (Apr. 2000). In: *Monthly Notices of the Royal Astronomical Society* 313.2, pp. 338–346. DOI: 10.1046/j.1365-8711.2000.03228.x.

Price-Whelan et al. (2018). In: *The Astronomical Journal* 156.3, p. 123.

Python Software Foundation, Version 2.7 (Mar. 2020). URL: http://www.python.org.

Rich et al. (June 2012). In: *The Astrophysical Journal* 753.1, p. 5. DOI: 10.1088/0004-637x/753/1/5.

Rodriguez-Gomez et al. (Mar. 2015). In: *Monthly Notices of the Royal Astronomical Society* 449.1, pp. 49–64. DOI: 10.1093/mnras/stv264.

Rosales-Ortega et al. (May 2011). In: *Monthly Notices of the Royal Astronomical Society* 415.3, pp. 2439–2474. DOI: 10.1111/j.1365-2966.2011.18870.x.

Ruiz-Lara et al. (Nov. 2015). In: *Monthly Notices of the Royal Astronomical Society: Letters* 456.1, pp. L35–L39. DOI: 10.1093/mnrasl/slv174.

Rupke, Kewley, and Chien (Oct. 2010a). In: *The Astrophysical Journal* 723.2, pp. 1255–1271. DOI: 10.1088/0004-637x/723/2/1255.

Rupke, Kewley, and JBarnes (Feb. 2010b). In: *The Astrophysical Journal* 710.2, pp. L156–L160. DOI: 10.1088/2041-8205/710/2/l156.

Sánchez et al. (Sept. 2010). In: *Monthly Notices of the Royal Astronomical Society* 410.1, pp. 313–340. DOI: 10.1111/j.1365-2966.2010.17444.x.

Sánchez et al. (Sept. 2012). In: *Astronomy & Astrophysics* 546, A2. DOI: 10.1051/0004-6361/201219578.

Sánchez et al. (Mar. 2014a). In: *Astronomy & Astrophysics* 563, A49. DOI: 10.1051/0004-6361/201322343.

Sánchez et al. (Mar. 2014b). In: *Astronomy & Astrophysics* 563, A49. DOI: 10.1051/0004-6361/201322343.

Sánchez-Blázquez et al. (Oct. 2014). In: *Astronomy & Astrophysics* 570, A6. DOI: 10.1051/0004-6361/201423635.

Sánchez-Menguiano et al. (Feb. 2016). In: *Astronomy & Astrophysics* 587, A70. DOI: 10.1051/0004-6361/201527450.

Sánchez-Menguiano et al. (Jan. 2018). In: *Astronomy & Astrophysics* 609, A119. DOI: 10.1051/0004-6361/201731486.

Schneider (2014). *Extragalactic Astronomy and Cosmology: An Introduction*. Springer. ISBN: 9783642540820.

Schönrich and Binney (June 2009). In: *Monthly Notices of the Royal Astronomical Society* 396.1, pp. 203–222. DOI: 10.1111/j.1365-2966.2009.14750.x.

Schroyen et al. (Aug. 2011). In: *Monthly Notices of the Royal Astronomical Society* 416.1, pp. 601–617. DOI: 10.1111/j.1365-2966.2011.19083.x.

Searle (Sept. 1971). In: *The Astrophysical Journal* 168, p. 327. DOI: 10.1086/151090.

Shaver et al. (Sept. 1983). In: *Monthly Notices of the Royal Astronomical Society* 204.1, pp. 53–112. DOI: 10.1093/mnras/204.1.53.

Sillero et al. (Sept. 2017). In: *Monthly Notices of the Royal Astronomical Society* 472.4, pp. 4404–4413. DOI: 10.1093/mnras/stx2265.

Skillman, Kennicutt, and Hodge (Dec. 1989). In: *The Astrophysical Journal* 347, p. 875. DOI: 10.1086/168178.

Spitoni, Matteucci, and Marcon-Uchida (Mar. 2013). In: *Astronomy & Astrophysics* 551, A123. DOI: 10.1051/0004-6361/201220401.

Spitzer (Mar. 1998). *Physical Processes in the Interstellar Medium*. Wiley. ISBN: 978-0471293354.

Springel (Jan. 2010a). In: *Monthly Notices of the Royal Astronomical Society* 401.2, pp. 791–851. DOI: 10.1111/j.1365-2966.2009.15715.x.

— (Jan. 2010b). In: *Monthly Notices of the Royal Astronomical Society* 401.2, pp. 791–851. DOI: 10.1111/j.1365-2966.2009.15715.x.

Springel et al. (Dec. 2001). In: *Monthly Notices of the Royal Astronomical Society* 328.3, pp. 726–750. DOI: 10.1046/j.1365-8711.2001.04912.x.

Stasinska et al. (Sept. 2006). In: *Monthly Notices of the Royal Astronomical Society* 371.2, pp. 972–982. DOI: 10.1111/j.1365-2966.2006.10732.x.

Stott et al. (Aug. 2014). In: *Monthly Notices of the Royal Astronomical Society* 443.3, pp. 2695–2704. DOI: 10.1093/mnras/stu1343.

Taylor and Kobayashi (July 2017). In: *Monthly Notices of the Royal Astronomical Society* 471.4, pp. 3856–3870. DOI: 10.1093/mnras/stx1860.

Teklu et al. (Oct. 2015). In: *The Astrophysical Journal* 812.1, p. 29. DOI: 10.1088/0004-637x/812/1/29.

Tissera et al. (Dec. 2015). In: *Monthly Notices of the Royal Astronomical Society* 456.3, pp. 2982–2992. DOI: 10.1093/mnras/stv2736.

Tissera et al. (Oct. 2018). In: *Monthly Notices of the Royal Astronomical Society* 482.2, pp. 2208–2221. DOI: 10.1093/mnras/sty2817.

Tody (1986). In: vol. 0627. SPIE, pp. 733–748. DOI: 10.1117/12.968154.

Torrey et al. (Jan. 2019). In: *Monthly Notices of the Royal Astronomical Society*. DOI: 10.1093/mnras/stz243.

Tosi (Apr. 1988). In: *Astronomy & Astrophysics* 197.1-2, pp. 47–51.

Tremonti et al. (Oct. 2004). In: *The Astrophysical Journal* 613.2, pp. 898–913. DOI: 10.1086/423264.

Vila-Costas and Edmunds (Nov. 1992). In: *Monthly Notices of the Royal Astronomical Society* 259.1, pp. 121–145. DOI: 10.1093/mnras/259.1.121.

Walter et al. (Nov. 2008). In: *The Astronomical journal* 136.6, 2563–2647. ISSN: 1538-3881. DOI: 10.1088/0004-6256/136/6/2563.

Wuyts et al. (Aug. 2016). In: *The Astrophysical Journal* 827.1, p. 74. DOI: 10.3847/0004-637x/827/1/74.

Zaritsky, Kennicutt, and Huchra (Jan. 1994). In: *The Astrophysical Journal* 420, p. 87. DOI: 10.1086/173544.

Zinchenko et al. (June 2016). In: *Monthly Notices of the Royal Astronomical Society* 462.3, pp. 2715–2733. DOI: 10.1093/mnras/stw1857.

Zinchenko et al. (Dec. 2018). In: *Monthly Notices of the Royal Astronomical Society* 483.2, pp. 1901–1911. DOI: 10.1093/mnras/sty3026.

Appendix A

Constants

NOTATION	VALUE	UNIT	DESCRIPTION
h	0.6774	km/Mpc/s	Reduced Hubble constant
γ	5/3	–	Adiabatic index
k_{B}	1.3807×10^{-16}	$\mathrm{g\,cm^2/s^2/K}$	Boltzmann constant
m_{H}	$1.6605391 \times 10^{-27}$	kg	Hydrogen mass
$M_{\odot}$	1.9884099×10^{30}	kg	Solar mass
$Z_{\odot}$	0.0127	dex	Primordial Solar metallicity
$\mathcal{X}_{\mathrm{H}}$	0.76	–	Hydrogen mass fraction
c_{d}	3.086×10^{21}	cm/kpc	Conversion factor from kpc to cm

Table A.1: Constants and conversion factors. Except otherwise noted, the Boltzmann constant is in CGS units in all calculations.

Appendix B

Hβ Maps and [S II] BPT Diagrams

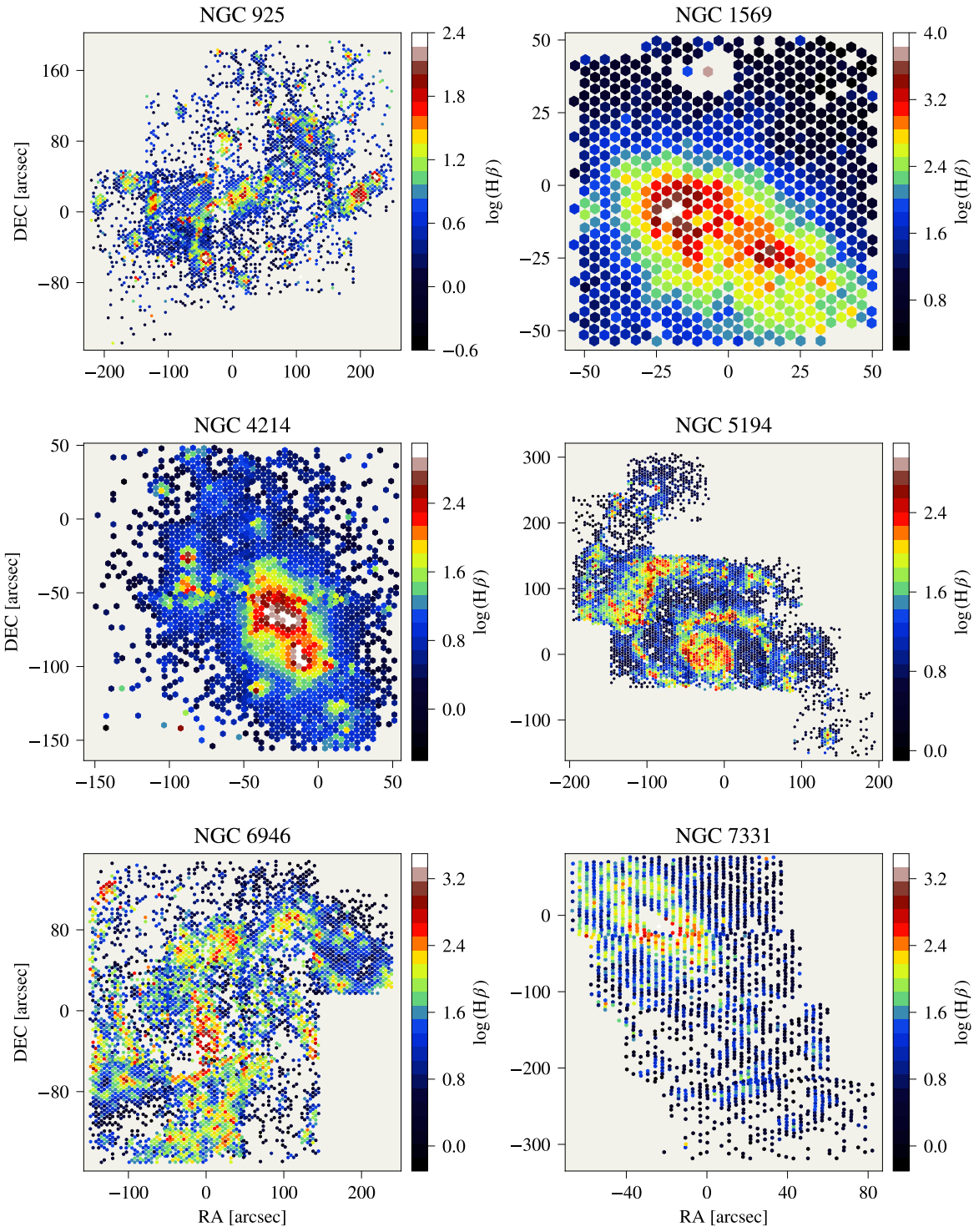

Figure B.1: Extinction corrected Hβ maps for the observed galaxies for spaxels with SNR > 3 in Hα and Hβ.

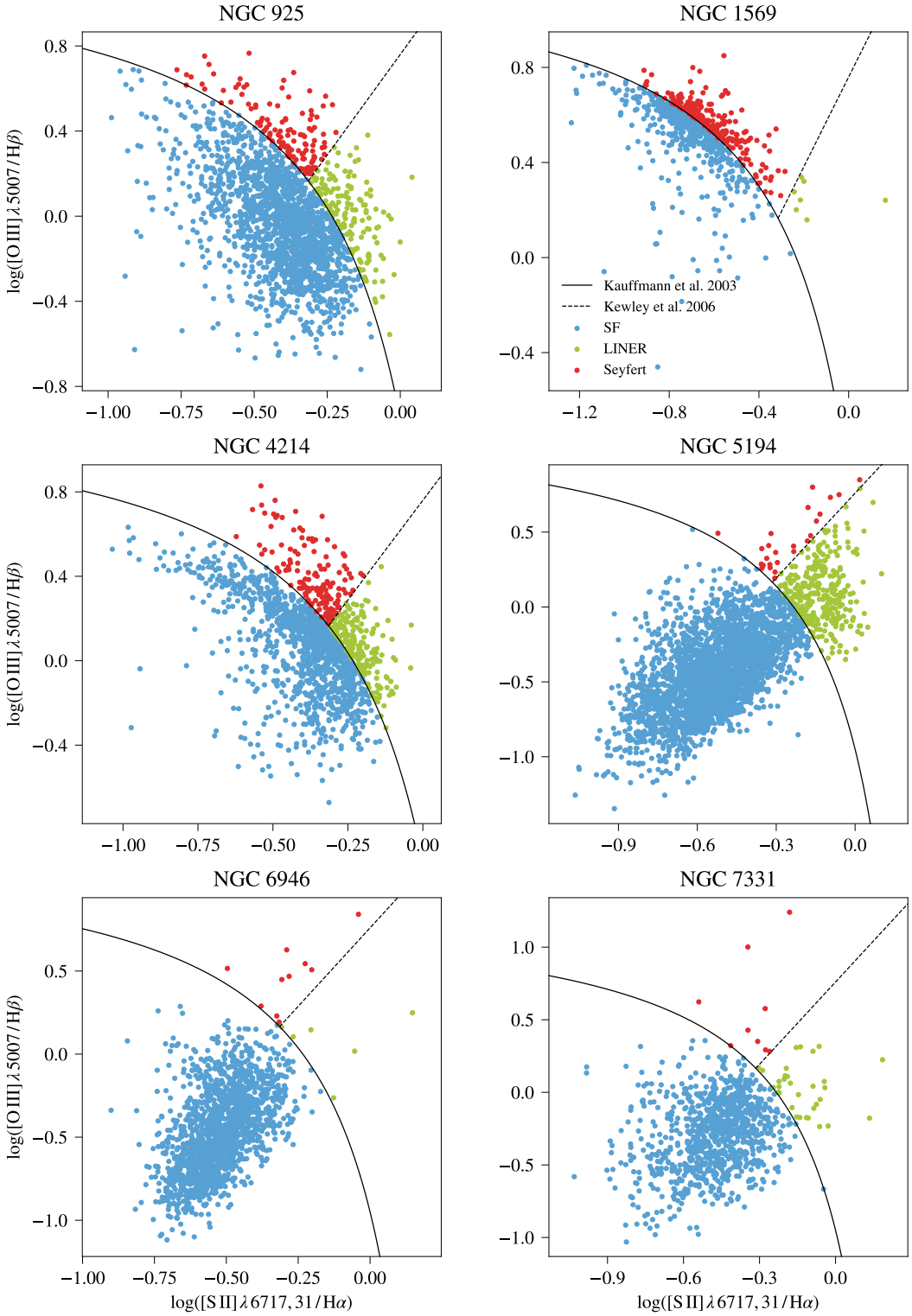

Figure B.2: [S II] BPT diagrams for the observed galaxies, with regions defined in equations (2.15) through (2.24).

Appendix C

Metallicity- and Ionization Gradients

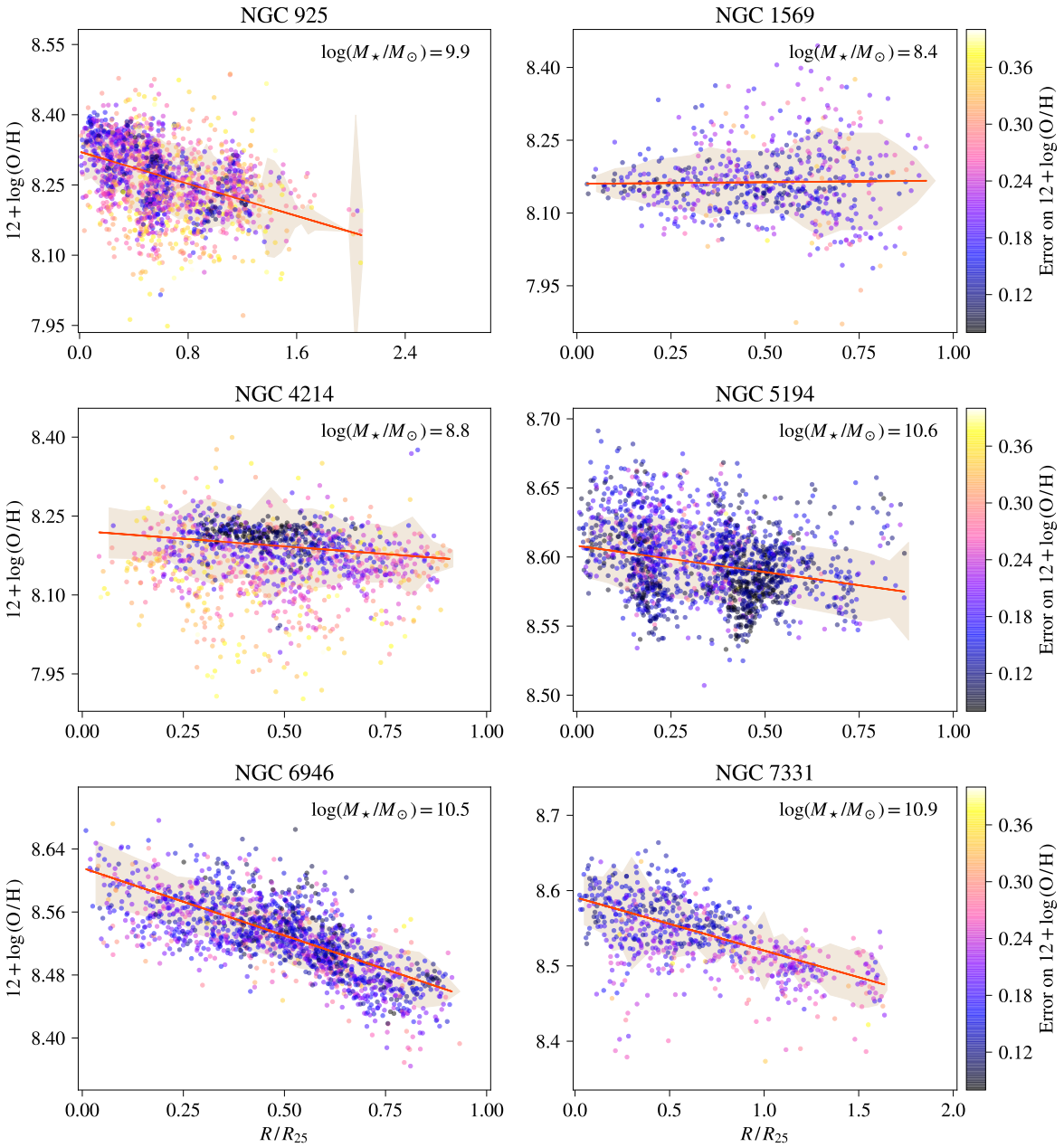

Figure C.1: Metallicity gradients of the observed galaxies in units of [dex/R_{25}]. The red line is a linear χ^2 regression, the dots are color coded by error on the metallicity, and the shaded area is a 1σ scatter. All spaxels are corrected for extinction, filtered by SNR > 3, categorized as starforming from the [N II] diagnostic in section 2.1.4 and 3σ clipped in log(Hα) to remove outliers.

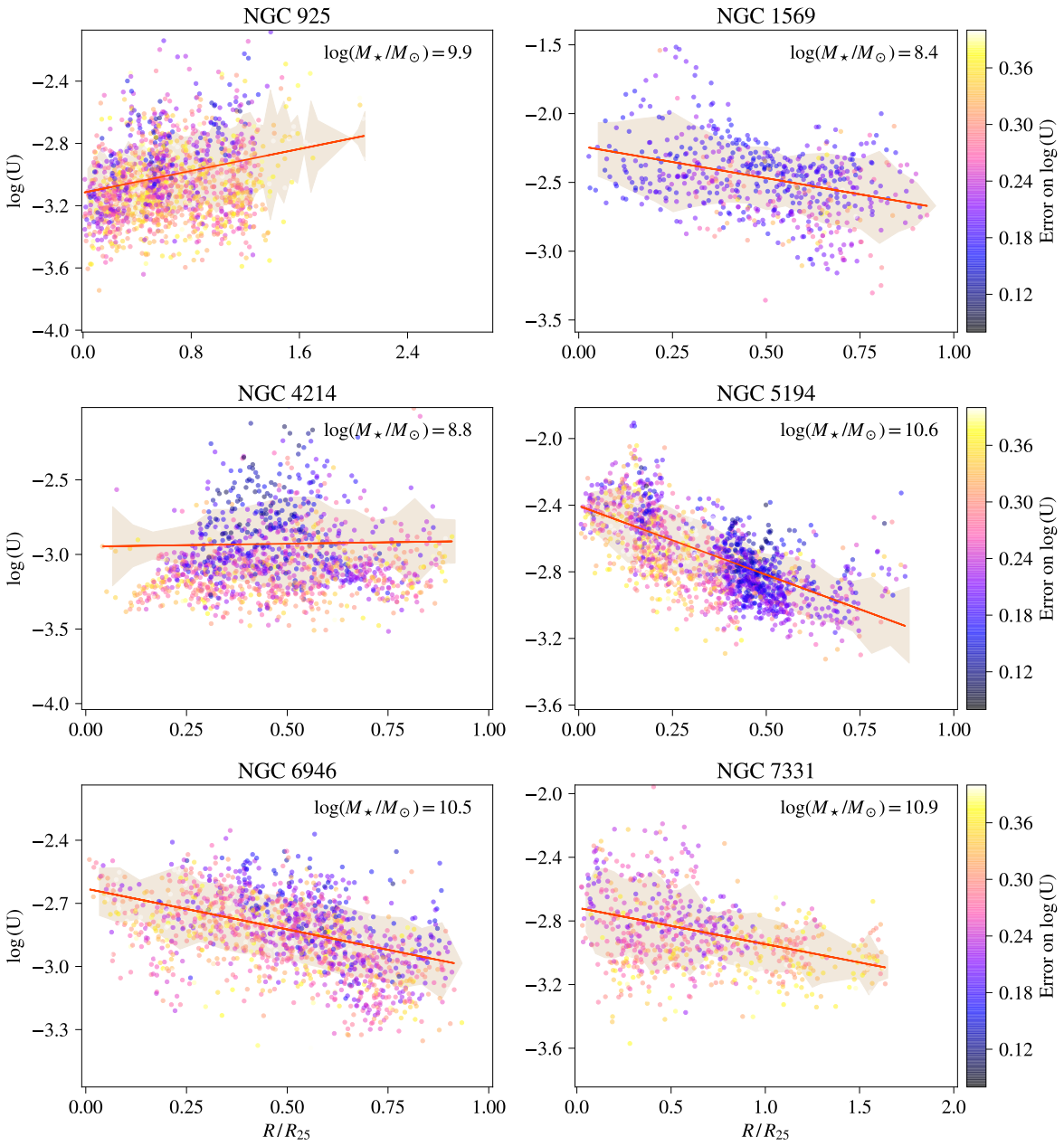

Figure C.2: Ionization gradients of the observed galaxies in units of [dex/R_{25}]. The red line is a linear χ^2 regression, the dots are color coded by error on the ionization parameter, and the shaded area is a 1σ scatter. All spaxels are corrected for extinction, filtered by SNR > 3, categorized as starforming from the [N II] diagnostic in section 2.1.4 and 3σ clipped in log(Hα) to remove outliers.

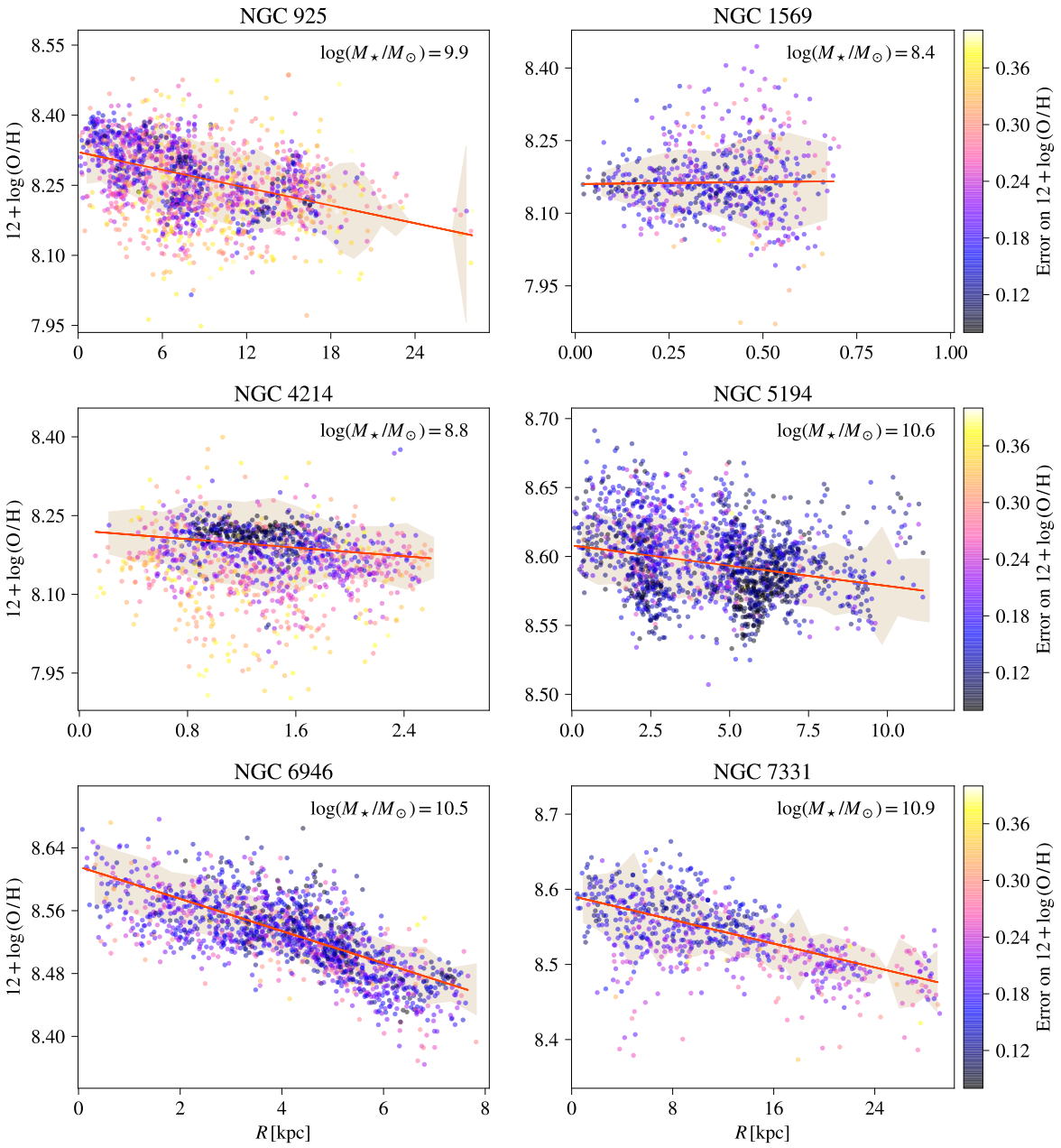

Figure C.3: Metallicity gradients of the observed galaxies in units of [dex/kpc]. The red line is a linear χ^2 regression, the dots are color coded by error on the metallicity, and the shaded area is a 1σ scatter. All spaxels are corrected for extinction, filtered by SNR > 3, categorized as starforming from the [N II] diagnostic in section 2.1.4 and 3σ clipped in log(Hα) to remove outliers.

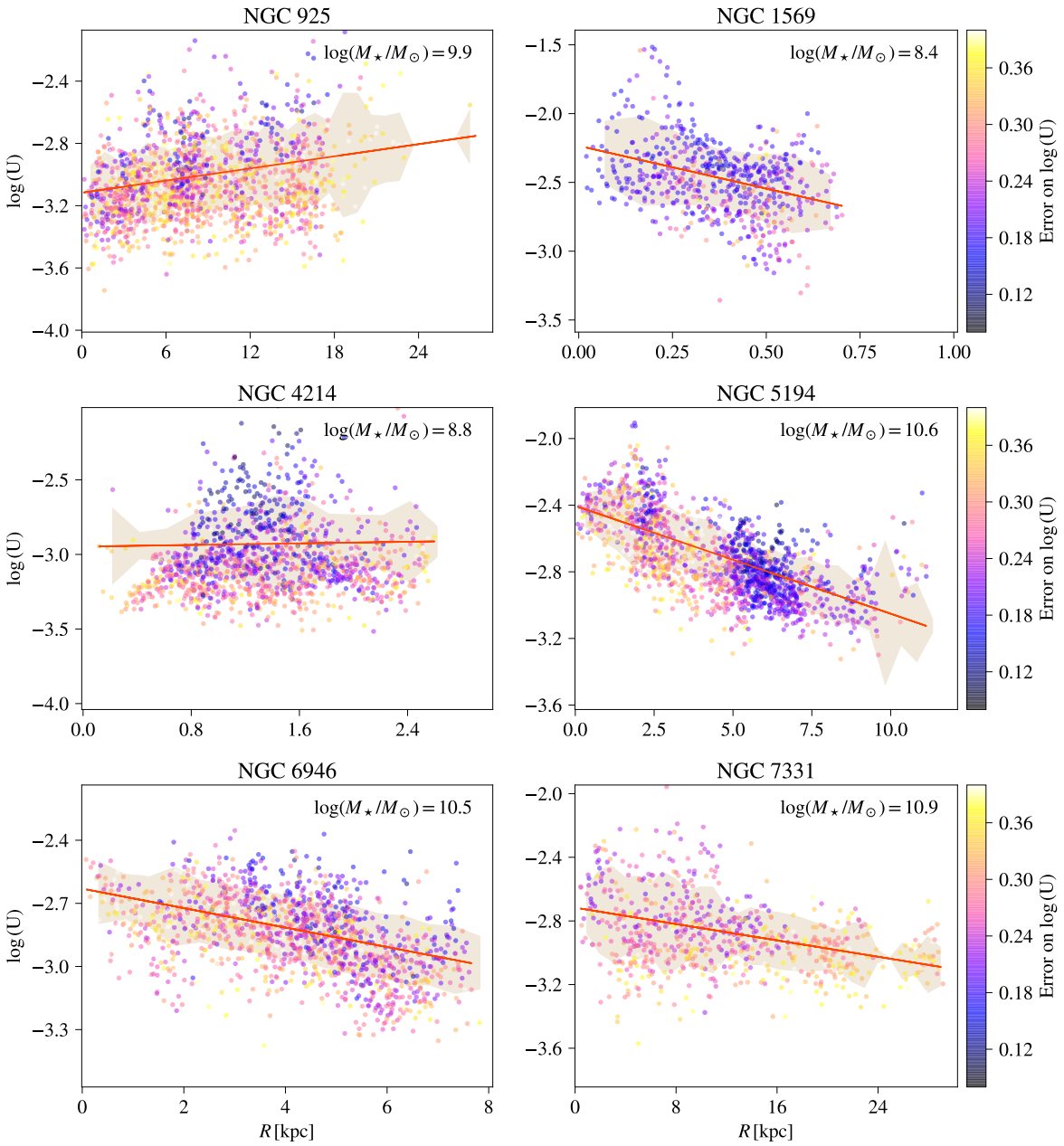

Figure C.4: Ionization gradients of the observed galaxies in units of [dex/kpc]. The red line is a linear χ^2 regression, the dots are color coded by error on the ionization parameter, and the shaded area is a 1σ scatter. All spaxels are corrected for extinction, filtered by SNR > 3, categorized as starforming from the [N II] diagnostic in section 2.1.4 and 3σ clipped in log(Hα) to remove outliers.

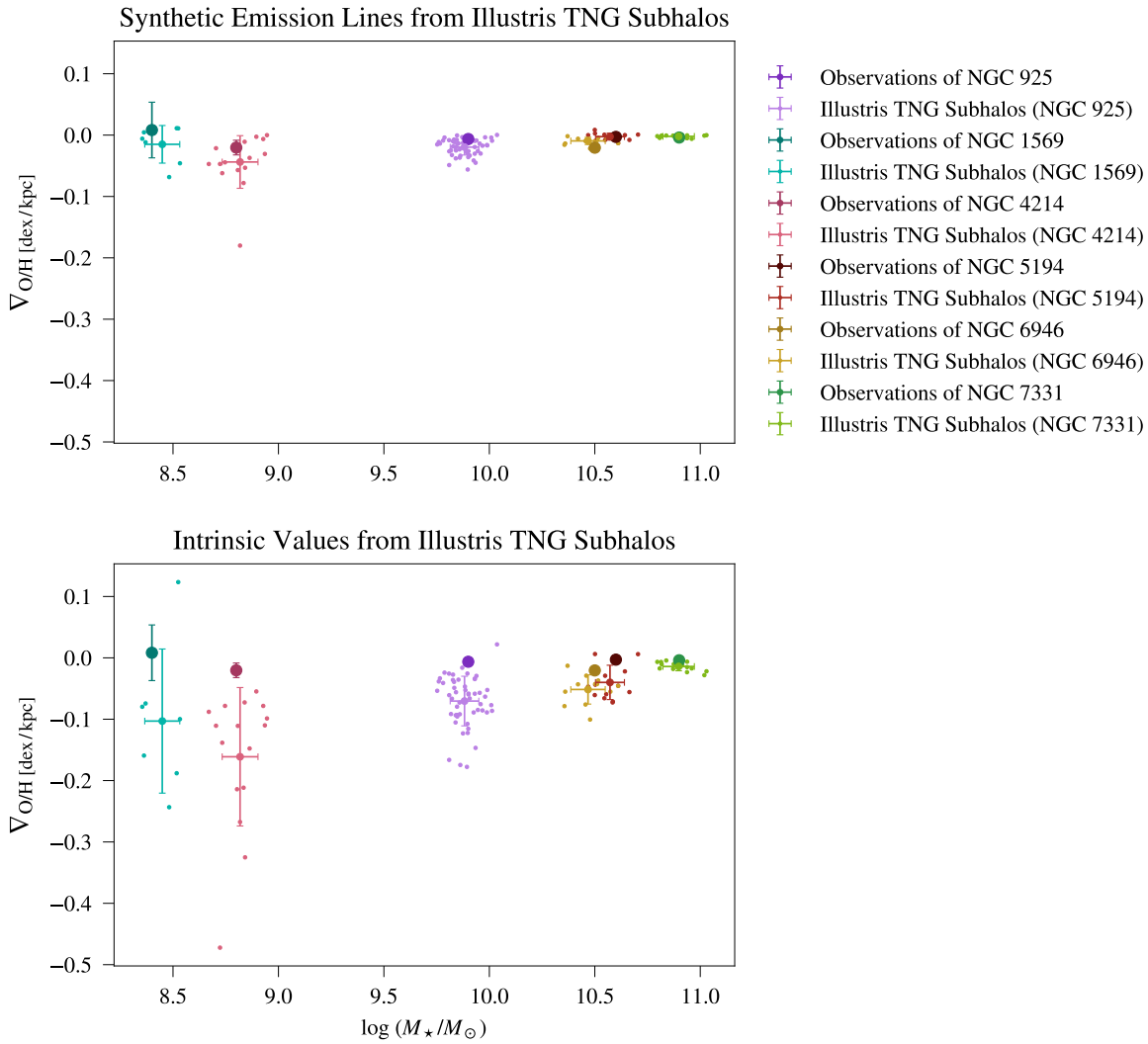

Figure C.5: Slope of metallicity gradients in units of [dex/kpc], derived from synthetic emission lines (top) and intrinsic simulation values (bottom), versus stellar mass of the full sample of Illustris TNG subhalos. The small dots are values for individual subhalos, color-coded by the observed galaxy to which any subhalo was matched, and the error bar of the same color is $\mu \pm \sigma$ for the respective subhalo sample. The darker colored error bars show values of the observed galaxies. The observed and synthetic metallicities are estimated with PG16.

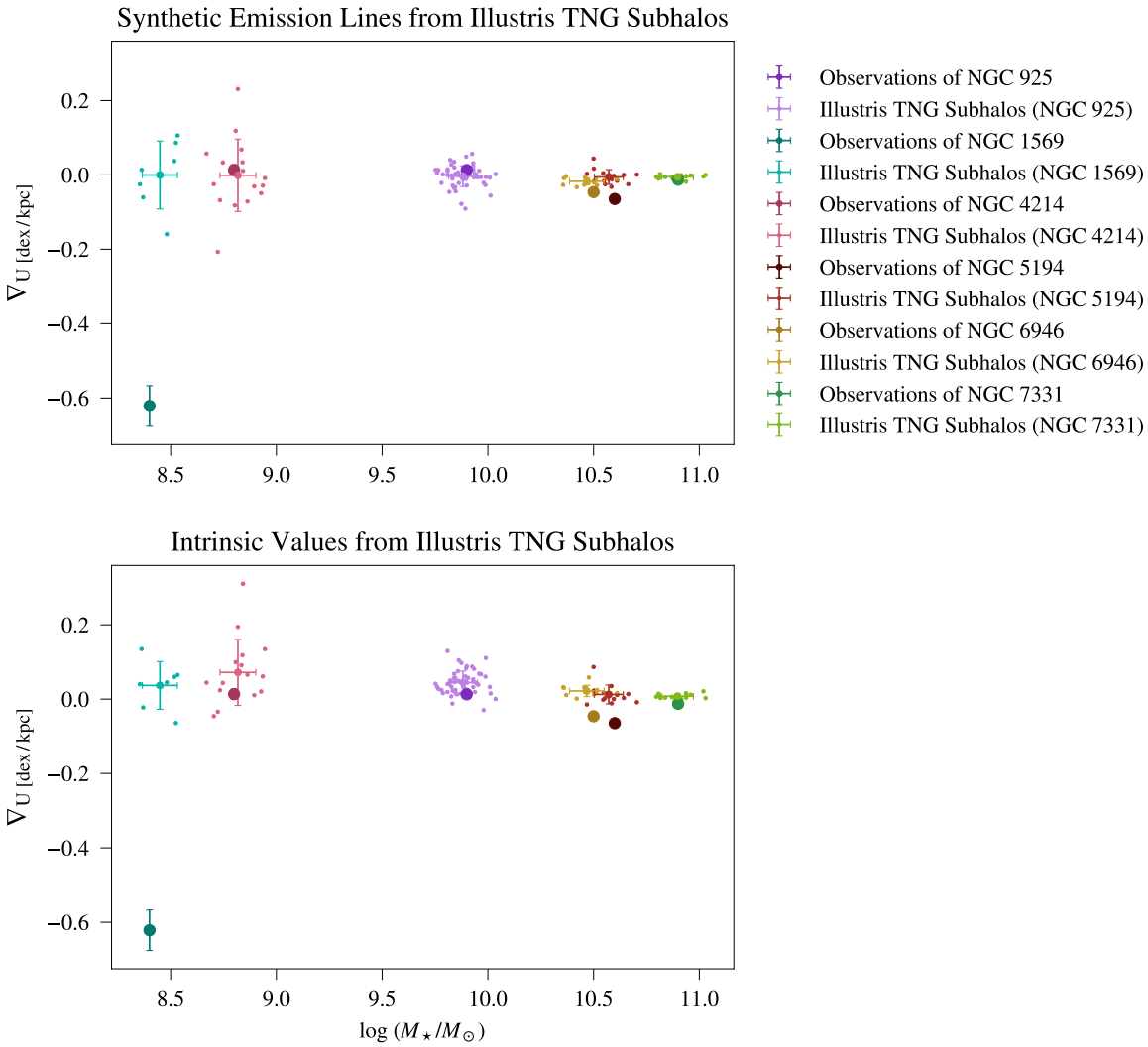

Figure C.6: Slope of ionization parameter gradients in units of [dex/kpc], derived from synthetic emission lines (top) and intrinsic simulation values (bottom), versus stellar mass of the full sample of Illustris TNG subhalos. The small dots are values for individual subhalos, color-coded by the observed galaxy to which any subhalo was matched, and the error bar of the same color is $\mu \pm \sigma$ for the respective subhalo sample. The darker colored error bars show values of the observed galaxies. The observed and synthetic ionization parameters are estimated using the calibration from Dors et al. (2016).

Appendix D

Strong Line Ratios, Metallicity and Ionization

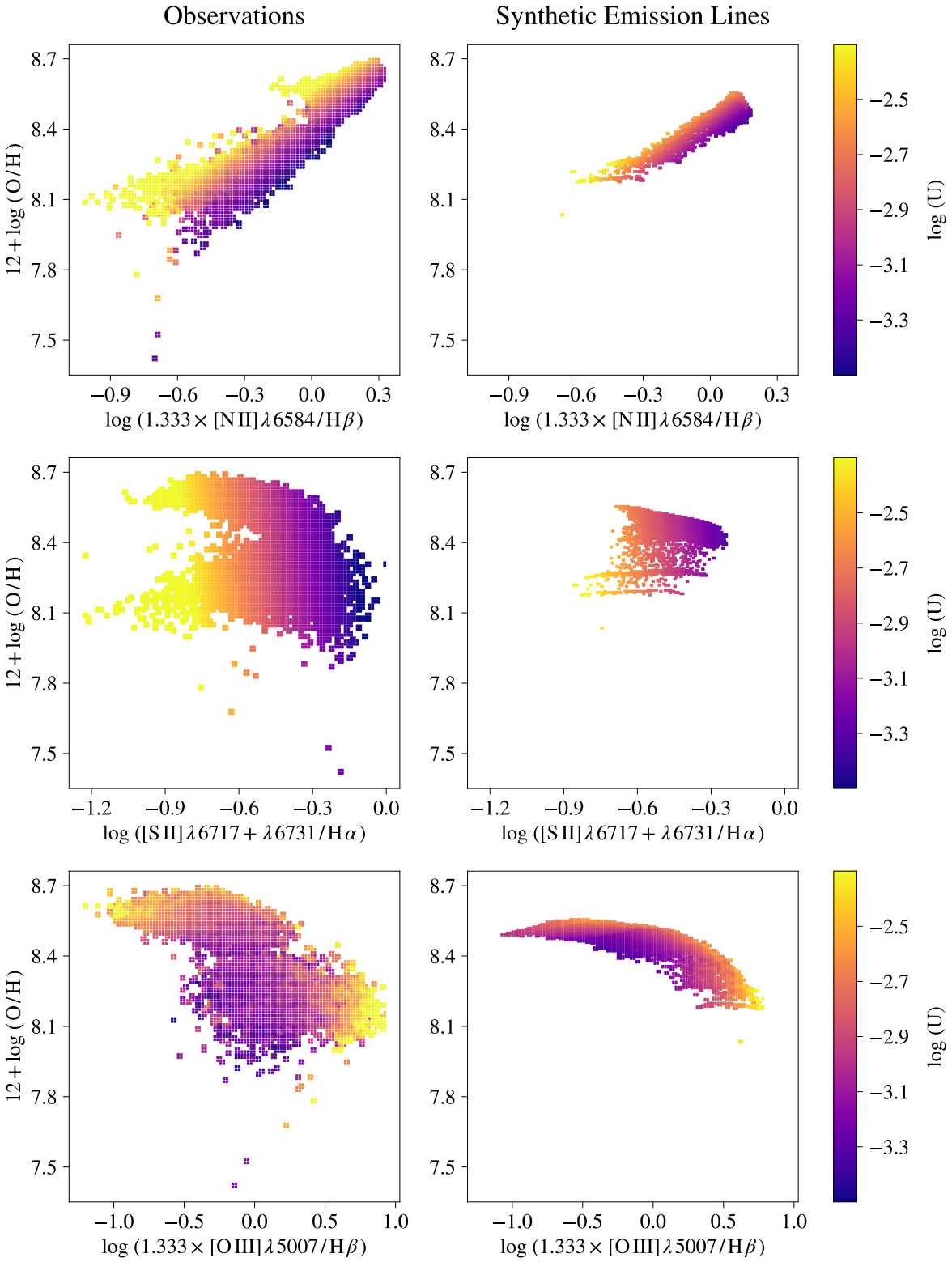

Figure D.1: 2D histogram of line ratios versus metallicity for individual spaxels of observed (left) and simulated galaxies (right), color-coded by ionization parameter. Parameters for the simulated sample are derived from the synthetic emission lines.

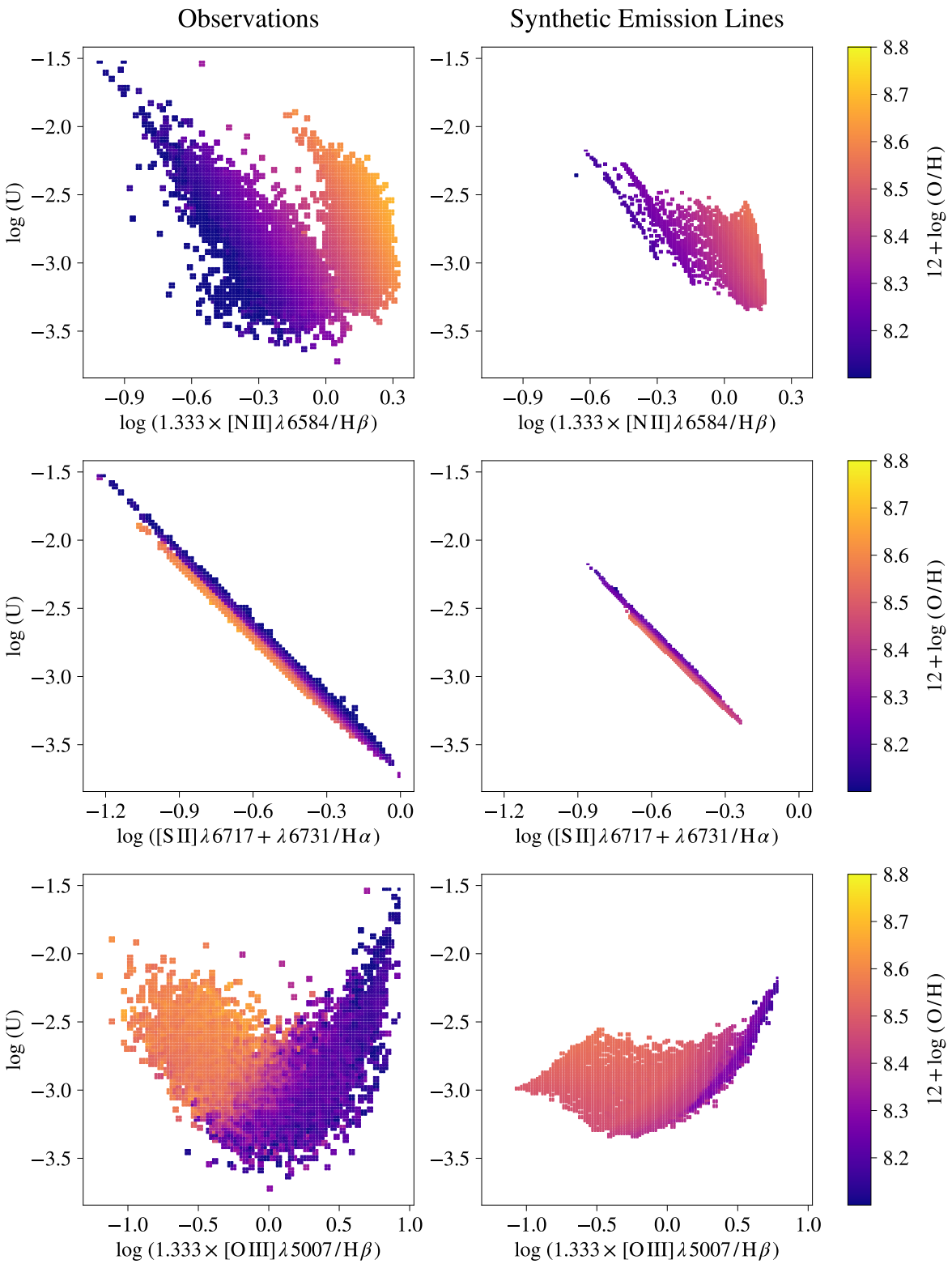

Figure D.2: 2D histogram of line ratios versus ionization parameter for individual spaxels of observed (left) and simulated galaxies (right), color-coded by metallicity. Parameters for the simulated sample are derived from the synthetic emission lines.

Appendix E

Results from Illustris TNG

The column names of table E.1 have the following meaning:

- Subhalo: SubhaloID of the Illustrins TNG subhalo
- TNG: Simulation volume; NGC: NGC name of the observed galaxy the subhalo was matched to
- $\log\left(\frac{M_\star}{M_\odot}\right)$: Stellar mass of subhalo
- $\log\left(\frac{M_{\mathrm{gas}}}{M_\odot}\right)$: Gas mass of subhalo
- log(SFR): Star formation rate of subhalo
- $(\mathrm{O/H})_S$: Total metallicity of subhalo, derived from synthetic emission lines
- $(\mathrm{O/H})_I$: Total metallicity of subhalo, derived from intrinsic simulation values
- $\nabla(\mathrm{O/H})_{S,R_\mathrm{e}}$: Slope of metallicity gradient of subhalo, derived from synthetic emission lines in units [dex/R_e]
- $\nabla(\mathrm{O/H})_{I,R_\mathrm{e}}$: Slope of metallicity gradient of subhalo, derived from intrinsic simulation values in units [dex/R_e]
- $\nabla(\mathrm{O/H})_{S,\mathrm{kpc}}$: Slope of metallicity gradient of subhalo, derived from synthetic emission lines in units [dex/kpc]
- $\nabla(\mathrm{O/H})_{I,\mathrm{kpc}}$: Slope of metallicity gradient of subhalo, derived from intrinsic simulation values in units [dex/kpc]

Subhalo	TNG	NGC	$\log\left(\frac{M_\star}{M_\odot}\right)$	$\log\left(\frac{M_{\rm gas}}{M_\odot}\right)$	log(SFR)	$(\mathrm{O/H})_S$	$(\mathrm{O/H})_I$	$\nabla(\mathrm{O/H})_{S,R_{\rm e}}$	$\nabla(\mathrm{O/H})_{I,R_{\rm e}}$	$\nabla(\mathrm{O/H})_{S,\rm kpc}$	$\nabla(\mathrm{O/H})_{I,\rm kpc}$
510586	50	925	9.9	9.8	0.5	8.43 ± 0.1	8.7 ± 0.2	-0.06 ± 0.07	-0.1	-0.03 ± 0.03	-0.07
282782	50	925	9.8	9.9	0.5	8.48 ± 0.03	8.8 ± 0.1	-0.03 ± 0.07	-0.1	-0.01 ± 0.02	-0.02
17	50	925	9.9	9.9	0.5	8.38 ± 0.09	8.6 ± 0.2	-0.06 ± 0.04	-0.1	-0.02 ± 0.01	-0.03
585080	50	925	9.9	9.9	0.7	8.4 ± 0.1	8.7 ± 0.2	-0.15 ± 0.06	-0.3	-0.03 ± 0.01	-0.05
676758	50	925	9.7	9.9	0.5	8.49 ± 0.05	8.9 ± 0.1	0.0 ± 0.1	-0.1	-0.01 ± 0.02	-0.04
319733	50	925	9.8	9.8	0.4	8.44 ± 0.05	8.7 ± 0.2	0.0 ± 0.1	-0.1	-0.01 ± 0.03	-0.03
229939	50	925	9.8	9.8	0.7	8.48 ± 0.04	8.8 ± 0.1	-0.01 ± 0.1	-0.06	0.00 ± 0.02	-0.01
446668	50	925	9.8	10.01	0.5	8.44 ± 0.07	8.7 ± 0.1	-0.06 ± 0.07	-0.1	-0.01 ± 0.02	-0.03
641249	50	925	9.8	9.8	0.3	8.4 ± 0.07	8.6 ± 0.1	-0.04 ± 0.08	-0.05	-0.02 ± 0.04	-0.02
557077	50	925	9.9	9.6	0.3	8.4 ± 0.1	8.7 ± 0.2	-0.07 ± 0.06	-0.1	-0.03 ± 0.03	-0.05
432108	50	925	9.7	9.9	0.5	8.44 ± 0.08	8.7 ± 0.2	-0.06 ± 0.06	-0.1	-0.01 ± 0.01	-0.03
574884	50	925	9.7	9.7	0.4	8.43 ± 0.06	8.7 ± 0.1	0.0 ± 0.1	-0.1	-0.02 ± 0.05	-0.05
651841	50	925	9.8	9.8	0.3	8.45 ± 0.04	8.7 ± 0.1	0.0 ± 0.1	-0.07	0.0 ± 0.1	-0.07
686753	50	925	9.8	9.7	0.3	8.46 ± 0.05	8.8 ± 0.1	-0.1 ± 0.2	-0.2	-0.02 ± 0.08	-0.09
499023	50	925	9.8	10.06	0.5	8.41 ± 0.06	8.7 ± 0.1	-0.03 ± 0.07	-0.06	-0.03 ± 0.05	-0.05
184941	50	925	9.9	10.004	0.6	8.47 ± 0.05	8.8 ± 0.2	0.0 ± 0.1	-0.2	-0.02 ± 0.04	-0.08
360924	50	925	9.9	9.9	0.3	8.44 ± 0.05	8.7 ± 0.1	0.0 ± 0.1	-0.1	-0.01 ± 0.03	-0.02
307491	50	925	9.8	9.6	0.7	8.5 ± 0.03	9.0 ± 0.1	0.0 ± 0.1	-0.1	-0.01 ± 0.04	-0.04
563051	50	925	9.8	9.7	0.3	8.35 ± 0.1	8.6 ± 0.2	-0.06 ± 0.07	-0.1	-0.03 ± 0.03	-0.06
411451	50	925	9.8	10.03	0.6	8.45 ± 0.04	8.7 ± 0.1	-0.04 ± 0.08	-0.1	-0.01 ± 0.02	-0.02
664263	50	925	9.9	10.05	0.7	8.47 ± 0.04	8.8 ± 0.1	-0.02 ± 0.04	-0.082 ± 0.0	-0.01 ± 0.03	-0.058 ± 0.0
29	50	925	9.7	9.6	0.4	8.44 ± 0.05	8.7 ± 0.1	-0.02 ± 0.05	-0.05	-0.01 ± 0.04	-0.03
667617	50	925	9.8	10.03	0.4	8.42 ± 0.07	8.7 ± 0.1	-0.05 ± 0.08	-0.1	-0.03 ± 0.04	-0.06
376549	100	925	9.8	9.8	0.5	8.42 ± 0.07	8.7 ± 0.2	-0.1 ± 0.1	-0.2	-0.02 ± 0.03	-0.05
379149	100	925	9.9	9.8	0.6	8.3 ± 0.1	8.6 ± 0.2	-0.1 ± 0.1	-0.2	-0.04 ± 0.04	-0.08
448841	100	925	9.8	9.7	0.5	8.44 ± 0.06	8.8 ± 0.2	-0.1 ± 0.2	-0.2	-0.01 ± 0.04	-0.06
253003	100	925	9.9	9.8	0.5	8.5 ± 0.04	9.0 ± 0.2	-0.1 ± 0.3	-0.3	-0.02 ± 0.07	-0.08
212844	100	925	9.9	9.8	0.5	8.46 ± 0.04	8.8 ± 0.1	-0.1 ± 0.1	-0.2	-0.01 ± 0.03	-0.05
387238	100	925	9.8	9.8	0.6	8.5 ± 0.05	9.0 ± 0.2	0.0 ± 0.6	-0.1	0.0 ± 0.2	-0.03
434412	100	925	9.8	9.8	0.4	8.5 ± 0.03	8.9 ± 0.2	0.0 ± 0.2	-0.3	-0.01 ± 0.06	-0.09
288749	100	925	9.8	9.8	0.4	8.46 ± 0.08	8.8 ± 0.2	-0.1 ± 0.3	-0.2	0.0 ± 0.1	-0.09
292359	100	925	9.8	9.8	0.5	8.47 ± 0.04	8.8 ± 0.2	-0.1 ± 0.3	-0.4	-0.02 ± 0.07	-0.1
540040	100	925	9.9	9.8	0.4	8.42 ± 0.09	8.8 ± 0.3	-0.1 ± 0.2	-0.3	-0.03 ± 0.04	-0.08
125050	100	925	9.8	9.6	0.5	8.52 ± 0.02	9.1 ± 0.1	0.0 ± 1.0	-0.4	0.0 ± 0.3	-0.1
319647	100	925	9.8	9.7	0.4	8.5 ± 0.03	9.0 ± 0.2	-0.1 ± 0.7	-0.7	0.0 ± 0.2	-0.1
305085	100	925	10.03	9.8	0.5	8.52 ± 0.02	9.12 ± 0.05	0.0 ± 0.2	0.09	0.00 ± 0.05	0.02

Table E.1

Subhalo	TNG	NGC	$\log\left(\frac{M_\star}{M_\odot}\right)$	$\log\left(\frac{M_{\rm gas}}{M_\odot}\right)$	log(SFR)	$(\mathrm{O/H})_S$	$(\mathrm{O/H})_I$	$\nabla(\mathrm{O/H})_{S,R_\mathrm{e}}$	$\nabla(\mathrm{O/H})_{I,R_\mathrm{e}}$	$\nabla(\mathrm{O/H})_{S,\mathrm{kpc}}$	$\nabla(\mathrm{O/H})_{I,\mathrm{kpc}}$
399845	100	925	9.9	9.8	0.4	8.51 ± 0.04	9.01 ± 0.1	0.0 ± 0.5	-0.1	0.0 ± 0.2	-0.06
228687	100	925	9.9	9.8	0.6	8.41 ± 0.1	8.7 ± 0.2	-0.1 ± 0.1	-0.1	-0.03 ± 0.05	-0.06
318634	100	925	9.8	9.8	0.4	8.52 ± 0.02	9.08 ± 0.1	0.0 ± 1.4	-0.3	0.0 ± 0.3	-0.07
140739	100	925	9.8	9.8	0.4	8.47 ± 0.07	9.0 ± 0.2	-0.1 ± 0.4	-0.4	0.0 ± 0.1	-0.1
236766	100	925	10.01	9.7	0.5	8.51 ± 0.03	9.0 ± 0.1	-0.1 ± 0.4	-0.4	-0.01 ± 0.07	-0.08
444444	100	925	9.8	9.7	0.4	8.4 ± 0.1	8.8 ± 0.2	-0.1 ± 0.1	-0.2	-0.04 ± 0.05	-0.09
437946	100	925	9.9	9.7	0.7	8.41 ± 0.09	8.7 ± 0.2	-0.2 ± 0.3	-0.4	-0.05 ± 0.08	-0.1
338459	100	925	9.7	9.8	0.5	8.5 ± 0.03	8.9 ± 0.1	0.0 ± 0.3	-0.1	0.00 ± 0.04	-0.02
319149	100	925	9.8	9.8	0.4	8.47 ± 0.07	8.9 ± 0.3	-0.1 ± 0.5	-0.6	0.0 ± 0.1	-0.1
125045	100	925	10.009	9.8	0.5	8.52 ± 0.02	9.0 ± 0.1	0.0 ± 1.0	-0.3	0.0 ± 0.2	-0.07
404646	100	925	9.9	9.6	0.5	8.47 ± 0.04	8.8 ± 0.09	0.0 ± 0.1	-0.09	-0.01 ± 0.05	-0.03
316859	100	925	9.8	9.8	0.7	8.4 ± 0.1	8.6 ± 0.2	-0.1 ± 0.2	-0.2	-0.06 ± 0.07	-0.1
146194	100	925	9.8	9.8	0.4	8.5 ± 0.03	9.0 ± 0.1	0.0 ± 0.2	-0.2	-0.01 ± 0.08	-0.09
284954	100	925	9.9	9.8	0.4	8.5 ± 0.03	9.0 ± 0.1	-0.1 ± 0.7	-0.1	0.0 ± 0.2	-0.05
241157	100	925	9.8	9.8	0.7	8.45 ± 0.04	8.7 ± 0.1	-0.03 ± 0.1	-0.1	-0.01 ± 0.03	-0.04
348042	100	925	9.9	9.7	0.3	8.47 ± 0.06	8.8 ± 0.2	-0.1 ± 0.3	-0.2	0.0 ± 0.2	-0.1
237948	100	925	9.8	9.7	0.3	8.43 ± 0.09	8.8 ± 0.3	-0.1 ± 0.1	-0.3	-0.03 ± 0.04	-0.1
599247	50	1569	8.4	7.9	0.07	8.48 ± 0.04	9.0 ± 0.2	$-$	$-$	$-$	$-$
670005	50	1569	8.2	7.8	0.06	8.5 ± 0.02	8.97 ± 0.08	$-$	$-$	$-$	$-$
388566	50	1569	8.3	7.9	0.02	8.52 ± 0.02	9.34 ± 0.05	0.0 ± 0.6	-0.064 ± 0.002	0.0 ± 0.7	-0.08 ± 0.002
569459	50	1569	8.3	8.08	0.06	8.52 ± 0.02	9.28 ± 0.08	0.0 ± 0.3	-0.045 ± 0.001	0.0 ± 0.6	-0.074 ± 0.002
533064	50	1569	8.5	8.003	0.05	8.31 ± 0.07	8.5 ± 0.1	0.0 ± 0.1	-0.05	0.0 ± 0.3	-0.09
621044	50	1569	8.3	8.007	0.09	8.52 ± 0.02	9.1 ± 0.1	0.0 ± 0.2	-0.05	0.0 ± 0.6	-0.1
524509	50	1569	8.3	8.07	0.02	8.4 ± 0.1	8.7 ± 0.3	$-$	$-$	$-$	$-$
661982	50	1569	8.3	7.7	0.03	8.42 ± 0.1	8.7 ± 0.2	$-$	$-$	$-$	$-$
654818	50	1569	8.5	8.05	0.07	8.48 ± 0.05	8.9 ± 0.2	0.0 ± 0.3	0.07	0.0 ± 0.5	0.1
275569	50	1569	8.3	7.8	0.007	8.5 ± 0.02	8.92 ± 0.04	$-$	$-$	$-$	$-$
63958	50	1569	8.4	7.9	0.01	8.47 ± 0.05	8.8 ± 0.2	-0.1 ± 0.5	-0.1	-0.1 ± 0.6	-0.2
143933	50	1569	8.3	7.9	0.004	8.48 ± 0.04	8.79 ± 0.05	$-$	$-$	$-$	$-$
682134	50	1569	8.4	7.9	0.006	8.5 ± 0.02	8.89 ± 0.05	$-$	$-$	$-$	$-$
117332	50	1569	8.4	8.07	0.009	8.47 ± 0.04	8.8 ± 0.1	$-$	$-$	$-$	$-$
355778	50	1569	8.5	7.7	0.04	8.51 ± 0.02	9.39 ± 0.05	$-$	$-$	$-$	$-$
411458	50	1569	8.3	8.05	0.01	8.52 ± 0.03	8.94 ± 0.07	$-$	$-$	$-$	$-$
436958	50	1569	8.5	8.1	0.07	8.51 ± 0.02	9.3 ± 0.1	0.0 ± 0.5	-0.1224 ± 0.0004	0.0 ± 0.7	-0.188 ± 0.0006
282793	50	4214	8.8	8.6	0.07	8.36 ± 0.09	8.6 ± 0.1	-0.2 ± 0.6	-0.3	-0.2 ± 0.5	-0.2
184984	50	4214	8.8	8.7	0.06	8.3 ± 0.1	8.6 ± 0.3	-0.2 ± 0.3	-0.4311 ± 0.0007	-0.1 ± 0.1	-0.2116 ± 0.0003
567386	50	4214	8.6	8.7	0.1	8.35 ± 0.1	8.6 ± 0.2	-0.1 ± 0.2	-0.1	0.0 ± 0.1	-0.08

Table E.1

Subhalo	TNG	NGC	$\log\left(\frac{M_\star}{M_\odot}\right)$	$\log\left(\frac{M_{\rm gas}}{M_\odot}\right)$	log(SFR)	$(\mathrm{O/H})_S$	$(\mathrm{O/H})_I$	$\nabla(\mathrm{O/H})_{S,R_\mathrm{e}}$	$\nabla(\mathrm{O/H})_{I,R_\mathrm{e}}$	$\nabla(\mathrm{O/H})_{S,\mathrm{kpc}}$	$\nabla(\mathrm{O/H})_{I,\mathrm{kpc}}$
208831	50	4214	8.7	8.7	0.06	8.42 ± 0.08	8.7 ± 0.2	-0.2 ± 0.8	-0.3	-0.1 ± 0.3	-0.1
791060	50	4214	8.8	8.8	0.07	8.45 ± 0.04	8.7 ± 0.2	–	–	–	–
445644	50	4214	8.7	8.5	0.1	8.46 ± 0.06	8.9 ± 0.4	0.0 ± 0.2	-0.2016 ± 0.0003	0.0 ± 0.4	-0.4723 ± 0.0007
797298	50	4214	8.8	8.8	0.07	8.4 ± 0.1	8.7 ± 0.2	–	–	–	–
184961	50	4214	8.8	8.7	0.03	8.49 ± 0.05	9.0 ± 0.1	–	–	–	–
586424	50	4214	8.7	8.8	0.1	8.32 ± 0.1	8.6 ± 0.2	-0.1 ± 0.1	-0.09	-0.04 ± 0.08	-0.07
375081	50	4214	8.8	8.7	0.03	8.48 ± 0.02	8.8 ± 0.1	0.0 ± 0.2	-0.06	0.0 ± 0.2	-0.05
589497	50	4214	8.7	8.4	0.1	8.3 ± 0.1	8.6 ± 0.3	–	–	–	–
488534	50	4214	8.7	8.6	0.03	8.46 ± 0.03	8.8 ± 0.1	0.0 ± 0.3	-0.1	0.0 ± 0.2	-0.1
690145	50	4214	8.8	8.9	0.08	8.36 ± 0.09	8.6 ± 0.1	–	–	–	–
812514	50	4214	8.8	8.9	0.07	8.47 ± 0.04	9.0 ± 0.2	-0.1 ± 0.7	-0.3374 ± 0.001	-0.1 ± 0.7	-0.3251 ± 0.0009
379810	50	4214	8.9	8.6	0.02	8.5 ± 0.01	8.9 ± 0.1	0.0 ± 0.3	-0.1	0.0 ± 0.2	-0.09
652863	50	4214	8.8	8.7	0.3	8.4 ± 0.08	8.7 ± 0.1	-0.1 ± 0.2	-0.1	-0.1 ± 0.2	-0.1
792996	50	4214	8.8	8.9	0.07	8.48 ± 0.03	8.8 ± 0.1	0.0 ± 0.5	-0.3598 ± 0.0007	0.0 ± 0.3	-0.2141 ± 0.0004
511307	50	4214	8.8	8.5	0.1	8.5 ± 0.02	8.9 ± 0.1	0.0 ± 0.2	-0.07	0.0 ± 0.2	-0.07
515298	50	4214	8.9	8.6	0.02	8.5 ± 0.02	8.9 ± 0.1	0.0 ± 0.3	-0.1	0.0 ± 0.2	-0.07
551974	50	4214	8.8	8.7	0.02	8.45 ± 0.04	8.8 ± 0.2	0.0 ± 0.3	-0.1773 ± 0.0006	0.0 ± 0.2	-0.1477 ± 0.0005
382217	50	4214	8.8	8.8	0.03	8.49 ± 0.03	8.9 ± 0.2	–	–	–	–
429477	50	4214	8.9	8.6	0.02	8.48 ± 0.03	8.8 ± 0.1	0.0 ± 0.3	-0.1187 ± 0.0002	0.0 ± 0.3	-0.11 ± 0.0002
41619	100	5194	10.7	9.4	3.01	8.5 ± 0.01	8.87 ± 0.02	0.00 ± 0.07	0.01	0.00 ± 0.04	0.006
69526	100	5194	10.5	9.7	3.1	8.47 ± 0.05	8.8 ± 0.2	-0.02 ± 0.08	-0.1	-0.01 ± 0.03	-0.04
52635	100	5194	10.5	9.6	1.7	8.5 ± 0.04	9.0 ± 0.1	0.0 ± 0.1	-0.1	-0.01 ± 0.03	-0.02
41616	100	5194	10.4	9.5	1.7	8.53 ± 0.02	9.28 ± 0.08	0.0 ± 1.0	-0.2	0.0 ± 0.2	-0.06
375402	100	5194	10.6	9.8	3.1	8.46 ± 0.04	8.7 ± 0.1	0.0 ± 0.1	-0.1	-0.01 ± 0.04	-0.04
161174	100	5194	10.4	9.6	2.2	8.52 ± 0.02	9.18 ± 0.1	0.0 ± 0.2	-0.2	0.00 ± 0.05	-0.04
41604	100	5194	10.6	9.7	4.1	8.52 ± 0.02	9.1 ± 0.1	0.0 ± 0.4	-0.2	-0.01 ± 0.09	-0.05
17216	100	5194	10.5	9.7	1.6	8.52 ± 0.02	9.3 ± 0.1	0.0 ± 0.6	-0.4	0.00 ± 0.09	-0.07
294513	100	5194	10.5	9.7	1.4	8.47 ± 0.03	8.8 ± 0.1	0.00 ± 0.04	0.0009	0.00 ± 0.01	0.0003
131058	100	5194	10.5	9.8	1.9	8.52 ± 0.02	9.2 ± 0.2	0.0 ± 0.2	-0.4	0.00 ± 0.03	-0.06
271731	100	5194	10.5	9.7	1.4	8.51 ± 0.02	9.1 ± 0.1	0.0 ± 0.5	-0.3	0.0 ± 0.1	-0.07
76111	100	5194	10.5	9.6	1.2	8.52 ± 0.02	9.13 ± 0.02	0.0 ± 0.5	0.01	0.0 ± 0.2	0.006
170544	100	5194	10.5	9.8	1.4	8.52 ± 0.02	9.1 ± 0.1	0.0 ± 0.2	-0.2	0.00 ± 0.05	-0.05
131057	100	5194	10.6	9.8	1.3	8.52 ± 0.02	9.18 ± 0.1	0.0 ± 0.1	-0.1	0.00 ± 0.02	-0.02
69526	100	6946	10.5	9.7	3.1	8.47 ± 0.05	8.8 ± 0.2	-0.02 ± 0.08	-0.1	-0.01 ± 0.03	-0.04
375402	100	6946	10.6	9.8	3.1	8.46 ± 0.04	8.7 ± 0.1	0.0 ± 0.1	-0.1	-0.01 ± 0.04	-0.04

Table E.1

Subhalo	TNG	NGC	$\log\left(\frac{M_\star}{M_\odot}\right)$	$\log\left(\frac{M_{\rm gas}}{M_\odot}\right)$	log(SFR)	$(\mathrm{O/H})_S$	$(\mathrm{O/H})_I$	$\nabla(\mathrm{O/H})_{S,R_\mathrm{e}}$	$\nabla(\mathrm{O/H})_{I,R_\mathrm{e}}$	$\nabla(\mathrm{O/H})_{S,\mathrm{kpc}}$	$\nabla(\mathrm{O/H})_{I,\mathrm{kpc}}$
288018	100	6946	10.4	10.06	3.3	8.47 ± 0.04	8.8 ± 0.1	-0.02 ± 0.06	-0.07	-0.01 ± 0.03	-0.02
336519	100	6946	10.3	10.06	3.3	8.46 ± 0.06	8.8 ± 0.2	-0.05 ± 0.06	-0.2	-0.01 ± 0.02	-0.05
421451	100	6946	10.3	10.004	3.4	8.5 ± 0.02	8.83 ± 0.08	-0.01 ± 0.05	-0.04	0.00 ± 0.02	-0.01
459518	100	6946	10.4	10.1	3.1	8.47 ± 0.06	9.0 ± 0.2	-0.1 ± 0.1	-0.2	-0.02 ± 0.05	-0.1
146190	100	6946	10.5	10.06	2.9	8.5 ± 0.02	9.0 ± 0.1	0.0 ± 0.1	-0.1	0.00 ± 0.02	-0.03
297211	100	6946	10.5	10.1	3.1	8.51 ± 0.03	9.1 ± 0.1	0.0 ± 0.1	-0.2	0.00 ± 0.03	-0.05
399268	100	6946	10.5	10.04	3.7	8.5 ± 0.05	9.0 ± 0.2	-0.05 ± 0.1	-0.2	-0.01 ± 0.02	-0.04
143888	100	6946	10.4	10.1	2.8	8.5 ± 0.03	8.9 ± 0.1	0.0 ± 0.2	-0.1	-0.01 ± 0.05	-0.04
429680	100	6946	10.4	10.07	2.7	8.5 ± 0.05	8.9 ± 0.2	0.0 ± 0.1	-0.3	-0.01 ± 0.03	-0.07
462833	100	6946	10.3	10.1	2.8	8.47 ± 0.06	8.8 ± 0.2	-0.1 ± 0.2	-0.3	-0.02 ± 0.04	-0.07
143888	50	7331	11.01	9.9	2.4	8.52 ± 0.02	9.03 ± 0.1	0.00 ± 0.08	-0.1	0.00 ± 0.02	-0.02
117256	50	7331	10.9	10.3	2.1	8.5 ± 0.03	9.0 ± 0.1	-0.03 ± 0.07	-0.1	0.00 ± 0.01	-0.02
394622	50	7331	10.8	10.3	3.7	8.51 ± 0.03	9.0 ± 0.1	-0.01 ± 0.04	-0.1	-0.001 ± 0.005	-0.01
143887	50	7331	10.9	10.3	1.9	8.52 ± 0.02	8.99 ± 0.06	0.00 ± 0.05	-0.06	0.000 ± 0.005	-0.006
264887	50	7331	10.8	10.3	2.1	8.48 ± 0.04	8.8 ± 0.1	-0.03 ± 0.1	-0.1	0.00 ± 0.01	-0.01
184935	50	7331	10.9	9.8	1.8	8.52 ± 0.02	9.23 ± 0.04	0.00 ± 0.05	-0.02	0.00 ± 0.02	-0.01
505586	50	7331	11.02	10.4	3.1	8.52 ± 0.02	9.2 ± 0.1	0.00 ± 0.05	-0.1	0.000 ± 0.006	-0.02
63868	50	7331	10.9	10.3	6.5	8.51 ± 0.02	9.0 ± 0.1	-0.01 ± 0.03	-0.09	-0.001 ± 0.003	-0.01
220597	50	7331	10.8	10.3	6.1	8.52 ± 0.02	9.08 ± 0.1	-0.01 ± 0.03	-0.08	-0.001 ± 0.004	-0.01
264886	50	7331	10.9	10.5	5.3	8.46 ± 0.06	8.8 ± 0.1	-0.03 ± 0.02	-0.08	-0.005 ± 0.004	-0.01
287338	100	7331	10.8	10.1	3.4	8.5 ± 0.02	9.00 ± 0.07	-0.01 ± 0.08	-0.05	0.00 ± 0.02	-0.01
249169	100	7331	10.8	10.05	1.8	8.51 ± 0.02	8.92 ± 0.07	0.00 ± 0.06	-0.02	0.00 ± 0.01	-0.004
388116	100	7331	10.8	10.3	3.9	8.47 ± 0.05	8.8 ± 0.1	-0.01 ± 0.04	-0.03	-0.002 ± 0.008	-0.006
222268	100	7331	10.9	10.4	2.5	8.47 ± 0.07	8.8 ± 0.1	-0.05 ± 0.1	-0.1	-0.01 ± 0.01	-0.01
279708	100	7331	10.7	10.3	1.8	8.5 ± 0.02	8.87 ± 0.07	0.0 ± 0.1	-0.05	0.00 ± 0.01	-0.006

Table E.1: Overview of parameters derived for the sample of Illustris TNG subhalos. The columns are described in appendix E. Entries with "$-$" could not be retrieved and are thus left empty.